SPECTROSCOPY AND DYNAMICS OF RYDBERG STATES OF NO IN STATIC AND RAMPED ELECTRIC FIELDS

Rakhee Patel

A thesis submitted for the degree of

Doctor of Philosophy

University College London

September 2007

ProQuest LLC
789 East Eisenhower Parkway
P.O. Box 1346
Ann Arbor, MI 48106-1346

ABSTRACT

This thesis reports the effect of applying static and ramped electric fields to quasi-bound Rydberg states of NO, with principal quantum number n = 25 – 32. The Rydberg states are excited by double resonance *via* the $v' = 0, N' = 0$, and $v' = 0, N' = 2$ rovibrational states of the intermediate $A^2\Sigma^+$ state of NO. Spectroscopic data is obtained by application of a static electric field ranging from 0 to 129 V cm^{-1}, and ramped electric fields.

In the presence of DC electric fields, the experimental Stark spectra presented in this thesis reveal a number of new interesting features, simulated using a matrix-diagonalisation approach. In this calculation, the adjustable parameters are the dipole transition moments from the various angular momentum components of the A-state, $A_{l'}(l)$, for which just one set is used to obtain the qualitative agreement with the experimental spectra *via* two different rotational states of the A-state.

The first detailed investigations of the selective field ionisation (SFI) of Rydberg states in a molecule are presented. The competition between electron-nuclear coupling and electron-field coupling is investigated and it is shown that the slew rate of the applied electric field can be exploited to control the rotational quantum state composition of field-ionised molecules.

ACKNOWLEDGMENTS

Firstly, I would like to thank my supervisor Prof. Helen Fielding for all her support and advice throughout my studies. Her patience and encouragement were essential to the success of this PhD.

The challenging last few years of my PhD were made endurable mainly due to the brilliant atmosphere created by my lab mates, Lizzy, Nick, Rob and Russ. I would like to thank Russ for being there to answer all my 'dim' questions and for putting up with me in my early lab days. Rob, the most patient person I know, was always there and ready to help out under any circumstances. I am also grateful to Nick for all his help during the 'fun' final years of my PhD. Lizzy, my 'sounding board' flatmate, who completely understood the joys of doing a PhD, was always there with the exact advice I needed.

Finally, big thanks to all my friends and family. Their endless support helped me get through the final years. Most importantly I am very grateful to my parents who always encouraged me, and without their unquestioning support this PhD would not exist.

THIS THESIS IS BASED ON THE FOLLOWING PUBLICATIONS

CHAPTER 4

Observation of the Stark Effect in $v^+ = 0$ Rydberg States of NO with a Matrix Diagonalisation Analysis

R. Patel, N.J.A. Jones and H.H. Fielding

Journal of Physics B – Atomic, Molecular and Optical Physics, **40** 1369–1381 (2007)

CHAPTER 5

Rotation-State Selective Field Ionisation of Molecular Rydberg States

R. Patel, N.J.A. Jones and H.H. Fielding

Physical Review A, **76** 043313 (2007)

OTHER PUBLISHED WORK:

Optical Control of the Rotational Angular Momentum of a Molecular Rydberg Wave Packet

R.S. Minns, R. Patel, J.R.R. Verlet and H.H. Fielding.

Physical Review Letters, **91**, 243601 (2003)

Interfering Rydberg Wave Packets in Na

R.E. Carley, E.D. Boléat, R.S. Minns, R. Patel and H.H. Fielding

Journal of Physics B – Atomic, Molecular and Optical Physics, **38** 1907-1922 (2005)

CONTENTS

FIGURES

CHAPTER 6: SUMMARY AND OUTLOOK

TABLES

CHAPTER 1

MOLECULAR RYDBERG STATES

ABSTRACT

Highly excited molecular Rydberg states have a number of unique properties which are fundamental to the results presented in this thesis. One property in particular is their sensitivity to external electric fields, known as the Stark effect. The experimental work in this thesis exploits the effects of applying an electric field to a molecular Rydberg system, which results in obtaining new spectroscopic and dynamical data for the NO molecule. In this chapter, concepts necessary to interpret these results are introduced and discussed. These include the physical characteristics of molecular Rydberg states as well as the Stark effect, which incorporates the fundamental basics of the field ionisation detection technique employed in these experiments.

1.1 A BRIEF HISTORY OF RYDBERG STATES

The concept of spectroscopy was first used by Newton (1666) who discovered that upon dispersion, white light from the sun gave a continuous spectrum of colours. Following this essential discovery, others, for example Kirchoff and Bunsen [1] soon realised that atoms and molecules have their own characteristic spectra and that from these spectra it was possible to determine the structural or chemical composition of various compounds. Key to the understanding of atomic spectroscopy was the significant contribution of the Swedish physicist J. R. Rydberg. His contributions to the spectroscopic laws allowed the interpretation of atomic and molecular line spectra (in the context of the Bohr model). The following section briefly describes his involvement in the development of spectroscopy.

In 1879 Liveing and Dewar [1] discovered from absorption studies that each atom gave a different and distinctive line sequence. Some spectra contained groups of spectral lines appearing in regular patterns, but initial attempts to characterise these lines were all unsuccessful. It was Balmer [1], in 1885, who related the frequencies of the lines to the formula given below

$$\lambda = \frac{m^2 h}{m^2 - n^2} \tag{1.1}$$

where h is the Planck's constant. When n = 2 and m = 3, 4, 5 or 6 then λ gives the first four visible lines of the hydrogen spectrum, which was named the Balmer series. Following this revelation other attempts were made to formulate a general solution to relate the frequencies of all the various lines series. For example,

Kayser and Runge [1,2] derived equations which gave the frequencies of various other series, but no universal solution was found. Rydberg also pursued this problem and extended the idea proposed by Balmer to produce a general formula [2]. His approach involved using the wave number (the number of waves occupying a unit length of a spatial analogue of frequency) as a unit of measure which greatly simplified the problem and resulted in a general formula. The newly established equation (equation 1.2), referred to as the Rydberg formula, includes a constant, R_X that was dependent on the system, X, excited.

$$\frac{1}{\lambda} = R_X\left(\frac{1}{n_1^2} - \frac{1}{n_2^2}\right), \tag{1.2}$$

In equation 1.2 λ is the wavelength of light emitted and n_1^2 and n_2^2 are integers such that $n_1 < n_2$. Rydberg was able to use this formula to reproduce the Balmer series as well as other series in Hydrogen, such as the far UV spectrum (Lyman) and far IR (Paschen). However, It was not until 1913 that Niels Bohr combined the atomic theory of electrons orbiting around a central nucleus, with the knowledge of Rydberg's work, to derive a formula for the constant used in the Rydberg formula [2]. From first principles he derived what is now known as the Rydberg constant

$$R_\infty = \frac{2\pi^2 me^4}{h^3 c} \tag{1.3}$$

where m is the mass of the electron, e is the charge of an electron, h is Planck's constant and c is the velocity of light.

Initial experimental investigations of Rydberg states were limited to absorption studies by the available technology. As technology developed, it allowed increased access of higher Rydberg states, and this resulted in the beginnings of modern (high resolution) spectroscopy. Most significantly the advent of tuneable lasers, in particular dye lasers, has allowed detailed investigations of selected Rydberg states.

The first high-resolution spectroscopic study of rotationally-resolved molecular Rydberg states was conducted in H_2. This was first observed as a function of wave length through a spectrometer by Herzberg and Jungen [3]. Other experimental investigations involved excitation of an electron from the ground state to the Rydberg states *via* one photon absorption of VUV light (i.e. absorption spectrum of H_2) [4,5].

1.2 RYDBERG SERIES

A Rydberg state of an atom or molecule is one in which an electron is promoted to a highly excited electronic state such that its motion is largely independent of the remaining core [2]. The large orbital radius means the Rydberg electron only sees the core as a 1+ point charge, essentially equivalent to the hydrogen atom which comprises of just a proton and an electron. The Rydberg equation which gives the binding energy of the state, E in cm^{-1}, is given by

$$E = -\frac{R_X}{n^2} \tag{1.4}$$

where in n is the principal quantum number and

$$R_X = \frac{\mu e^4}{8\varepsilon_0^2 h^3 c} \tag{1.5}$$

is the Rydberg constant in wave numbers for some molecular system, X. In equation 1.5 e is the charge on the electron, ε_0 is the permitivity of free space, h is Planck's constant and μ is the reduced mass of the core. The reduced mass is given by $m_1 m_2/(m_1 + m_2)$ where m_1 and m_2 are the mass for the two bodies. Rydberg states in the Hydrogen atom with the same n but different electronic orbital angular momentum, l are degenerate. States differing in n but the same l are collectively referred to as a Rydberg series, where upon each series converges to an ionisation threshold (figure 1.1 (A)). Each n level contains n degenerate l states.

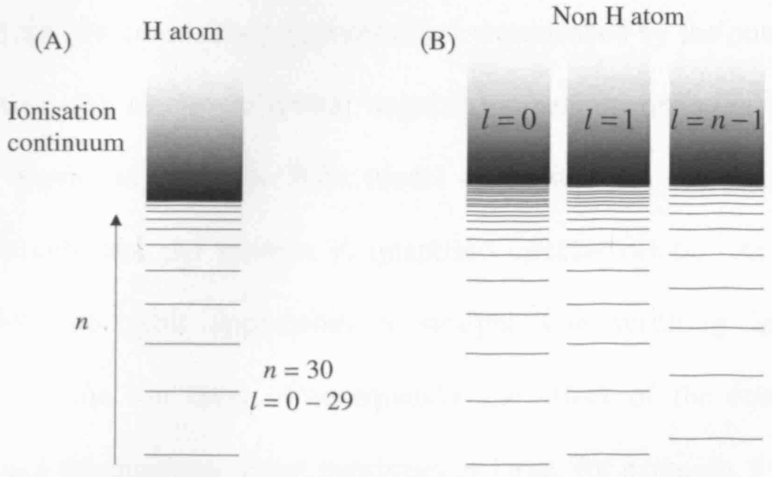

Figure 1.1 A schematic diagram illustrating a Rydberg series for (A) the Hydrogen atom and (B) a non hydrogenic atom. States differing in l in the non hydrogenic atom are not degenerate leading to several Rydberg series. There are several Rydberg series in the Hydrogen atom, also defined by l, which happen to be degenerate.

For atoms other than hydrogen, the existence of a core containing the nucleus and electrons induces perturbations to the energy of the Rydberg states. The potential felt by the Rydberg electron is no longer purely Coulombic along its whole radial orbit. For large radial distances, r (the distance of the electron from the ion core), where the electron is sufficiently far from the core, it still feels a pure Columbic potential, and can therefore be described as hydrogenic like. As r approaches 0 (i.e. the core region) a more complex potential must be considered. The influence of the core electrons on the Rydberg electron is characterised by a quantum defect value [2]. When the repulsive forces of the core electrons dominate the attractive effect of the core, the energy is lowered as indicated in equation 1.6,

$$E = -\frac{R}{(n-\delta_l)^2} \tag{1.6}$$

where δ_l is the angular momentum-dependent quantum defect. The quantum defect parameter gives a quantitative measure of the interaction of the excited electron with the ion core. The repulsive effect experienced by the outer electron is dependent on the electronic orbital angular momentum quantum number, l. This can be explained using the Bohr model of an atom, in which an electron orbits a positively charged nucleus in quantised circular orbits. At low l the classical electronic orbit approaches a straight line resulting in frequent encounters with the ion core. Consequently the effect of the core is more pronounced and the quantum defect parameter is large, for example, for NO δ_p = 0.7286 [6,7] where δ_p is the quantum defect of an electron with p angular momentum. As l becomes large, the classical electronic orbit becomes more circular resulting in the electron spending less time near the core region.

Consequently, there is less core penetration and the quantum defects for these states are smaller, sometimes negligible. For example, the states in NO with *f* angular momentum character have a quantum defect value of 0.01 [6] hence their energies are comparable to the hydrogen states. As a result of the *l*-dependence on the quantum defect the degeneracy of Rydberg states of same *n* and different *l* character is lifted. This results in several Rydberg series all converging upon the same ionisation threshold characterised by their *l* quantum number (figure 1.1 (B)). It is interesting to note that despite the *f* quantum defect being so small, the size can be significant in determining the field ionisation dynamics as illustrated in chapter 5.

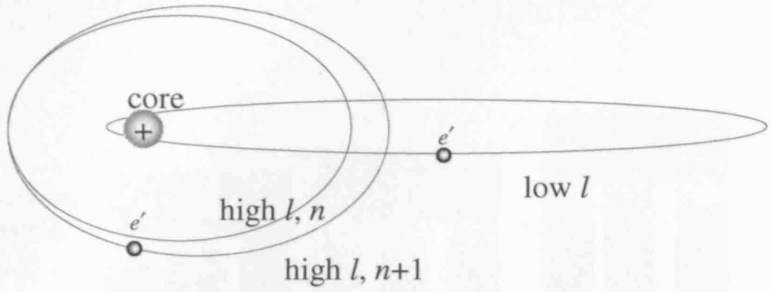

Figure 1.2 A schematic diagram illustrating a classical trajectory for low and high electronic orbital angular momentum states of Rydberg system. The electron visits the core region more often when it has low electronic orbital angular momentum.

The Rydberg states of a molecule are further perturbed from the hydrogenic model due to the presence of a rotating and vibrating core. A molecular Rydberg state is described by the rotational and the vibrational quantum numbers of the

core, N^+ and v^+ respectively, as well as the electron quantum numbers (n, l). The energy of a given Rydberg state which is not perturbed by any other Rydberg series is given, to the 1st approximation, by

$$E = IP_{v^+N^+} - \frac{R}{(n-\delta_l)^2} \tag{1.7}$$

where $IP_{v^+N^+}$ is the ionisation potential to which a Rydberg series converges. Each Rydberg series is characterised by states with the same v^+, N^+. The greater number of series creates more opportunities for inter-series couplings as well as with other continua leading to decay processes such as autoionisation or predissociation. These decay processes and inter-series interactions will be discussed further in section 1.4 and chapter 4 respectively.

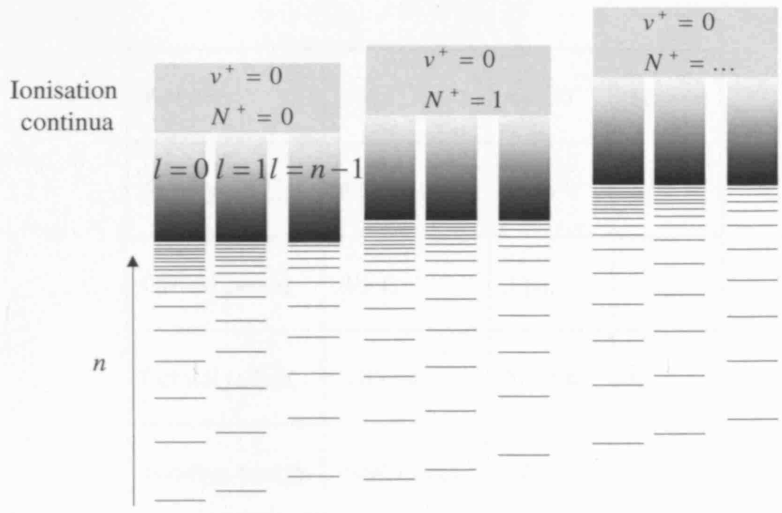

Figure 1.3 A schematic diagram of a molecular Rydberg system with several Rydberg series. Each series converges upon a different ro-vibrational ionisation continuum.

1.3 PROPERTIES OF MOLECULAR RYDBERG STATES

To date, investigations of Rydberg states have concentrated on three different regions defined by the value of the principal quantum number, n: low n $(n < 10)$, high n $(11 < n < 50)$ and ZEKE (zero electron kinetic energy) states with $n > 100$ (Rydberg states which lie within about 11 cm^{-1} of the ionisation limit). Early studies of molecular Rydberg states mainly consisted of the low n states, primarily due to the available equipment and technology at that time. As technology improved Rydberg states with higher n were accessed and this led to the advent of ZEKE spectroscopy. In this thesis the intermediate high n region is considered.

Table 1.1 compares some of the important physical properties for n = 1 and n = 30 Rydberg states for the Hydrogen atom, and shows how they scale with n.

Property	n = 1	n = 30	Scaling
Energy spacing	80 000 cm^{-1}	3 cm^{-1}	n^{-3}
Orbital period	0.1 fs	5 ps	n^{3}
Orbital radius	0.05 nm	0.1 mm	n^{2}
Binding energy	109677 cm^{-1}	122 cm^{-1}	n^{-2}

Table 1.1 A selection of physical properties of Hydrogen Rydberg states with principal quantum number n = 1 and n = 30, and how they scale with n.

In equation 1.6 it is evident that in the limit of high principal quantum number, the energy spacing between adjacent Rydberg states scales as n^{-3}. As a result, states close to the ionisation limit are very close in energy. Since the spacing between adjacent Rydberg states is small it is experimentally feasible to create Rydberg wave packets using the broad bandwidth of a picosecond laser (~ 15 cm^{-1}), where a Rydberg wave packet is a coherent superposition of two or more Rydberg states [8]. It has therefore been possible to study the time dependent dynamics of the Rydberg electron in the form of a wave packet (in our group [9-14] and other atomic [15-21] and molecular [14,22,23]) systems).

In terms of the Bohr model, a bound particle in a $1/r$ Coulomb potential moves in an orbit with period $\tau = 2\pi n^3$ (a.u.). An electron with n = 1 has a classical orbit period of approximately 150 *as* (1 *as* = 10^{-18} s), which is almost ten times faster than molecular vibrations and 10 - 1000 times faster than molecular rotations. The significance of this is that the electronic distribution adjusts rapidly to the nuclear motion. In this case, the Born-Oppenheimer approximation, in which the motion of the nucleus is stationary with respect to electronic motion, is valid. On the other hand, for an electron with n = 30 the classical orbit period is almost 5 ps, which is the same order of magnitude as molecular rotations and around one thousand times slower than typical molecular vibrations (the inverse Born-Oppenheimer regime). The small binding energy of the Rydberg electron is also a consequence of its large radial distribution. This makes field ionisation of the electron possible using experimentally achievable electric fields. The Rydberg electron spends a relatively large amount of its time at large r and so it is highly susceptible to external fields. This is of particular significance for work presented

in this thesis in which an external electric field is applied to molecular Rydberg states. The effect of an electric field on the molecular Rydberg states will be discussed in further detail in section 1.5.

At small distances the Rydberg electron interacts with the core leading to inter-series coupling, which results in the perturbation of states. An example of such a coupling is the well documented *s-d* interaction in NO [7,24]. Further details on inter-series couplings are discussed in chapter 4.

1.4 LIFETIMES OF RYDBERG STATES/DECAY PROCESSES

In general, Rydberg states have a large radial distribution. The electron therefore spends most of its time relatively far from the ion core which results in a long electronic lifetime. However, the presence of the ion core means that there is the possibility of interactions leading to decay. Molecular Rydberg states can decay *via* the radiative decay processes of spontaneous emission or stimulated or absorption emission induced by black body radiation from the surroundings. In spontaneous emission, the rate of decay of electron population to lower lying states is dependent on the principal electronic quantum number, n and the electronic angular quantum number, l. In comparison, black body radiation tends to induce decay to near lying states with a dependence only on n. The black body lifetimes scale with n^2 compared to n^3, the spontaneous emission lifetime, and thus spontaneous emission dominates at high n. Rydberg states can also decay *via* non-radiative processes where the final decay outcome is dependent on the state.

In a molecule, other decay processes are possible as well. The lifetimes of molecular Rydberg states are governed by interactions of Rydberg series with the continuum associated with ionisation or dissociation of the molecular core. These interactions lead to the non-radiative processes such as autoionisation and predissociation. A Rydberg state can autoionise if it lies above an ionisation continuum, and can dissociate if it interacts with another state above its dissociation limit. Since the decay processes occurs in the core region, the lifetime of a Rydberg state, $\tau(n)$, is directly proportional to the orbit period of the electron and therefore also scales with n^3. As n and l increases the electron encounters the core less frequently and so these states have longer lifetimes.

Lifetimes can be determined in the frequency domain by measuring or calculating the homogeneous line-width of a molecular Rydberg state, $\Gamma(n)$. The total line width of a molecular Rydberg system is given by

$$\Gamma(n) = \Gamma_0 / n^3 \tag{1.8}$$

where Γ_0 (cm^{-1}) are zero field, experimentally-determined decay parameters which vary with the electronic orbital angular momentum of Rydberg states. The Lifetime of the Rydberg state is then given by

$$\tau(n) = \hbar/\Gamma(n). \tag{1.9}$$

It has been shown that the lifetimes of Rydberg states vary with vibrational character as well with n. Experimentally, the decay parameters in NO used for states converging to the $v^+ = 1$ continuum [25] are larger compared to the decay

parameters for the states converging to the $v^+ = 0$ ionisation limit [6,26-28]. This is due to the Rydberg states converging to the $v^+ = 0$ continuum only decaying *via* predissociation compared to the Rydberg states converging to $v^+ = 1$ continuum which also decay *via* autoionisation. For example *np* Rydberg states converging to $v^+ = 0$ continuum have a decay parameter (zero field decay linewidths) of 1610 cm^{-1} [27] compared to 4000 cm^{-1} [25] for *np* states converging to the $v^+ = 1$ continuum

Exceptions to the expected lifetimes have been found in studies involving ZEKE states. The lifetimes of these states have been found to exceed the expected values. For example, Vrakking *et al.* [27] studied the lifetimes of the *np* and *nf* ZEKE series of NO (n = 40 - 120), and reported lifetime enhancements of these series. They compared these lifetime values favourably to calculated lifetimes using the angular momentum model. This model was first proposed by Chupka *et al.* [29-31]. The long lifetimes of these states were explained by the presence of small stray dc fields which are typically found in experiments involving ZEKE states. The presence of an electric field causes the l Rydberg states to mix, resulting in a dilution of the l character of the state. The result is a mixed l state that, unlike a pure low l state, interacts only weakly with the ionic core. The consequence is lower rates of decay processes such as autoionisation and predissociation and a significant enhancement of the lifetimes of the Rydberg states.

1.4.1 AUTOIONISATION

If the Rydberg states are excited above the lowest ionisation limit then they are termed autoionising states. Classically, this can be considered as the electron colliding with the ion core and gaining sufficient energy to escape the Coulomb potential and ionise. Quantum mechanically, autoionisation can be considered as involving a bound state, which is degenerate with the ionisation continuum of a lower energy state of the molecular ion. In molecular systems, the core has several types of energy which can be transferred to the Rydberg electron. For example, in rotational autoionisation the core loses rotational energy and the electron gains kinetic energy, resulting in ionisation. This can be understood in terms of quantum mechanics as a state coupling to a continuum which has the same vibrational level, v^+ but with different rotational level, N^+. Similarly in vibrational autoionisation the core loses vibrational energy to the electron. An analogous form of decay in Rydberg atoms is spin-orbit autoionisation.

1.4.2 PREDISSOCIATION

In a similar manner to autoionisation, predissociation occurs when the Rydberg electron collides with the ion core resulting in its energy being transferred into vibrational energy which then leads to dissociation of the molecule. Alternatively, the Rydberg state can be considered as being degenerate with a continuum associated with the dissociated molecule. For example in figure 1.4 rovibrational levels in the molecular ion potential energy curve which lie above the dissociation

limit of the electronic state (dissociating potential energy curve) can result in decay *via* predissociation.

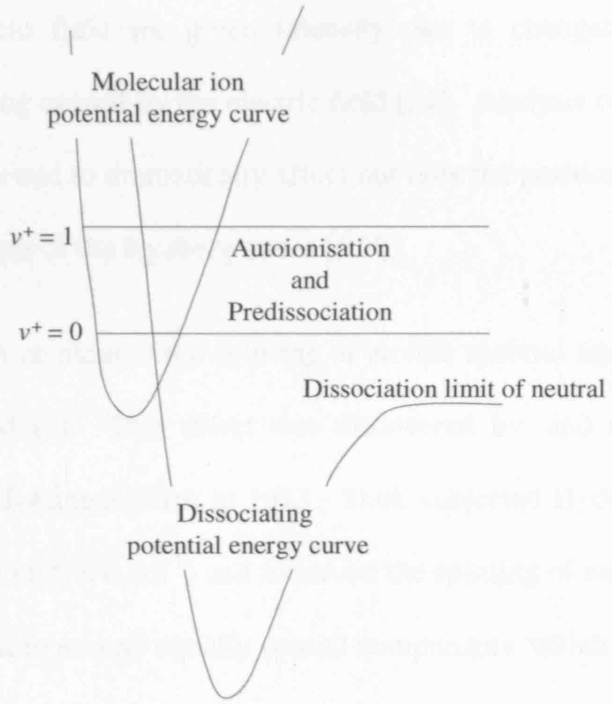

Figure 1.4 A schematic diagram illustrating the autoionisation and predissociation processes for a Rydberg state. Autoionisation occurs when the excited Rydberg states (rovibrational) are degenerate with an ionisation continuum of a lower energy state of the molecular ion. In a similar manner, predissociation occurs when the states are degenerate with a dissociating continuum. The $v^+ = 0$ vibrational levels can only dissociate whereas excitation into the $v^+ = 1$ levels allows competition between autoionisation and predissociation.

1.5 RYDBERG STATES IN AN ELECTRIC FIELD: THE STARK EFFECT

The macroscopic orbital radius of a Rydberg state makes it highly sensitive to an external electric field. The work in this thesis exploits this property, allowing experiments to be carried out with relatively low electric fields. One very

significant reason for studying the effect of an electric field on a molecular Rydberg system is that it enables a more in-depth study of the system, in particular the electron-core coupling. Also Rydberg states that are otherwise inaccessible in zero field are given intensity due to changes in the angular momentum coupling caused by the electric field [32]. Analysis of the Stark effect in molecules has found to dramatically affect not only the positions and intensities but also the lifetimes of the Rydberg states [6,27].

The Stark effect in an atom is the splitting of atomic spectral lines when exposed to an electric field [2]. This effect was discovered by, and named after, the German physicist Johannes Stark in 1913. Stark subjected Hydrogen atoms to a static electric field (100 kV cm^{-1}) and observed the splitting of each of the lines in the Balmer series into several equally spaced components, which are now referred to as a Stark manifold [2].

In a Rydberg system the electric field affects the coupling of the electronic orbital angular momenta, such that for every principal quantum number n, all l states couple according to the $\Delta l = \pm 1$ selection rule. A state with no intensity at zero field gains intensity by coupling to a state which has intensity at zero field. For example, excitation from an s state would give rise to Rydberg states of p character only. In a field, this p state can couple with states of d character giving them intensity, which can then couple to states with f character and so on. This sequence of $\Delta l = \pm 1$ couplings continues until all n states have intensity. This results in the angular momentum of the Rydberg electron no longer being conserved and l ceases to be a good quantum number. Also, the degeneracy of the

high l states in zero field of a Rydberg state n is lifted and splits into a Stark manifold (see figure 1.5) of $n-|m|$ separate Stark states where m is the magnetic quantum number. The energy of a Stark state is determined by solving the Schrödinger equation with the Hamiltonian including the perturbation,

$$H = H_{elec} + H_{rot} + H_F \tag{1.10}$$

where H_{elec} is the electronic and H_{rot} is the rotational Hamiltonian. $H_F = -eFz$ is the Stark Hamiltonian where F is the electric field in the z direction. Incorporating the perturbation of an electric field, the Schrödinger equation becomes separable in the parabolic co-ordinates

$$\xi = r + z \tag{1.11}$$

$$\eta = r - z \tag{1.12}$$

$$\phi = \arctan\frac{y}{x} \tag{1.13}$$

where $z = r\cos\theta$. The wavefunction in the Schrödinger equation is now written in terms of the quantum numbers n, m, n_1 and n_2

$$\Psi(\xi,\eta,\phi) = (2\pi\xi\eta)^{-\frac{1}{2}} f_{n_1 m}(\xi) g_{n_2 m}(\eta) e^{im\phi} \tag{1.14}$$

where n_1 and n_2 are the number of nodes in the separated parts of the wavefunction. These parabolic quantum numbers are related by $k = n_1 - n_2$ and are non-negative integers,

$$n_1 = 1,2,3\ldots n-1$$

$$n_2 = 1,2,3\ldots n-1$$

and must satisfy

$$n = n_1 + n_2 + |m| + 1 \tag{1.15}$$

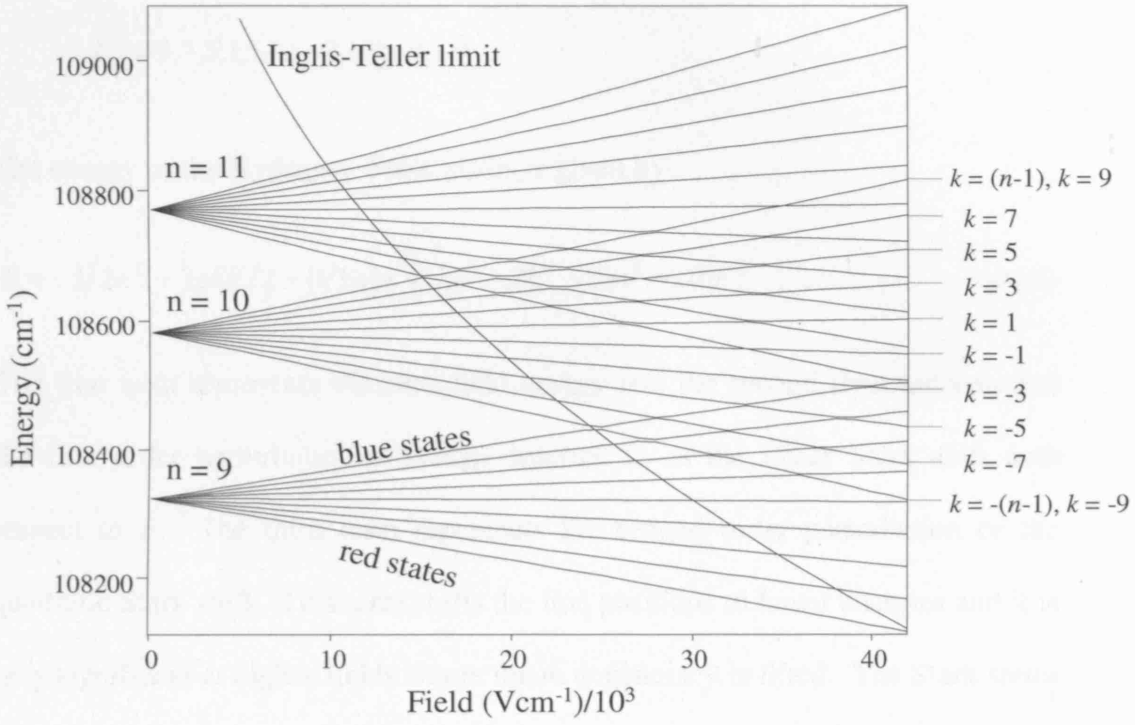

Figure 1.5 Stark manifolds for the Hydrogen atom with n = 9, 10 and 11 as function of electric field strength, F. The number of Stark states per manifold is given by $n-m$, where m is the magnetic quantum number. Each of these Stark states are labelled with quantum number k, and their value ranges between $(n-1-m)$ and $-(n-1-m)$. The first order energy of a Stark state is given by $E = -1/2n^2 + 3nkF/2$ and the energy gap between adjacent states is given by $\Delta E = 3nF$. Stark states which go up in energy are referred to as blue states and those lower in energy as red states. The point at which the Stark states from neighbouring manifolds cross is given by the Inglis-Teller limit, $F = 1/3n^5$ (curve).

For example, if a Stark manifold of n = 10 (figure 1.5) is accessed using laser light with parallel polarisation with respect to the applied electric field, giving m = 0, then the k values are given as

$$n_1 = 9,8,7,6,5,4,3,2,1,0$$

$$n_2 = 0,1,2,3,4,5,6,7,8,9$$

$$k = 9,7,5,3,1,-1,-3,-5,-7,-9$$

The energy of the Hydrogen Stark states is given by

$$E = -1/2n^2 + 3nkF/2 - (1/16)n^4\left[17n^2 - 3k^2 - 9m^2 + 19\right]F^2 \qquad (1.16)$$

The first term represents the zero field energy and the second term incorporates the first order perturbation in energy referred to as the linear Stark shift with respect to F. The third term represents the second order perturbation or the quadratic Stark shift. This term shifts the line positions to lower energies and it is only significant at higher fields where the m degeneracy is lifted. The Stark states of non-hydrogenic systems can be calculated using either matrix diagonalisation [27,32] (of the perturbed Hamiltonian) or multichannel quantum defect theory (MQDT) [33], each of which has its own advantages and disadvantages as discussed in chapter 4. Stark simulations in this thesis were calculated using a hybrid MQDT-matrix diagonalisation method, as first described by Vrakking [27] with further details given in chapter 4.

In an electric field, the Coulomb potential of a Rydberg electron is considerably altered. The states that increase in energy with increasing external electric field

are localised uphill in the potential and are known as blue Stark states, whilst those that are localised downhill are known as red Stark states. As the 2nd term in equation 1.10 has a linear n dependence, an increase in n results in an increase in the spacing between k states. In the Hydrogen atom this leads to the crossing of Stark states belonging to different n manifolds. These crossings occur at the Inglis-Teller limit $F = 1/3n^5$ [2], which is defined as the point at which the extreme Stark states belonging to neighboring manifolds overlap. This limit is defined by taking into consideration the energy spacing of adjacent n states at zero field, $1/n^3$ and the linear Stark shifts of the most extreme states of the n manifold, $\pm 3n^2F/2$ ($m = 0$).

Each Stark state consists of a mixture of l = 0, 1, 2... (n - 1) character. The intensity distribution of p character is dependent on the polarisation of the exciting laser light with respect to the applied electric field (figure 1.6). If the light is polarised parallel to the electric field (m = 0), the intensity distribution of the l states lie at the edges of the manifold, comprising the reddest and bluest stark states (figure 1.6 A). Conversely, if the light is perpendicularly polarised ($|m|$ = 1) the distribution is more central (figure 1.6 B).

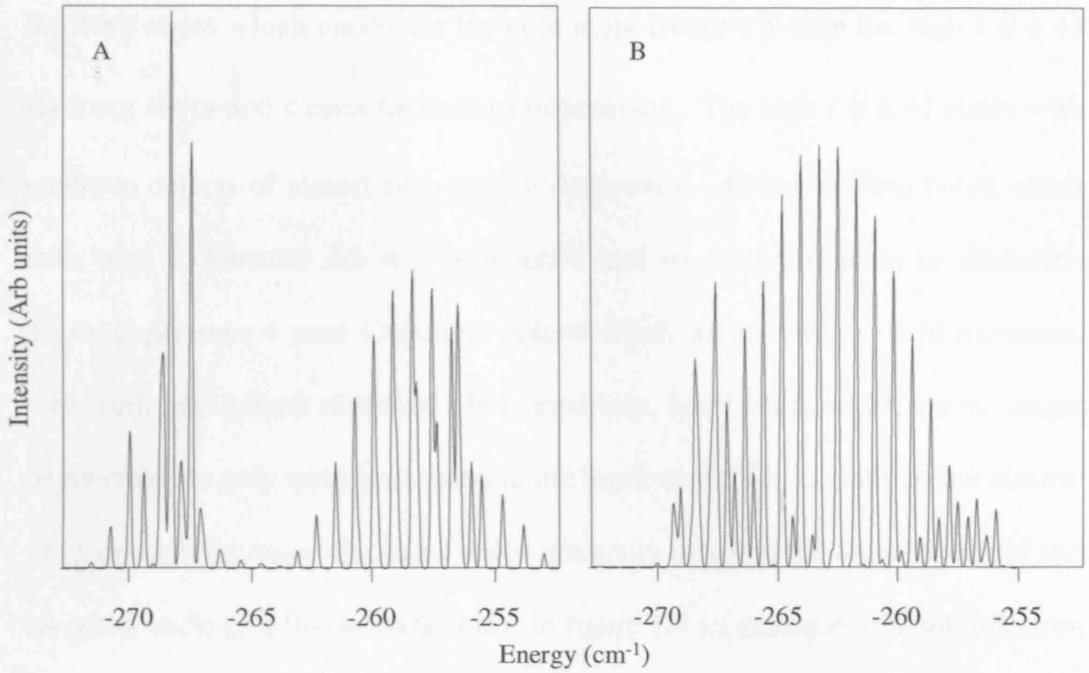

Figure 1.6 Matrix diagonalised calculation of a Rydberg stark manifold intensity, after excitation using laser light with different polarisations with respect to the applied electric field. The figures above are the calculated Rydberg Stark spectra for the 20(2) manifold, accessed *via* the $v' = 0, N' = 0$ rovibrational level of the intermediate state of NO at field strength of 300 V cm^{-1}. The molecular Stark manifolds are labelled according to the $n(N^+)$ nomenclature, where n is the principal quantum number and N^+ is the rotational quantum number of the ion core. (A) is calculated for parallel-polarised (m = 0) laser light, where the maxima of the intensities of l character lie at the edges of the manifold. When using perpendicularly polarised ($|m| = 1$) laser light the maximum intensity lies in the middle of the manifold (B).

On moving from the Hydrogen atom to more complex systems one must consider the complex potential the electron feels in the core region, which is reflected in the quantum defect value. The potential of the core lifts the l degeneracy in zero field. The lower l states therefore do not mix in with the rest of the manifold until higher fields. The perturbation is especially large for the low l ($l \leq 3$)

Rydberg states which encounter the core more frequently than the high l $(l \geq 4)$ Rydberg states and causes the loss of degeneracy. The high l $(l \geq 4)$ states with quantum defects of almost zero remain degenerate. At low electric fields, states with high l character are still degenerate and so are hydrogenic in character. These experience a pure Columbic potential and, as the electric field increases, they form into a Stark manifold. In comparison, low l states which are no longer degenerate are only weakly coupled to the Stark manifold. Initially as the electric field strength increases the low l states gradually mix into the Stark manifold and all states undergo a linear Stark shift. In figure 1.7 an example of a multielectron Stark manifold for NO is presented.

At the Inglis-Teller Limit, the extreme red and blue states of the n and n + 1 manifolds do not cross like in the Hydrogen atom but create an avoided crossing due to the coupling at the core [2,34]. At these avoided crossings the Rydberg state population is transferred from the initial n state to the n + 1 or n - 1 state. The amount of population transferred is strongly dependent on how quickly the applied electric field rises from zero field to the ionising field. It is important to understand how these avoided crossings are traversed, especially when considering results obtained from selective field ionisation. These are reported in chapter 5.

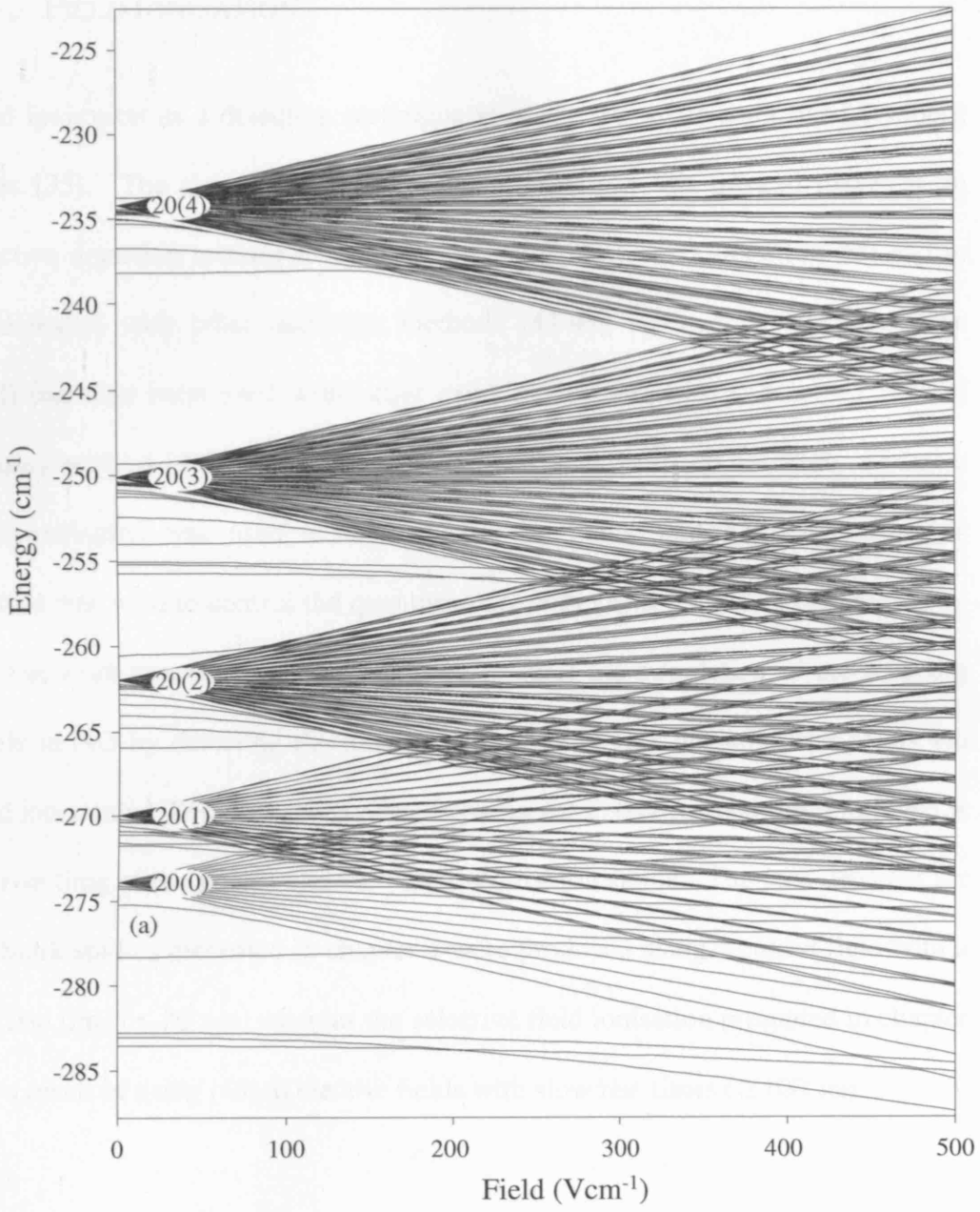

Figure 1.7 A region of the NO Stark map calculated to show the 20(0), 20(1), 20(2), 20(3) and 20(4) manifolds. At zero field, states with low angular momentum quantum number ($l < 3$) are lower in energy compared to high l states and thus join a neighbouring manifold at higher electric field strengths. For example, (a) the 20*d*(0) Rydberg state at -275 cm^{-1} joins the 20(0) manifold at approximately 170 V cm^{-1}.

1.6 FIELD IONISATION

Field ionisation as a detection technique is ideally suited to long lived Rydberg states [35]. The simplicity and experimental ease of this method makes it an effective detection technique for Rydberg states when used alone [36-40] and in combination with other detection methods [41-43]. Selective field ionsiation (SFI) has also been used with other experimental methods such as the optical Ramsey method [44], for example in our own work [45]. In the work, selective field ionisation was used as the detection technique and the optical Ramsey method was used to control the quantum state composition of wave packets in Na. For the work presented in this thesis we monitor the population of the Rydberg levels in NO by detecting the ions and electrons, which are produced solely *via* field ionisation. The major difference between the detection methods employed is the rise time of the pulsed electric field used for ionisation. The ions detected for the Stark studies presented in chapter 4 were produced using a pulsed field with a fast rise time (≤ 20 ns), whereas the selective field ionisation presented in chapter 5 is a result of using pulsed electric fields with slow rise times (≥ 100 ns).

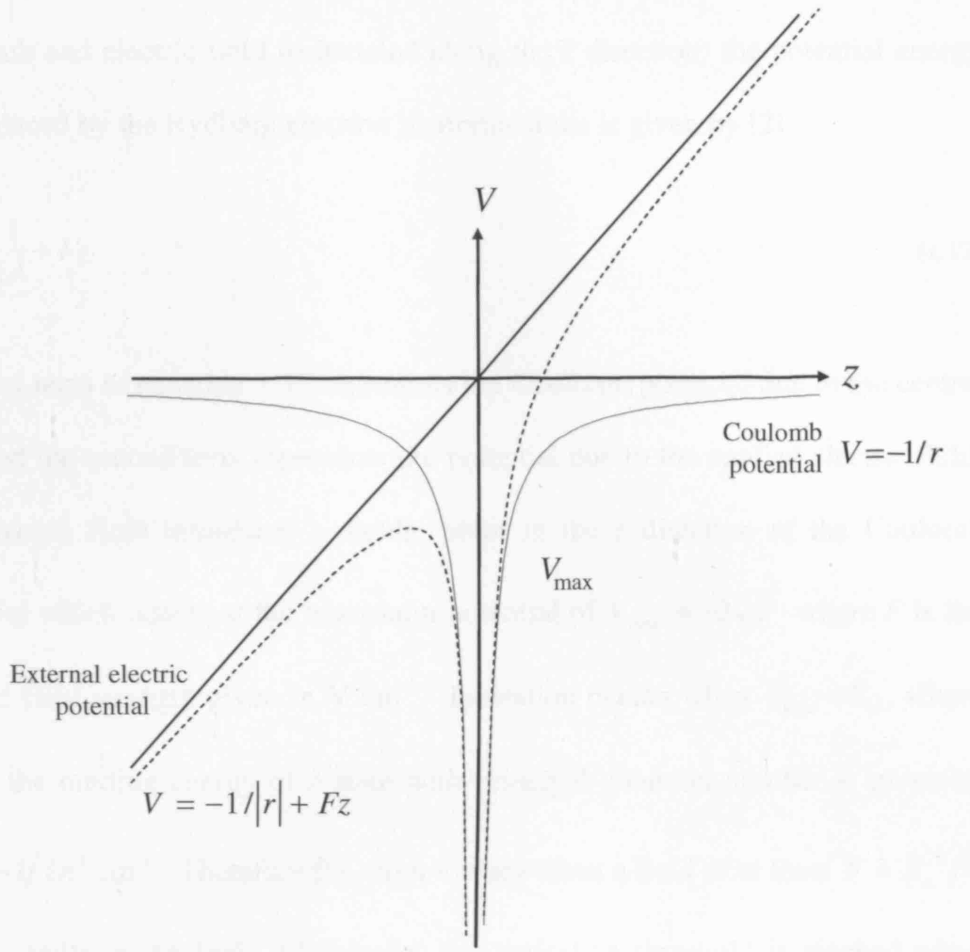

Figure 1.8 A schematic diagram of a Coulomb potential of an electron (solid line). Applying an electric field in the z direction, tips the potential (dashed line) and introduces a saddle point to the Coulomb potential at $V_{max} = -2\sqrt{F}$, where F is the applied field strength given in $V\ cm^{-1}$. An electron with energy greater that this saddle point can escape over the potential barrier and ionise classically, or it may escape the potential *via* tunnel ionisation if it is slightly below the saddle point.

The interaction of a Rydberg system with an electric field effectively lowers the ionisation potential and this is shown in figure 1.8, where r is the radial distance of the electron from the core and F is the applied electric field. In a combined

Coulomb and electric field (orientated along the z direction) the potential energy experienced by the Rydberg electron in atomic units is given by [2]

$$V = -\frac{1}{|r|} + Fz \tag{1.17}$$

The first term in equation 1.17 represents the Coulomb potential due to the central core and the second term represents the potential due to the applied electric field. The electric field introduces a saddle point in the z direction of the Coulomb potential which occurs at the maximum potential of $V_{max} = -2\sqrt{F}$ where F is the applied field strength given in V cm^{-1}. Ionisation occurs when $V_{max} = E_n$, where E_n is the binding energy of a state with principal quantum number n, given by $E_n = -1/2n^2$ cm^{-1}. Therefore the atom ionises when a field of at least $F = E_n^{\,2}/4$ (atomic units) is applied. Classically, the ionisation threshold is reached when $F = 1/16n^4$ (atomic units) and the threshold energy, E_{sp} at which the electron can escape over the saddle point, is $E_{sp} = -6.12\sqrt{F}$ cm^{-1} [46]. When a fast rising pulsed electric field is applied, the barrier drops instantly such that all states with energy greater then E_{sp} ionise simultaneously. However if the field is ramped up slowly, the barrier is gradually lowered and states with energy greater then E_{sp} ionise and are detected at different times (figure 1.9). This is the basis of selective field ionisation.

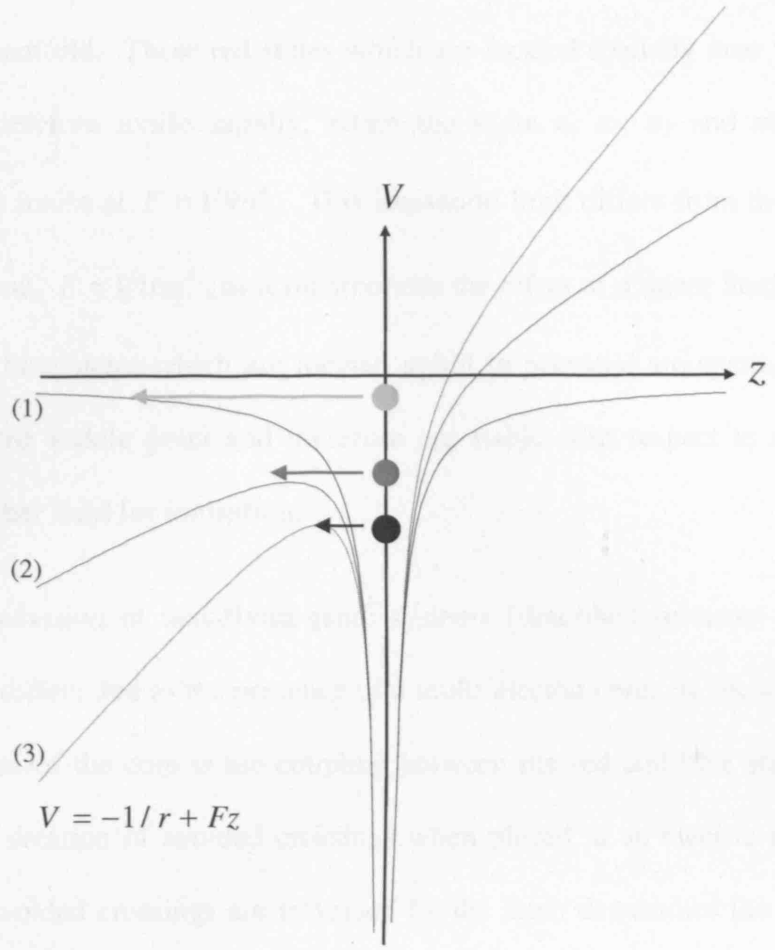

Figure 1.9 A schematic diagram illustrating the mechanism of selective field ionisation. As the applied electric field is ramped slowly (from (1) to (3)) to higher field strengths the barrier is gradually lowered and states with energy greater then $E_{sp} = -6.12\sqrt{F}$ ionise and are detected at different times. The filled circles represent the electrons in Rydberg states at different energies.

When a field greater than $E_n^{\,2}/4$ is applied, tunnelling ionisation becomes important. In the Hydrogen atom, field ionisation of the Rydberg states occur *via* this process, in which the electron escapes the atom by tunnelling through the potential barrier produced by the applied field. Stark states that are high in energy (blue states) tend to ionise at higher fields compared to the low energy (red) states

in a Stark manifold. These red states which are located spatially near the saddle point and therefore ionise rapidly, retain the same n, n_1, n_2 and m quantum numbers and ionise at $F = 1/9n^4$. This ionisation limit differs from the classical ionisation limit, $F = 1/16n^4$, as it incorporates the effect of a linear Stark shift. In contrast the blue states which are located uphill in potential are spatially further away from the saddle point and therefore are stable with respect to decay and require a higher field for ionisation.

The field ionisation of non-Hydrogenic systems (described in terms of energy level maps) differs due to the presence of a multi-electon core. A consequence of the finite size of the core is the coupling between the red and blue states which leads to the creation of avoided crossings when placed in an electric field. The way these avoided crossings are traversed by the atom determines the ionisation mechanism. The traversal of an avoided crossing is dependent on the how fast the applied electric field pulse rises from zero field to the ionising field. Therefore it is necessary to understand how the atom evolves from zero field to the high ionising (Stark) fields.

As a ramped electric field is applied the evolution of the atom can be described by considering three regions of electric field strength. The low field region encountered by the atom is when l is no longer considered a good quantum number. In this region the spacing between Stark states is equal to the zero field spacing between l states and the Stark effect is considered to be stronger then the spin orbit interaction but not strong enough that the states cross. When this field

is reached in a time which is long compared to the inverse of the zero field splitting, the passage is adiabatic.

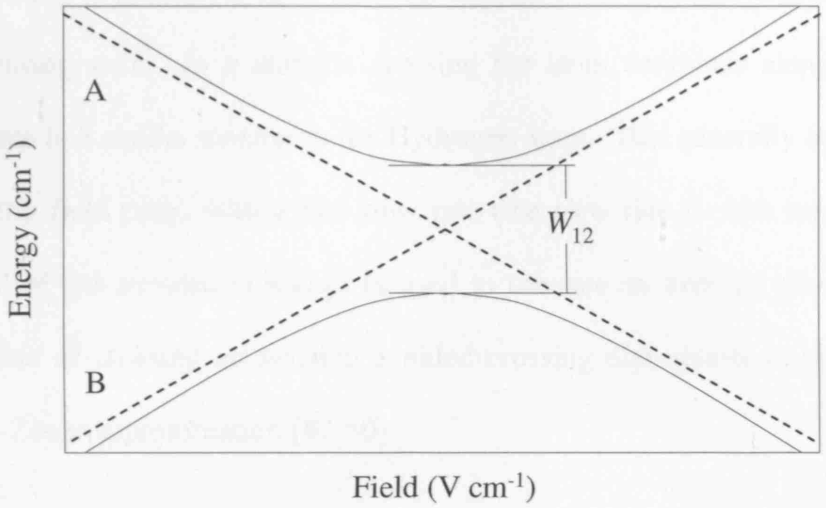

Figure 1.10 A schematic diagram of an isolated avoided crossing in a molecular system. The solid lines indicate an adiabatic crossing and the dashed lines represent a diabatic traversal. The probability of a diabatic traversal is given by the Landau–Zener approximation, equation 1.17. The way an avoided crossing is traversed is dependent on the slew rate of the applied electric field pulse and the size of the avoided crossing, w_{12}.

The high field limit considers the behaviour of the atom in a field range of (Inglis-Teller) $F > 1/3n^5$ but below the classical field ionisation limit. In this region, avoided crossings between adjacent n manifolds of same m are encountered. Figure 1.10 shows a schematic of an isolated avoided crossing. An avoided crossing can be traversed either adiabatically (solid line) or diabatically (dashed line). In general at the crossing, population crosses partially adiabatically and

diabatically. The relative amount is dependent on the slew rate of the applied field pulse.

When an avoided crossing is crossed adiabatically the population crosses into the neighbouring n manifold, such that the excited atom assumes character of the neighbouring state. In a diabatic crossing the atom continues along the same Stark state in a similar manner to the Hydrogen atom. This generally occurs when an electric field pulse with a fast slew rate (the slew rate is with respect to the traversal of the avoided crossing) is used to traverse an avoided crossing. The probability of crossing an isolated avoided crossing diabatically is given by the Landau-Zener approximation [47-50]

$$P_{dia} = \exp\left[-\frac{2\pi|V_{12}|^2}{\hbar \cdot (dW_{12}/dt)}\right] \tag{1.18}$$

where V_{12} is the coupling matrix element of the interaction which is the root of an avoided crossing. A strong coupling between states results in a small energy gap at the avoided crossing, leading to a greater probability of a diabatic crossing. In equation 1.18, W_{12} is the energy difference between the two states, which is dependent on the energy of the states at zero field, and also on the strength of the electric field at the avoided crossing. The slew rate of the applied electric field pulse can be expressed by rewriting the time derivative as

$$\frac{dW_{12}}{dt} = \dot{F} \cdot \left|\frac{dE_1}{dF} - \frac{dE_2}{dF}\right| \tag{1.19}$$

where the gradient of the state involved is given by dE/dF and the slew rate is $\dot{F}$. It is evident from equation 1.18 that the traversal of an avoided crossing is dependent on the slew rate of the applied electric field pulse and the energy gap between the two states at the crossing. The energy gap between the two states in an avoided crossing is a reflection of the core coupling between the two states [34,51,52]. The weaker this coupling, the smaller the energy gap at the crossing and the greater the probability of a diabatic crossing for a given slew rate. The traversal of an avoided crossing is directly dependent on the rate at which the field pulse is applied. If the field is swept through the avoided crossing in a time much shorter than the inverse of the energy gap then the passage through the avoided crossing a diabatic. If the field is swept through the avoided crossing in a time much longer then the inverse of the energy gap then the path taken is adiabatic. The result of such an adiabatic crossing is that the atom assumes the character of the other state involved in the crossing. However if the crossing is traversed in a time comparable to the inverse of the energy gap, the passage will neither be wholly diabatic or adiabatic.

The final region crossed by the atom along the Stark manifold is in the very high field above the classical field limit of $F \geq 1/16n^4$. In Hydrogen, states always ionise diabatically irrespective of the slew rate of the pulsed field as there is no coupling at the core, so states always cross (figure 1.11B). For non-hydrogenic systems two possible forms of ionisation are possible. Hydrogenic ionisation occurs when a pulsed field with a fast enough slew rate is applied and usually for states with high n (>60) [53,54].

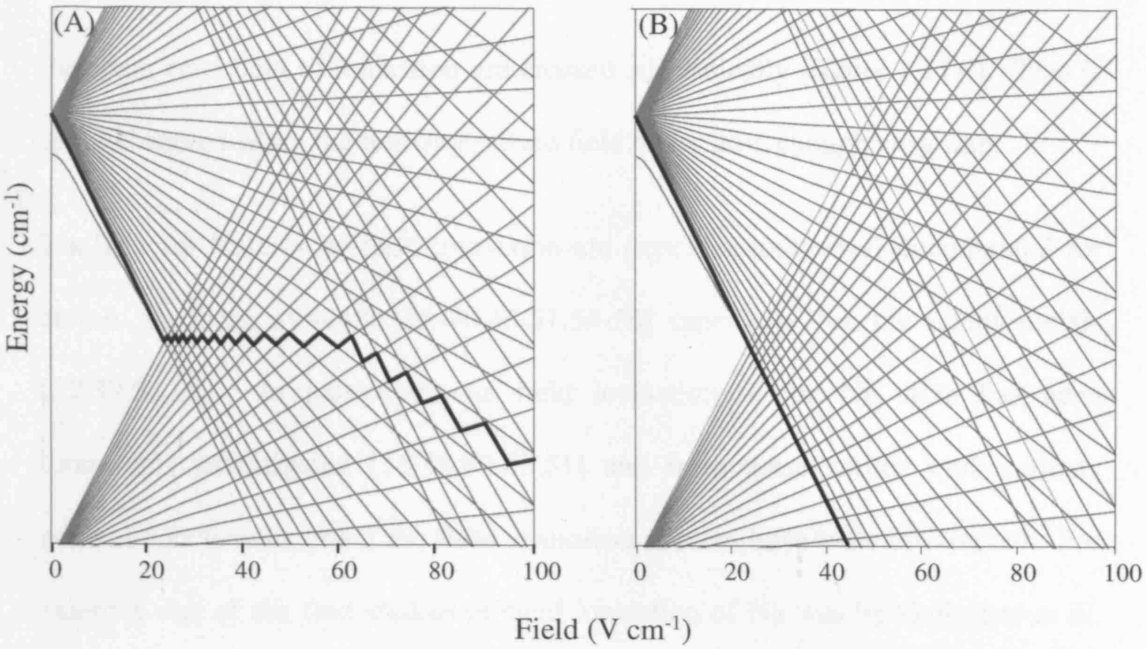

Figure 1.11 Schematic Stark map illustrating the two extreme ionisation routes possible for an electron excited into a Rydberg Stark manifold. (A) shows a pure adiabactic route towards the ionisation continuum, such that all avoided crossings encountered are traversed adiabatically. In comparison figure (B) illustrates a pure diabatic route to the ionisation continuum which results in ionisation at higher electric field strength compared to a pure adiabatic ionisation.

These blue states in Hydrogen can be very stable with respect to decay *via* field ionisation even though they are energetically degenerate with the lower n red continua states. In other atoms this is not the case, the presence of the finite core results in the coupling of the blue states with the red continuum states at the ionic core. As a result the blue states ionise at lower fields compared to the blue states in the Hydrogen atom. This type of ionisation can be considered as a form of autoionisation and occurs at electric fields between the classical field limit, $1/16n^4$ and hydrogenic limit, $1/9n^4$. Ionisation features observed in this region are a result of a combination of diabatic and adiabatic traversal of avoided crossings. Pure adiabatic ionisation occurs at $F = 1/16n^4$ and when all regions

between zero field to ionisation are crossed adiabatically (figure 1.11A). This is only observed when the ionising pulsed field has a slow enough slew rate.

The general features of field ionisation are experimentally well documented for atomic Rydberg systems [36-40,45,51,54-58] especially for the alkali metals [37,39,54,58]. In particular, the field ionisation of the Na atom has been thoroughly investigated [36,38,40,45,51] and from these earlier studies many general conclusions about the field ionisation process have been discovered. For example one of the first studies of field ionisation of Na was by Gallagher *et al.* [36] who discovered that upon exciting the *s*, *p* and *d* Rydberg states in Na, multiple ionisation field thresholds were observed. This was as a result of resolving the different m_l states associated with each l state, for example the ionisation field threshold for the *p* state contained two limits, one for $m_l = 0$ and the other for $m_l = 1$. They were able to resolve these thresholds by applying an increasing electric field pulse to ionise the atoms over a period of time from 0 V cm^{-1} to some peak value. As the ionising field increased in time it reached each of the ionisation thresholds at different times. In the follow up report [51], a more detailed analysis of the assignment of these ionisation field thresholds was given. The thresholds were assigned according to what extent the passage to ionisation was adiabatic or diabatic, and were achieved by considering the route in two field regions, low to intermediate field and intermediate to high field. In the low field region, before any crossing between neighbouring Stark states, they found that the Na atoms passed adiabatically when a field pulse with a slew rate of 2×10^{10} V cm^{-1} s^{-1} was used. In the second part of their experiments, the passage to the higher ionising field region from intermediate fields for the $n = 17$ Stark

map of Na was investigated. In this region, due to the overlap of Stark states belonging to different Stark manifolds, the route to ionisation was significantly more complicated. For that reason a simplified model was used to determine whether the passage to ionisation, in general, was adiabatic or diabatic. This involved considering only the extreme components of the n = 17 Stark map. In this method, by obtaining the energy and field at which ionisation occurred for these extreme states, they were able to determine whether the passage was mainly either adiabatic or diabatic using an electric field pulse with a slew rate of 2×10^{10} V cm^{-1} s^{-1}. Using these values of energies and field thresholds as a comparison, they were able to ascertain whether other states ionised along a mainly adiabatic or diabatic route.

The first experiment to observe evidence of a diabatic signal in a field ionisation spectrum was in Na by Jeys *et al.* [38]. (Previous experiments in Na reported that the route to ionisation was mainly adiabatic when applying an increasing field). They observed data showing both adiabatic and diabatic ionisation thresholds recorded using pulsed electric fields rising from 0 – 1100 V cm^{-1} in 1 μs (figure 1.12(a)). In figure 1.12(a) field ionisation data for the *d* states of sodium with n = 30, 32, 24 and 36 are presented and show two major ionisation threshold limits. In figure 1.12(b) the corresponding passages to give these ionisation thresholds are shown. They also observed similar ionisation spectra for the *s* and *p* states of Na. In a similar manner to the experiments by Gallagher *et al.* [36,51], the low field threshold, when slewed through with a slower rising pulse showed additional structure as a result of different m_l states. This low field threshold was assigned as a result of an adiabatic route to ionisation occurring at the classical field ionisation

limit. The higher field ionisation threshold is enough to ionise the lowest energy state of the $m_l = 2$ manifold, and results in states with $m_l = 2$ traversing the Stark map from low field to high field along a diabatic route. From these results they have shown that as the m_l value increases, so does the probability of a diabatic passage to ionisation. Littman *et al.* [59] showed that the strength of interaction between the various manifolds was strongly dependent on m_l. The larger the m_l value the smaller the interaction between states of same m_l at a crossing, and therefore a greater probability of a diabatic traversal. The results in figure 1.12(a) also show an evolution from a mainly adiabatic ionisation to both adiabatic and diabatic, and this occurs as n increases with a field pulse increasing from 0 – 1100 V cm^{-1} in 1 μs. This is an indication that at a given slew rate of an electric field pulse, for high n there is less interaction between two states at a crossing, leading to a greater probability of a diabatic transition. The method they used to confirm the diabatic nature of the signal at the higher fields involved changing the laser polarisation with respect to the field. By changing the polarisation to be parallel with respect to the applied electric field and according to the distribution of the different m_l states in the manifold (equation 1.15), states with high m_l (>1) were not excited. Upon applying a slowly rising pulse there was no high field signal observed, thus confirming the diabatic character of the signal.

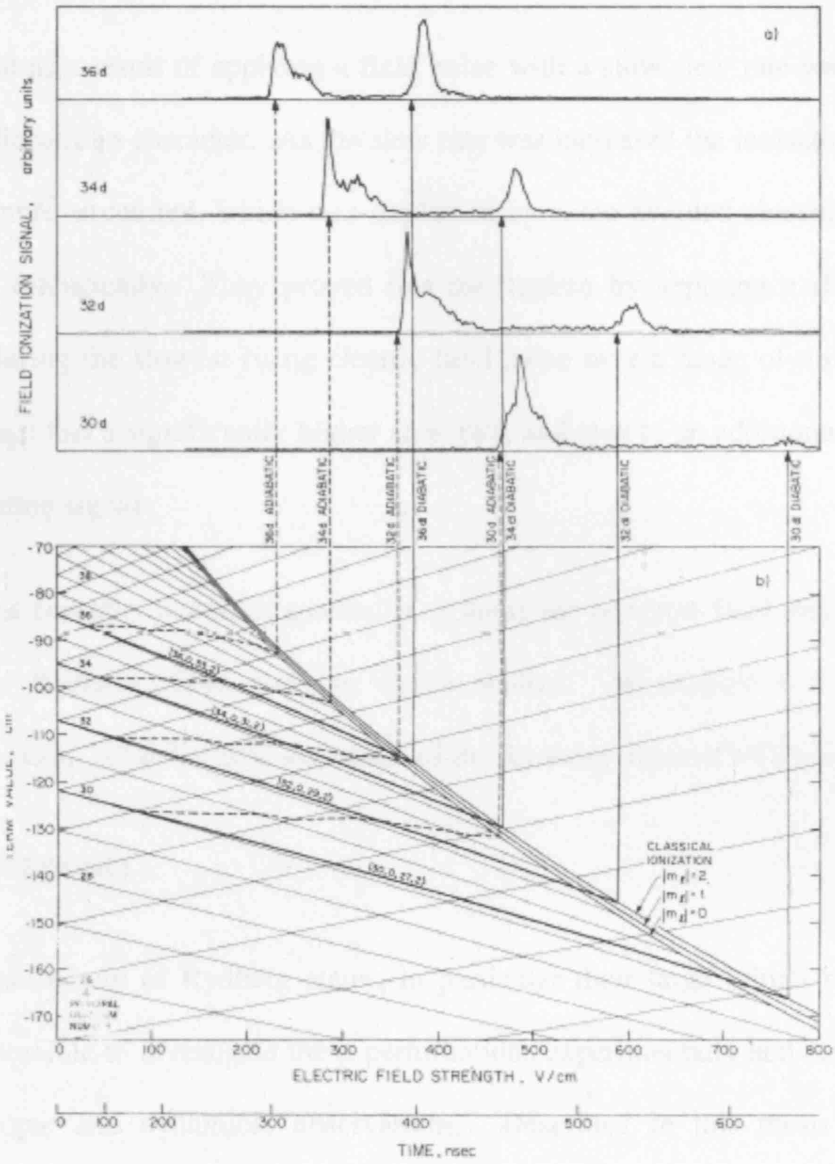

Figure 1.12 Figure taken from Jey *et al.* [38] showing the (a) field ionisation profiles for the *d* Rydberg states with n = 30, 32, 34 and 36 of Na using an electric field pulse increasing from 0 – 1100 V cm-1 in 1 μs. (b) Illustrates the corresponding passage along a Stark map, where the light lines are the extreme members of the m_l = 0 manifolds, the dotted lines are the adiabatic routes and the dark line are the diabatic paths to ionisation.

Another technique employed to determine the diabatic nature of a signal was reported by McMillan *et al.* [60]. They presented the field ionisation signals for the *ns* and *nd* states of Na after applying field pulses with different slew rates.

The signal as a result of applying a field pulse with a slow slew rate was almost purely adiabatic in character. As the slew rate was increased the ionisation signal became more structured, which was explained by some avoided crossings being traversed diabatically. They proved this mechanism by applying a sharp step voltage during the slowest rising electric field pulse over a range of times. The step voltage had a significantly higher slew rate, and lead to an additional peak in the ionisation signal.

Due to the complex nature of molecular systems the selective field ionisation of molecular Rydberg states has yet to be studied. In chapter 5 a detailed investigation of selective field ionisation of the Rydberg states of NO is reported.

1.7 SUMMARY

The unique nature of Rydberg states, in particular their large orbital radii, has made it possible to investigate these perturbations experimentally and reveal new spectroscopic and dynamical observations. Described in this thesis are the perturbations incurred by molecular Rydberg systems when exposed to external electric fields. In chapter 4 new spectroscopic results obtained from applying static electric fields to the Rydberg states of NO are reported. Applying a ramped electric field to these Rydberg states allows a degree of selectivity and these results are presented in chapter 5. The experimental set-up used to obtain all the results presented in this thesis is described in chapter 2. Crucial to the interpretation of these results is the spectroscopic details of the molecule, NO, and this is described first in chapter 3.

1.8 REFERENCES

1. H. E. White, *Introduction to Atomic Spectra.* McGraw-Hill Book Company, 1934.
2. T. F. Gallagher, *Rydberg Atoms.* CUP, 1994.
3. G. Herzberg and C. Jungen, *Journal Of Chemical Physics* **77** (12), 5876 (1982).
4. P. M. Dehmer and W. A. Chupka, *Journal Of Chemical Physics* **65** (6), 2243 (1976).
5. G. Herzberg, *Journal of Molecular Spectroscopy* **33** (1), 147 (1970).
6. M. J. J. Vrakking and Y. T. Lee, *Journal Of Chemical Physics* **102** (22), 8818 (1995).
7. S. Fredin, D. Gauyacq, M. Horani, C. Jungen, G. Lefevre, and F. Masnou-Seeuws, *Molecular Physics* **60** (4), 825 (1987).
8. A. Ten Wolde, PhD Thesis, University of Amsterdam (1990).
9. R. S. Minns, R. Patel, J. R. R. Verlet, and H. H. Fielding, *Physical Review Letters* **91** (24) (2003).
10. R. S. Minns, J. R. R. Verlet, L. J. Watkins, and H. H. Fielding, *Journal Of Chemical Physics* **119** (12), 5842 (2003).
11. R. A. L. Smith, V. G. Stavros, J. R. R. Verlet, H. H. Fielding, D. Townsend, and T. P. Softley, *Journal Of Chemical Physics* **119** (6), 3085 (2003).
12. H. H. Fielding, R. A. L. Smith, V. G. Stavros, and J. R. R. Verlet, *Abstracts Of Papers Of The American Chemical Society* **221**, U251 (2001).

13. R. A. L. Smith, J. R. R. Verlet, E. D. Boleat, V. G. Stavros, and H. H. Fielding, *Faraday Discussions*, 63 (2000).

14. V. G. Stavros, J. A. Ramswell, R. A. L. Smith, J. R. R. Verlet, J. Lei, and H. H. Fielding, *Physical Review Letters* **84** (8), 1847 (2000).

15. B. J. Lyons, D. W. Schumacher, D. I. Duncan, R. R. Jones, and T. F. Gallagher, *Physical Review A* **57** (5), 3712 (1998).

16. H. Maeda, W. Li, and T. F. Gallagher, *Physical Review Letters* **85** (24), 5078 (2000).

17. D. W. Schumacher, D. I. Duncan, R. R. Jones, and T. F. Gallagher, *Journal of Physics B-Atomic Molecular and Optical Physics* **29** (11), L397 (1996).

18. D. W. Schumacher, B. J. Lyons, and T. F. Gallagher, *Physical Review Letters* **78** (23), 4359 (1997).

19. A. Tenwolde, L. D. Noordam, A. Lagendijk, and H. B. V. Vandenheuvell, *Physical Review Letters* **61** (18), 2099 (1988).

20. J. R. R. Verlet, V. G. Stavros, R. S. Minns, and H. H. Fielding, *Physical Review Letters* **89** (26), 263004 (2002).

21. J. R. R. Verlet, V. G. Stavros, R. S. Minns, and H. H. Fielding, *Journal of Physics B-Atomic Molecular and Optical Physics* **36** (17), 3683 (2003).

22. R. A. L. Smith, J. R. R. Verlet, E. D. Boleat, V. G. Stavros, and H. H. Fielding, *Faraday Discussions* **115**, 63 (2000).

23. V. G. Stavros, J. A. Ramswell, R. A. L. Smith, J. R. R. Verlet, J. Lei, and H. H. Fielding, *Physical Review Letters* **83** (13), 2552 (1999).

24. D. Gauyacq, A. L. Roche, M. Seaver, S. D. Colson, and W. A. Chupka, *Molecular Physics* **71** (6), 1311 (1990).

25. A. L. Goodgame, H. Dickinson, S. R. Mackenzie, and T. P. Softley, *Journal Of Chemical Physics* **116** (12), 4922 (2002).

26. J. Jortner and M. Bixon, *Journal Of Chemical Physics* **102** (14), 5636 (1995).

27. M. J. J. Vrakking, *Journal Of Chemical Physics* **105** (17), 7336 (1996).

28. R. Patel, N. J. A. Jones, and H. H. Fielding, *Journal of Physics B-Atomic Molecular and Optical Physics* **40** (7), 1369 (2007).

29. W. A. Chupka, *Journal Of Chemical Physics* **99** (8), 5800 (1993).

30. W. A. Chupka, *Journal Of Chemical Physics* **98** (6), 4520 (1993).

31. C. Bordas, P. F. Brevet, M. Broyer, J. Chevaleyre, P. Labastie, and J. P. Perrot, *Physical Review Letters* **60** (10), 917 (1988).

32. R. Patel, N. J. A. Jones, and H. H. Fielding, *Journal of Physics B-Atomic Molecular and Optical Physics* **40**, 1369 (2007).

33. C. H. Greene and C. Jungen, *Advances In Atomic And Molecular Physics* **21**, 51 (1985).

34. M. Gatzke, J. R. Veale, W. R. Swindell, and T. F. Gallagher, *Physical Review A* **54** (3), 2492 (1996).

35. D. H. Tuan, S. Liberman, and J. Pinard, *Optics Communications* **18** (4), 533 (1976).

36. T. F. Gallagher, L. M. Humphrey, R. M. Hill, and S. A. Edelstein, *Physical Review Letters* **37** (22), 1465 (1976).

37. A. Gurtler and W. J. van der Zande, *Physics Letters A* **324** (4), 315 (2004).

38. T. H. Jeys, G. W. Foltz, K. A. Smith, E. J. Beiting, F. G. Kellert, F. B. Dunning, and R. F. Stebbings, *Physical Review Letters* **44** (6), 390 (1980).

39. F. Robicheaux, C. Wesdorp, and L. D. Noordam, *Physical Review A* **62** (4), 043404 (2000).

40. J. L. Vialle and H. T. Duong, *Journal of Physics B-Atomic Molecular and Optical Physics* **12** (8), 1407 (1979).

41. J. Ahn, D. N. Hutchinson, C. Rangan, and P. H. Bucksbaum, *Physical Review Letters* **86** (7), 1179 (2001).

42. S. N. Pisharody and R. R. Jones, *Physical Review A* **65** (3), 033418 (2002).

43. T. C. Weinacht, J. Ahn, and P. H. Bucksbaum, *Physical Review Letters* **80** (25), 5508 (1998).

44. L. D. Noordam, D. I. Duncan, and T. F. Gallagher, *Physical Review A* **45** (7), 4734 (1992).

45. R. E. Carley, E. D. Boleat, R. S. Minns, R. Patel, and H. H. Fielding, *Journal of Physics B-Atomic Molecular and Optical Physics* **38** (12), 1907 (2005).

46. T. W. Ducas, M. G. Littman, R. R. Freeman, and D. Kleppner, *Physical Review Letters* **35** (6), 366 (1975).

47. D. A. Harmin, *Physical Review A* **26** (5), 2656 (1982).

48. D. A. Harmin, *Physical Review Letters* **49** (2), 128 (1982).

49. D. A. Harmin, *Physical Review A* **56** (1), 232 (1997).

50. D. A. Harmin and P. N. Price, *Physical Review A* **49** (3), 1933 (1994).

51. T. F. Gallagher, L. M. Humphrey, W. E. Cooke, R. M. Hill, and S. A. Edelstein, *Physical Review A* **16** (3), 1098 (1977).

52. J. R. Rubbmark, M. M. Kash, M. G. Littman, and D. Kleppner, *Physical Review A* **23** (6), 3107 (1981).

53. Y. Kishimoto, M. Tada, K. Kominato, M. Shibata, S. Yamada, T. Haseyama, I. Ogawa, H. Funahashi, K. Yamamoto, and S. Matsuki, *Physics Letters A* **303** (4), 279 (2002).

54. M. Tada, Y. Kishimoto, M. Shibata, K. Kominato, S. Yamada, T. Haseyama, I. Ogawa, H. Funahashi, K. Yamamoto, and S. Matsuki, *Physics Letters A* **303** (4), 285 (2002).

55. F. G. Kellert, T. H. Jeys, G. B. McMillian, K. A. Smith, F. B. Dunning, and R. F. Stebbings, *Physical Review A* **23** (3), 1127 (1981).

56. K. B. Macadam, D. B. Smith, and R. G. Rolfes, *Journal of Physics B-Atomic Molecular and Optical Physics* **18** (3), 441 (1985).

57. J. H. M. Neijzen and A. Donszelmann, *Journal of Physics B-Atomic Molecular and Optical Physics* **15** (13), 1981 (1982).

58. T. F. Gallagher, B. E. Perry, K. A. Safinya, and W. Sandner, *Physical Review A* **24** (6), 3249 (1981).

59. M. G. Littman, M. L. Zimmerman, T. W. Ducas, R. R. Freeman, and D. Kleppner, *Physical Review Letters* **36** (14), 788 (1976).

60. G. B. McMillian, T. H. Jeys, K. A. Smith, F. B. Dunning, and R. F. Stebbings, *Journal of Physics B-Atomic Molecular and Optical Physics* **15** (14), 2131 (1982).

CHAPTER 2

EXPERIMENTAL SET-UP

ABSTRACT

This chapter presents the experimental set-up used to investigate the spectroscopy of the Rydberg states of NO in external dc electric fields and ramped electric fields. The lasers, vacuum apparatus, electronic timing devices and detection techniques are discussed. In all the experiments described in this thesis, field-ionisation is used to detect the Rydberg state population. The experiment described in chapter 4 involves excitation of the Rydberg states in the presence of static dc fields, which are then detected using a pulsed electric field with a fast rise time. In chapter 5 the Rydberg states are excited in zero field and the populations are detected using ramped electric field pulses.

2.1 INTRODUCTION

The Rydberg states of NO are accessed using a multiphoton excitation scheme. This involves excitation from the ground $X\,^2\Pi_{3/2}$ state of NO to the Rydberg states, *via* the intermediate $A^2\Sigma^+$ state, a technique known as resonance-enhanced multiphoton excitation. This is now a standard and widely used method of accessing the high-energy states of atoms and molecules that would otherwise be inaccessible using commercial light sources. Multiphoton processes have different selection rules to single photon processes and may also provide new information on the excited states. For example, transitions to excited states with the same parity as the ground state are accessible in a 2 or 4 photon process but not with a single photon. The selection rules for Rydberg state excitation in NO are discussed in Chapter 3.

In the experiments described in this thesis, a two photon process is used to excite high n electronic states. A frequency resolved experiment is a useful and accurate method of obtaining structural information about the system under investigation, and can also provide additional information about a system including the selection rules for various transitions. Frequency and time resolved experiments can be used to corroborate each other and often, frequency spectra are recorded to give detailed knowledge of states excited within a wave packet in a time resolved experiment. This was the original motivation for some of the investigations presented in this thesis, and is especially important when designing coherent control schemes and experiments which depend on accurate knowledge of the wave packet composition.

A constant dc electric field applied to a Rydberg system allows new structural information to be obtained from the frequency spectrum. States that are otherwise inaccessible in zero field can be accessed and investigated. The frequency spectra obtained are also very useful for determining the lifetimes of Rydberg states [1], where the lifetime of a state in a frequency spectrum is given by the width of the corresponding resonance peak. Work presented in this thesis utilises information obtained from frequency spectra with the added influence of a constant electric field.

2.2 EXPERIMENTAL SET-UP

2.2.1 LASER SYSTEM

The frequency spectra presented in this thesis were recorded using two tuneable dye lasers pumped by a single Nd:YAG laser. Figure 2.1 is a schematic diagram of the experimental set-up. The individual Rydberg states of NO are accessed *via* the well defined intermediate *A*-state, which is excited using a narrow bandwidth nanosecond laser pulse. The nanosecond laser pulse is generated from a tuneable nanosecond dye laser (Continuum ND6000) pumped by a Q-switched Nd:YAG laser (Continuum Powerlite 8010). The Nd:YAG pump laser generates pulses of light at 1064 nm and 6 ns duration, at a repetition rate of 20 Hz and a second harmonic (532 nm) power of 8 W (450 mJ per pulse). 40% of this beam is used to pump the first dye laser operating with Pyridine 1 dye (dissolved in ethanol) which generates light in the 645 – 730 nm range. The power of the light pulse

generated from the dye laser is 15 mJ per pulse and has an approximate bandwidth of 0.05 cm^{-1}. The UV light required to excite the intermediate state is generated by passing the red light through various non-linear crystals. First it is passed through a potassium dihydrogen phosphate (KDP) crystal which frequency doubles the light to give UV light (340.19 – 340.27 nm). The polarisation of this light is then rotated 90° with respect to the fundamental by a half waveplate. Both the fundamental and doubled light are then frequency mixed in a β-barium borate (BBO) crystal to generate the output in the UV. The process of frequency conversion is not 100% efficient, so the light is separated according to wavelength through a Pellin Broca prism in order to select the required frequency. For all the experiments reported in this thesis the frequency-tripled output is used to excite the $A^2\Sigma^+(v'=0,N',J') \leftarrow X^2\Pi_{3/2}(v''=0,J'')$ (226.77 – 226.89 nm) transition in NO.

The remaining 60 % of the Nd:YAG laser output is used to pump a second dye laser (Sirah Cobra Stretch). The light from this laser is used to excite NO from its intermediate state to the individual Rydberg states. The dye laser operates with DCM dye (dissolved in ethanol) to generate red light in the wavelength range 610 – 660 nm. This light is frequency doubled internally in a KDP crystal to produce UV light in the range 305 – 330 nm. The resultant UV light pulses are of 8 ns duration with a second harmonic of power 15 mJ per pulse and approximate bandwidth of 0.05 cm^{-1}. The Sirah output beam is combined with the Continuum

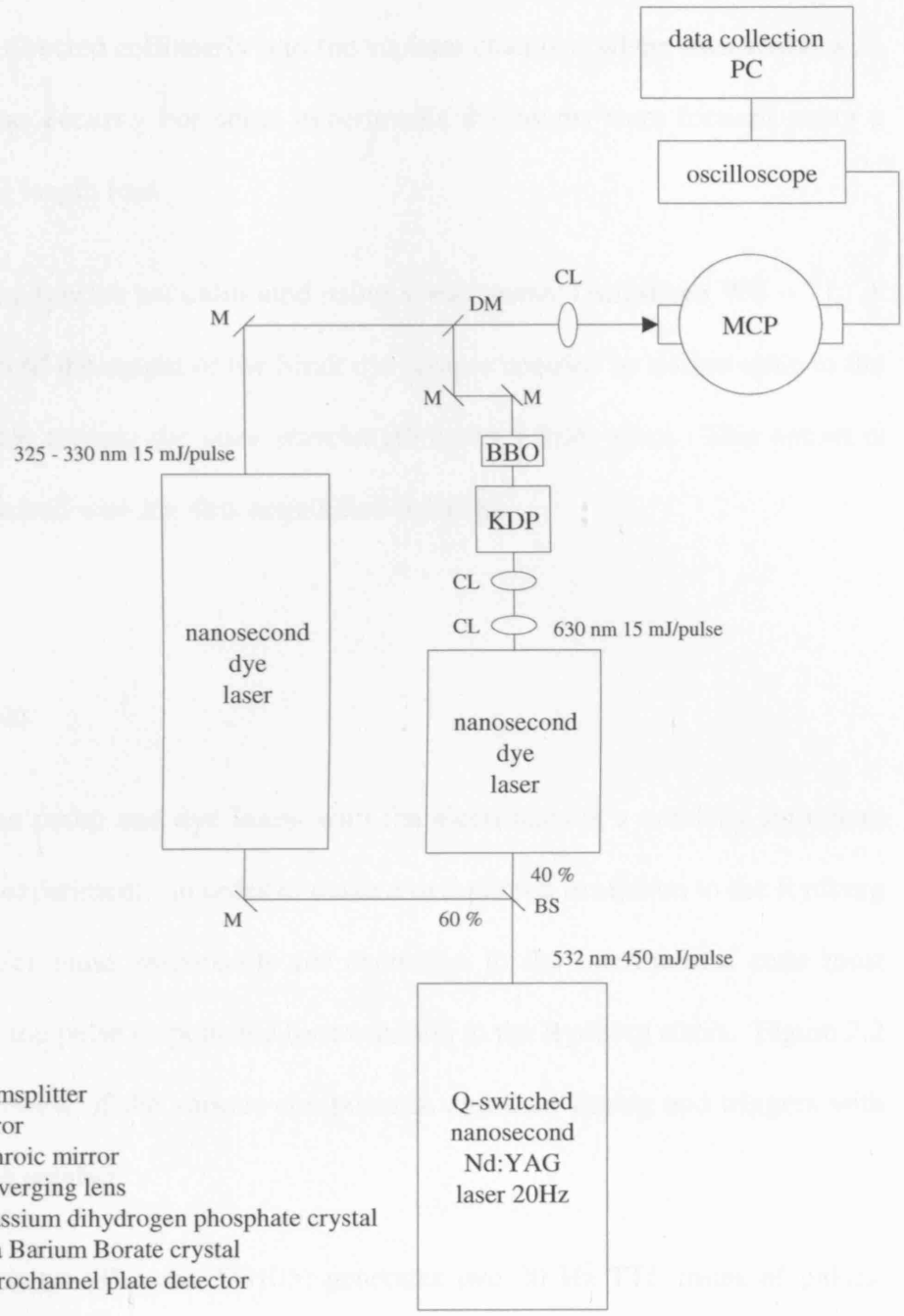

Figure 2.1 A schematic diagram of the laser set-up used to record frequency spectra in NO. A nanosecond Nd:YAG is used to pump two narrow bandwidth nanosecond dye lasers. The two beams are combined at a dichroic mirror and for some experiments focused into the chamber where they interact with the NO gas.

nanosecond light after a short time delay (approx 3 ns) at a dichroic beamsplitter before being directed collinearly into the vacuum chamber, where interaction with the sample gas occurs. For some experiments the beams were focused using a 300 mm focal length lens.

The frequency spectra are calibrated using a wavemeter (Angstrom WS – 7). A small fraction of the output of the Sirah dye laser is coupled by a fibre optic to the wavemeter that records the laser wavelength every 5 laser shots. This output is then synchronised with the data acquisition software.

2.2.2 TIMING

Timing of the pump and dye lasers with the electronics is a crucially important factor in the experiment. In order to make a two-photon excitation to the Rydberg states the laser pulse responsible for excitation to the intermediate state must arrive before the pulse responsible for excitation to the Rydberg states. Figure 2.2 gives an overview of the various components, and their timing and triggers with respect to one another.

A pulse generator (Thandar TG105) generates two 20 Hz TTL trains of pulses. One triggers the pulsed nozzle controller (IOTA ONE) 5 ms before any other piece of equipment. This has been optimised to ensure maximum gas flow at the same time that the pulses interact with the gas. After a 5 ms delay the second 20 Hz signal triggers the first digital delay generator (Stanford Research Systems DG535). There are four 'precisely-timed logic transitions' A, B, C and D and two

independent pulse output settings, $A \cup B$ and $C \cup D$. For the experiments described in this thesis, output A and pulse outputs $A \cup B$ and $C \cup D$ are used. Output A triggers a second delay generator (110 μs) whilst $A \cup B$ triggers the flash lamps (B = 266.67 μs) and $C \cup D$ triggers the Q-switch (D = 10 μs) of the nanosecond Nd:YAG. From the second DG535, output A triggers the digital oscilloscope (LeCroy Waverunner LT372) (A = 268.94 μs) for data collection and output $C \cup D$ triggers the pulsed electric field (D = 300.31 μs). The pulsed field is triggered to arrive 70 ns after the light pulses to allow completion of all possible excitation or decay processes, and also to ensure there is no electric field present during the interaction with the light pulse.

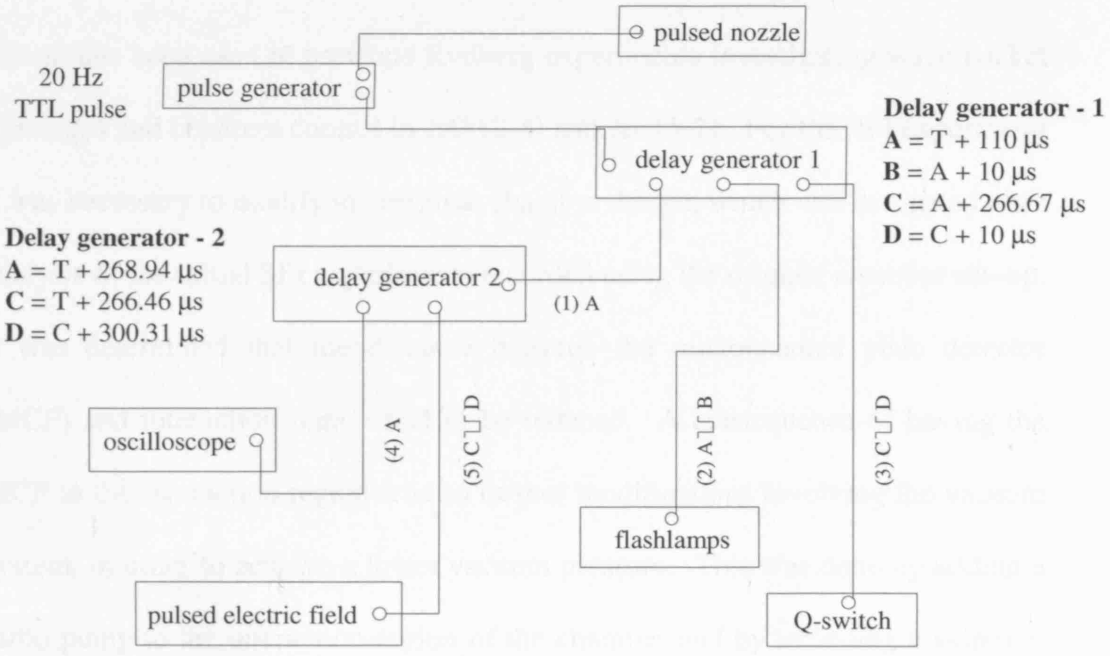

Figure 2.2 A circuit diagram illustrating the synchronisation of the lasers with various electronic components. Time delayed 20 Hz TTL pulse trains are generated and used to trigger the pulsed gas valve, the Nd:YAG laser as well as some data collection components.

The pulsed field is generated using a high voltage power supply (Stanford Research System PS350) with a commercial pulse generator (Direct Energy Incorporated PVE-4140). For the Stark experiments a second high voltage power supply is used to provide a constant dc voltage.

2.2.3 VACUUM CHAMBER

The experiments described in this thesis are all conducted using the same apparatus: however it was modified to accommodate the ramped or selective field ionisation (SFI) experiment (described in chapter 5). The first set-up, described below, was used to record the Stark spectra presented in Chapter 4. This chamber set–up has been used in previous Rydberg experiments investigating wave packet dynamics and coherent control in NO [2-4] and Xe [5-7]. For the SFI experiment it was necessary to modify the original chamber design, which was instigated after analysis of the initial SFI experiments recorded using the original chamber set–up. It was determined that the distance between the microchannel plate detector (MCP) and interaction region had to be reduced. A consequence of having the MCP in the interaction region lead to further modifications involving the vacuum system, in order to achieve a lower vacuum pressure. This was done by adding a turbo pump to the interaction region of the chamber and by including a skimmer between the pulsed nozzle and interaction region. In the following section a description of both chamber set-ups is provided, as well as the various connections and components found within the chambers.

2.2.3.1 VACUUM APPARATUS FOR STARK SPECTRA OF NO

The vacuum chamber itself consists of two sections: an interaction chamber and a detection chamber connected by a 20 cm time of flight (TOF) tube (figure 2.3(a)). The chamber is differentially pumped to high vacuum using a combination of diffusion, turbo and rotary pumps. The interaction part of the chamber is kept at a working pressure of 10^{-5} mbar using a 700 l s^{-1} diffusion pump (Edwards 160/700 M) when the pulsed nozzle is off. The interaction chamber and diffusion pump are connected *via* a butterfly valve which is used to isolate the chamber from the pump. The diffusion pump is backed by a two stage rotary pump (Edwards E2M18) at 10^{-3} mbar which is also used to rough out the chamber when pumping down from atmosphere.

The sample gas is pumped through a PTFE tube which is connected to the chamber *via* a stainless steel T piece tube. The T piece has several control valves which allows the removal of gas from the gas-line before venting the chamber. The steel tube is connected to an XYZ translation stage which is mounted on top of the interaction chamber. Connected to the end of the tube is a pulsed solenoid valve (General Valve Corporation 9-442-900) which pulses the sample gas at 20 Hz. When the valve is open the pressure within the chambers rises to 10^{-4} mbar. The amount of gas entering the chamber can be controlled by the length of time the valve is opened. The backing pressure of the gas is usually maintained at 2 bar with a valve pulse duration of 250 μs.

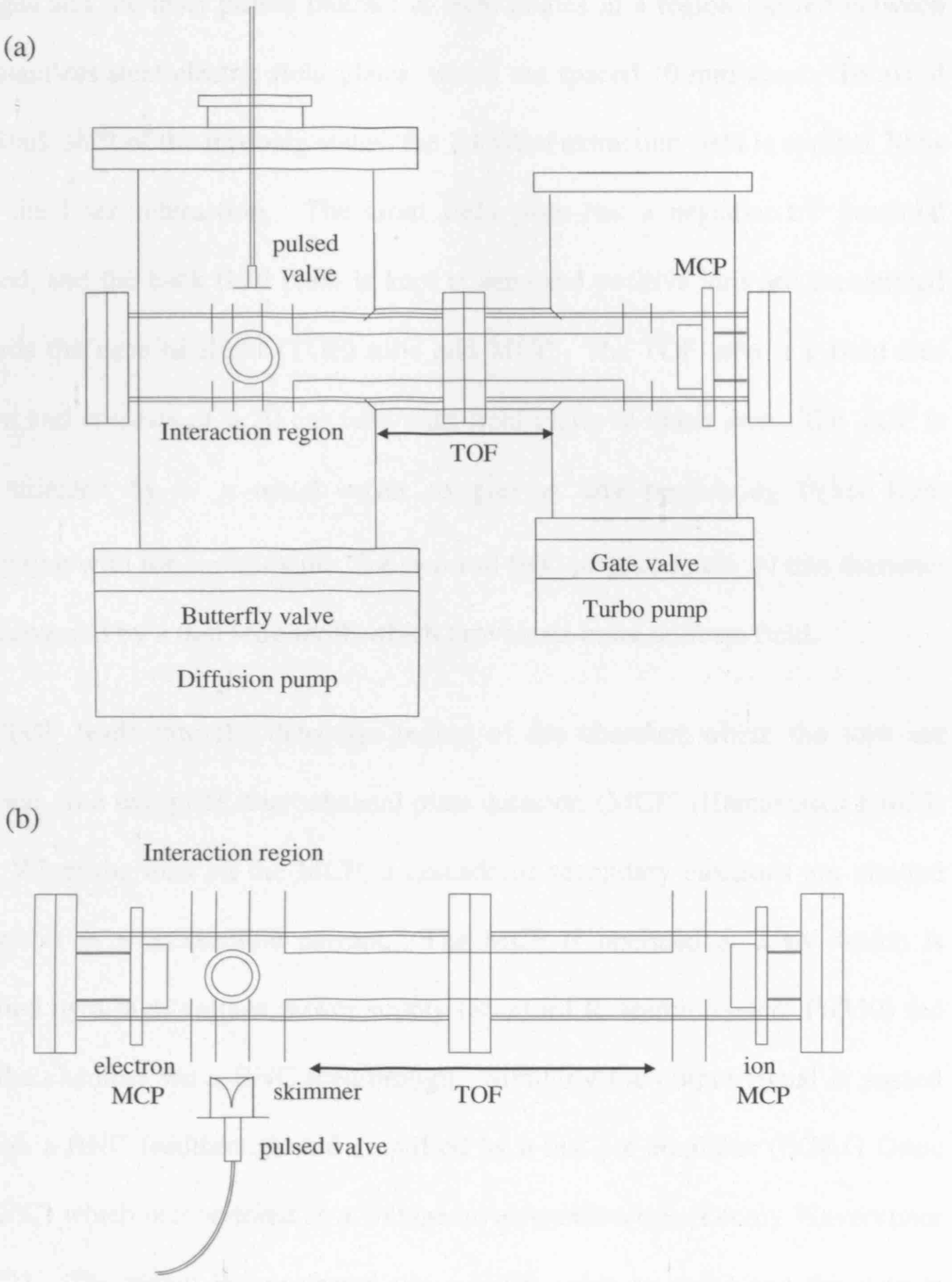

Figure 2.3 (a) The original vacuum chamber layout used for the Stark Experiments of NO. (b) Modified TOF layout used for the selective field ionisation experiments in NO. The interaction region houses the electron MCP whereas the ion MCP is located at the end of the TOF tube in the detection chamber. The gas is now passed through a skimmer where it interacts with the lasers beams at 90°.

The gas and the laser pulses interact at right angles in a region located between two stainless steel electric field plates, which are spaced 10 mm apart. To avoid any Stark shift of the Rydberg states, the 2 kV/cm extraction field is applied 70 ns after the laser interaction. The front field plate has a negative kV potential applied, and the back field plate is kept at zero and positive ions are accelerated towards the time of flight (TOF) tube and MCP. The TOF tube is a field free region and consists of a 20 cm tube with field plates at either end. The TOF is also shielded by a μ-metal cover to prevent any penetrating fields from interacting with the experiment. The two end field plates contain 10 mm diameter holes covered by a thin wire mesh which provides a more uniform field.

The TOF leads into the detection region of the chamber where the ions are detected on a two plate microchannel plate detector, (MCP) (Hamamatzu F4655-12). When the ions hit the MCP, a cascade of secondary electrons are emitted and result in a measurable current. The MCP is operated at 2 kV which is supplied by a high voltage power supply (Stanford Research System PS350) fed into the chamber *via* a BNC feedthrough. Similarly the output signal is passed through a BNC feedthrough and amplified by a fast pre-amplifier (EG&G Ortec VT120C) which is monitored as a voltage on an oscilloscope (Lecroy Waverunner LT372). The signal is transferred *via* a GPIB cable to a PC and the data is collected using a Labview (software) program. A typical NO ion signal is given in figure 2.4 as a function of oscilloscope time base.

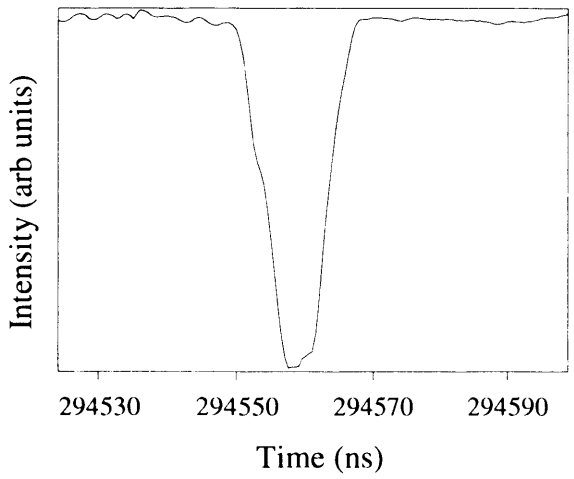

Figure 2.4 An oscilloscope screen dump of a typical NO ion signal plotted as a function of oscilloscope time base.

For some experiments electrons are detected and if this is the case, the polarity of the front plate is reversed to a negative charge and the MCP and its wiring is changed. An MCP must be operated in a high vacuum environment and for this reason the detection region of the chamber is maintained at 10^{-6}-10^{-7} mbar using a small turbo molecular pump (Edwards EXT-250). The turbo pump is backed to 10^{-3} mbar by the same rotary pump used to back the diffusion pump.

2.2.3.2 VACUUM APPARATUS FOR SFI OF NO

The major changes to the vacuum apparatus for the SFI experiment were to the interaction part of the chamber whilst the detection part was left mostly unchanged. The interaction region now houses an additional electron MCP (MCP wired for electron detection) while the detection chamber accommodates the ion MCP (MCP wired for ion detection). The distance between the electron MCP and

interaction region is 2.5 cm whilst the distance from the time of flight to the ion MCP is still 20 cm. A shorter time of flight to the electron MCP allows any electrons obtained through ionisation of NO molecules when using ramped field pulses, to be detected almost immediately and makes it easier to distinguish electrons ionised from different Rydberg states.

This major modification of positioning the electron MCP as close as possible to the interaction region required additional pressure conditions to be satisfied. The diffusion pump could not achieve the required 10^{-7} mbar pressure so a turbo pump was attached to the top of the interaction region of the chamber. This maintained the pressure in this region at 10^{-7} mbar. A skimmer was also introduced between these two regions. The skimmer separated the two regions which provided a sufficient pressure differential (10^{-5} to 10^{-7}) for gas flow from the valve to the interaction region.

Experimentally, ramped fields are generated by attaching a series of resistors using a BNC cable between a high voltage pulser and the field plate in the interaction region (figure 2.5).

The potential experienced by the field plate is modelled by the calculated potential of a charging capacitor

$$V(t) = V_0\left(1 - e^{\frac{-t}{CR}}\right) \tag{2.1}$$

where V_0 is the amplitude of the square pulse (2000 V), C is the capacitance in Farads, R is the resistance in Ohms and t is the time in seconds. The value of C is determined by best fit to the experimental data.

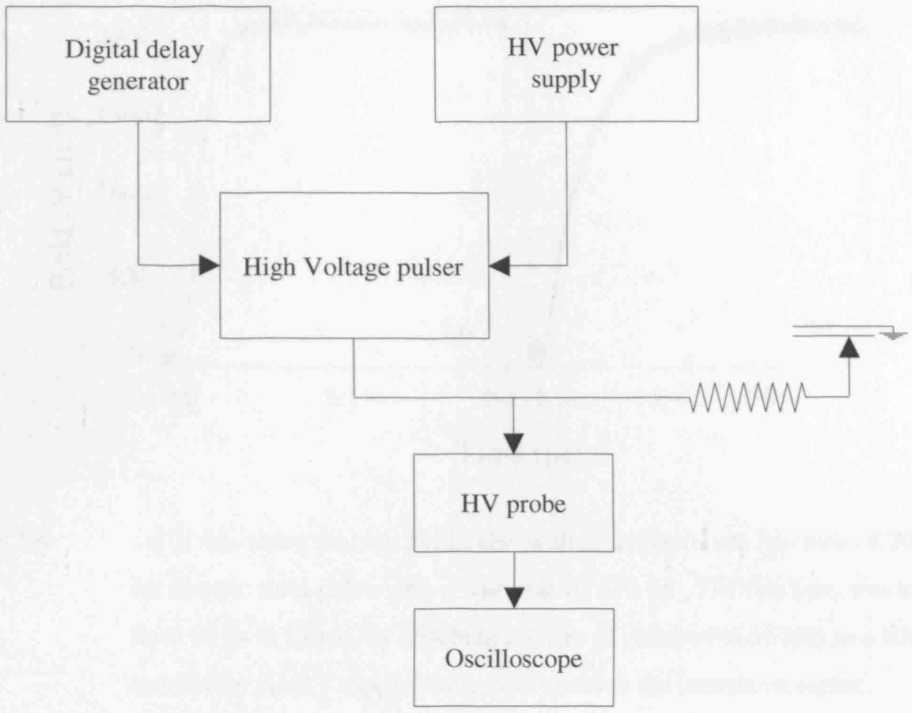

Figure 2.5 Schematic diagram showing the modifications to the high voltage pulser used to generate electric field pulses with varying rise times. A series resistor was added to the output of the high voltage pulser to increase the slew rate of the pulse, ranging from 6.9 to 1.3 V cm^{-1} ns^{-1}.

Figure 2.6 highlights the change in shape of the field pulse from a fast rise time of approximately 20 ns (a) to a rise time achieved when a series of resistors are attached to a BNC cable (b). This modification was obtained through a series of resistors with a combined sum of 6.56 kΩ, which increased the rise time to 870 ns. The signal is passed through a fast (< 1 ns) pre-amplifier and collected on a digital oscilloscope. The rise time is also recorded on the oscilloscope by attaching a high voltage probe to the field plate input voltage. In order to record an adequate SFI spectrum it was necessary to sum over 1000 laser shots.

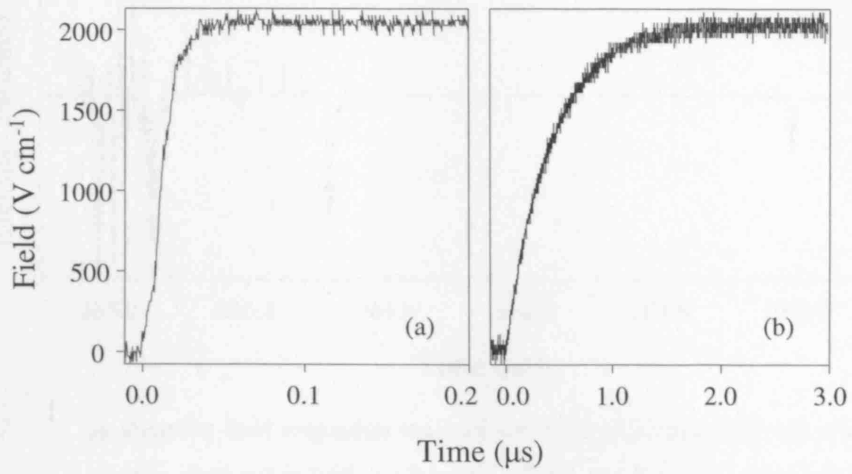

Figure 2.6 (a) A fast rising electric field pulse with an approximate rise time of 20 ns. (b) An electric field pulse with a rise time of 870 ns. The rise time was increased from 20 ns to 870 ns by attaching a series of resistors (6.56 kΩ) to a BNC cable connecting the HV supply to the field plates in the interaction region.

Figure 2.7 shows a typical trace of a SFI signal as a function of the oscilloscope timebase. Three electron signals are observed, as well as noise (265 μs) due to electrical interference. A feature common to all our SFI scans is the presence of these three similar, but separate signals, which arrive at the MCP at different times and have different intensities. These 3 peaks are an experimental artefact; however we exploit the fact that the third peak lies outside the region of electrical noise (insufficient shielded cables within the vacuum chamber). For this reason the analysis of the results in the following sections concentrates on this third peak, with the knowledge that this analysis will reflect the properties of each of these signals. Subsequently work in our group has resulted in reducing the noise and ringing considerably and is now possible to analyse the data obtained in the first, most intense peak.

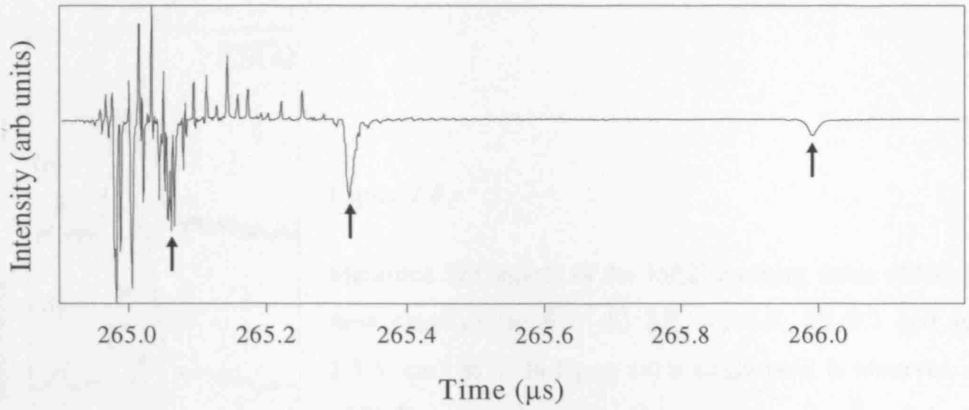

Figure 2.7 A selective field ionisation trace of the 35*f*(2) Rydberg state recorded using a electric field pulse with a slew rate of 3.7 V cm^{-1} ns^{-1}. Observed are three distinct peaks (indicated by arrows) at 265.06 μs, 265.32 μs and 265.99 μs. The presence of the three peaks is a due to the close proximity of the electron MCP to the interaction region which resulted in these echoed signals. The structure on the far left of the figure is a result of electrical noise. The first two peaks observed are perturbed due to the electrical noise and therefore the results analysed in chapter 5 concentrate on the furthest peak at 265.99 μs.

The relative start time of the field pulse with respect to the SFI trace was obtained using an iterative method. The starting point for fitting the field pulse to the SFI data was to use the SFI trace obtained from using an electric field pulse with a very fast rise time (<20 ns). The single peak obtained in these traces for the different Rydberg states is a result of a pure diabatic route to ionisation. This single diabatic peak is shown for the 35*f*(2) state in figure 2.8(a). Also shown in figure 2.8 are the 35*f*(2) ionisation profiles obtained using electric field pulses with slew rate decreasing from 6.9 V cm^{-1} ns^{-1} (a) to 1.3 V cm^{-1} ns^{-1} (e). Aligning the ionisation profiles obtained using these slew rates, clearly show the single diabatic peak at ~370 V in figure 2.8(a) evolve into a more structured profile. For each of these slew rates the different ionisation profiles for the different Rydberg states were then shifted the same amount.

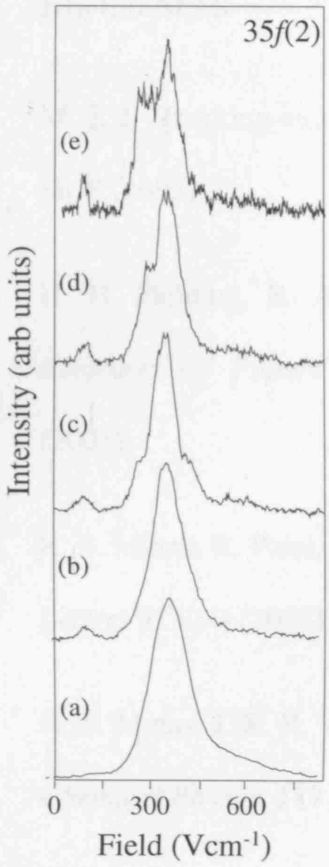

Figure 2.8

Measured SFI signals of the 35*f*(2) Rydberg states of NO at slew rates of (a) 6.9, (b) 3.7, (c) 2.8, (d) 2.3 and (e) 1.3 V cm^{-1} ns^{-1}. In figure (a) a single peak is observed at ~370 V cm^{-1}, which is consistent with a complete diabatic route to ionisation of the 35*f*(2) state. As the slew rate of the applied electric field pulse is reduced, this single peak evolves into a more structured profile, suggesting a change in route to ionisation.

2.3 SUMMARY

This chapter has described the experimental set–up used to investigate the Rydberg states of NO in the frequency domain. The simplicity and efficiency of field ionisation makes it an appealing method to detect Rydberg states, which is reflected by the fact that two different methods of field ionisation were used in the experiments described. For the investigations into the Stark states of NO, an electric field pulse with a fast rise time is used. An alternative method using electric field pulses with slow rise times was used to achieve selective field ionisation in NO.

2.4 REFERENCES

1. M. J. J. Vrakking and Y. T. Lee, *Journal Of Chemical Physics* **102** (22), 8818 (1995).

2. H. H. Fielding, R. A. L. Smith, V. G. Stavros, and J. R. R. Verlet, *Abstracts Of Papers Of The American Chemical Society* 221, U251 (2001).

3. R. S. Minns, R. Patel, J. R. R. Verlet, and H. H. Fielding, *Physical Review Letters* **91** (24) (2003).

4. R. S. Minns, J. R. R. Verlet, L. J. Watkins, and H. H. Fielding, *Journal Of Chemical Physics* **119** (12), 5842 (2003).

5. J. A. Ramswell, V. G. Stavros, J. Lei, Q. Hong, and H. H. Fielding, *Physical Review A* **59** (3), 2186 (1999).

6. J. R. R. Verlet, V. G. Stavros, R. S. Minns, and H. H. Fielding, *Physical Review Letters* **89** (26), 263004 (2002).

7. J. R. R. Verlet, V. G. Stavros, R. S. Minns, and H. H. Fielding, *Journal Of Physics B-Atomic Molecular And Optical Physics* **36** (17), 3683 (2003).

8. T. H. Jeys, G. W. Foltz, K. A. Smith, E. J. Beiting, F. G. Kellert, F. B. Dunning, and R. F. Stebbings, *Physical Review Letters* **44** (6), 390 (1980).

9. T. F. Gallagher, L. M. Humphrey, R. M. Hill, and S. A. Edelstein, *Physical Review Letters* **37** (22), 1465 (1976).

10. J. L. Vialle and H. T. Duong, *Journal Of Physics B-Atomic Molecular And Optical Physics* **12** (8), 1407 (1979).

11. A. Gurtler and W. J. van der Zande, *Physics Letters A* **324** (4), 315 (2004).

12. F. Robicheaux, C. Wesdorp, and L. D. Noordam, *Physical Review A* **62** (4), 043404 (2000).

13. T. C. Weinacht, J. Ahn, and P. H. Bucksbaum, *Physical Review Letters* **80** (25), 5508 (1998).

14. J. Ahn, D. N. Hutchinson, C. Rangan, and P. H. Bucksbaum, *Physical Review Letters* **86** (7), 1179 (2001).

15. S. N. Pisharody and R. R. Jones, *Physical Review A* **65** (3) (2002).

16. R. E. Carley, E. D. Boleat, R. S. Minns, R. Patel, and H. H. Fielding, *Journal Of Physics B-Atomic Molecular And Optical Physics* **38** (12), 1907 (2005).

17. T. F. Gallagher, *Rydberg Atoms*. Cambridge University Press, 1994.

CHAPTER 3

SPECTROSCOPY OF THE RYDBERG STATES OF NO

ABSTRACT

This chapter describes in detail the multiphoton excitation scheme used to access the Rydberg states of NO for all the experiments presented in this thesis. Described in this chapter are the ground $X\,^2\Pi_{3/2}$, intermediate $A^2\Sigma^+$ and high n Rydberg states of NO which are accessed in the experiments presented in chapter 4 and 5. Excitation to these Rydberg states results in complicated electronic spectra which is a result of simultaneous vibrational and rotational excitation. In order to interpret these spectra, a description of how the various angular momenta in NO are coupled is presented. The energies of the ground and Rydberg states excited are determined, the selection rules are derived for these transitions, as are the energies of the observed transitions.

3.1 INTRODUCTION - NO SPECTROSCOPY

The investigation of highly excited Rydberg states has been a popular subject for many years. Their unique properties [1], especially their large radial distribution, has allowed for a variety of investigations and experiments to be performed. The comprehensive review by Softley, references within [2], provided a number of examples of these applications.. As a consequence of the large orbital radius of highly excited Rydberg states, at the outer turning point of its orbit, the electron does not feel the effect of the core and can therefore be approximated to an electron in a hydrogen atom. The ability to compare Rydberg states of any system to a hydrogen atom model has allowed very accurate theoretical models to be developed, which strengthens the experimental investigations involving these Rydberg states.

The work in this thesis focuses on the Rydberg states of the nitric oxide molecule, NO. One compelling reason for investigating molecular Rydberg systems is that they offer a benchmark system for the study of the complex spectra more commonly associated with larger, polyatomic molecules. Large molecules have a high density of rovibronic states, and additional complications arising from the fact that the fundamental periods associated with electronic and rotational motion become comparable at high n, leading to strongly coupled states and thus complex and highly irregular Rydberg spectra.

NO is an ideal model Rydberg molecule: it is a free radical, such that on excitation of the outer electron in the π^*_{2pz} orbital (figure 3.1), the core is left in a

closed shell configuration. A closed shell has zero core angular momentum, which results in no net spin or angular momentum in the core.

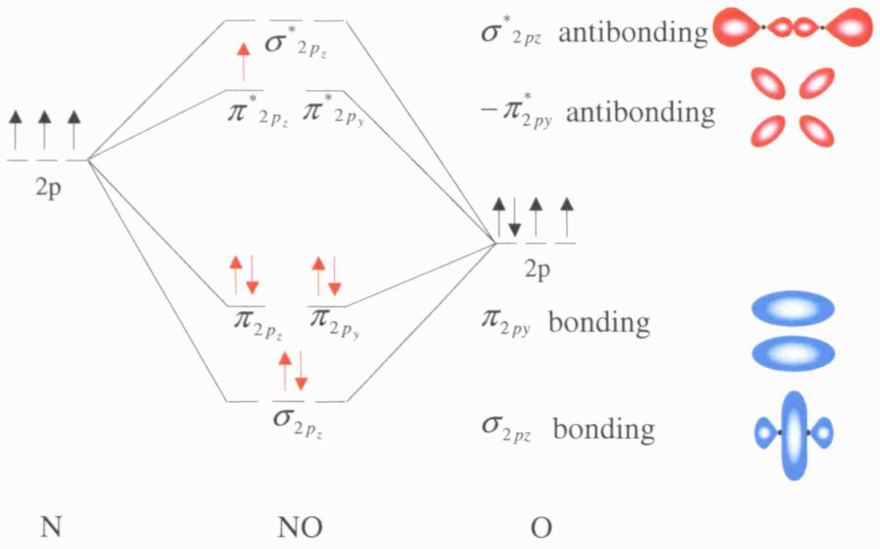

Figure 3.1 A Molecular orbital diagram for NO illustrating the 2p atomic orbitals which combine to the give the molecular orbitals (centre). Shown from the 15 electrons in NO are the electronic configuration in the 2p orbital, with the unpaired electron in the $-\pi^*_{2py}$ antibonding orbital. Excitation of this electron leads to a closed shell core, resulting in simplified coupling within the molecule and thus giving simple electronic spectra. The figures on the far right are $\sigma_{2pz}, \pi_{2py}, -\pi^*_{2py}$ and σ^*_{2pz} molecular orbitals as a result of combing the from 2p atomic orbital of N and O atoms.

The spectroscopy of the bound, autoionising and predissociating Rydberg states of NO has been investigated in detail by numerous groups [3-11]. Initial absorption spectroscopy studies of NO reported by Miescher *et al.* [12-16] resulted in a detailed analysis of the spectroscopy and behaviour of Rydberg series in NO converging to a range of vibrational levels. In this thesis only the Rydberg states

converging to the lowest vibrational state of the molecular ion are investigated and therefore these Rydberg states are electronically bound with respect to autoionisation. It is however, possible for the states to decay *via* predissociation. The $A^2\Sigma^+$, $B^2\Pi$, and $I^2\Sigma^+$ dissociative valence states of NO cross the ground state of the molecular ion around $v^+ = 0$, and molecules excited to this region can therefore dissociate leading to N + O. The evidence for this dissociation came from the observation of line broadening of the *np* states in the absorption studies of Miescher [17]. This work lead to a thorough investigation by Fujii [18-22] who compared the yield spectra of the NO^+ ion with that of the N^+ ion. The N^+ ion was created from ionisation of N atom after predissociation. They demonstrated that for the excited Rydberg states of NO, the decay dynamics were not only attributed to autoionisation but also to predissociation. The most significant discovery from these investigations was the relative decay rates of the different *l* states, and it was found that the decay dynamics of the *ns* states were dominated by autoionisation compared to the *np* states which showed strong dissociation [23,24]. The *nf* states had a lower probability of predissociation due to the smaller core penetration compared to the *np* states, and the smaller core penetration also has the effect of increasing the autoionisation lifetime. The decay processes of the *nf* states have therefore shown to compete with one another with a dependence shown on the *n* character of the state [18-20]. The dissociation of the Rydberg states was also found to be dependent on its rotational level [19] and the value of *n*: as *n* increases the Rydberg electron encounters the core less frequently leading to longer lifetimes. The competition between the two processes has been investigated by Minns *et al.* [25]. In that work the dynamics

of predissociating Rydberg wave packets was observed using the optical Ramsey method. Here, the products of the competing processes of autoionisation and predissociation were monitored by collecting either the NO^+ ions generated from autoionisation, or the N^+ ions generated from ionisation of N atoms created from predissociation. Hydrogen-atom-like dynamics were observed for the dissociating electron Rydberg wave packet, due to the presence of only one *p* Rydberg series. In contrast the autoionising wave packet dynamics in NO were more complex due to interference effects between different Rydberg series. Essentially the interplay between electronic and molecular phases was manipulated to control the ratio of autoionisation to predissociation of Rydberg wave packets in NO.

3.2 EXCITATION SCHEME

The potentially complex and dense number of Rydberg states accessible in NO can be controlled to some extent by employing a multiphoton excitation scheme. In principle, it is possible to access the Rydberg states of NO using a single photon of vacuum ultraviolet radiation but control over the resulting states would be limited. Since a number of rotational states are significantly populated in the ground state, a huge variety of Rydberg series converging to different rotational states of the ion core would be excited. Instead, in the work presented in this thesis, we employ a two step excitation process. We first excite to a well-defined rotational level of the $A^2\Sigma^+$ state which allows some selectivity over the Rydberg states to be excited. This state is the lowest Rydberg state in NO and was chosen as a suitable intermediate due to its well-characterised spectroscopy and because

the Franck-Condon factors to high Rydberg states shows a strong $\Delta v = 0$ propensity. Both the *A*-state and the Rydberg states converge to the same electronic state of the ion and therefore have very similar potential surfaces which results in this propensity.

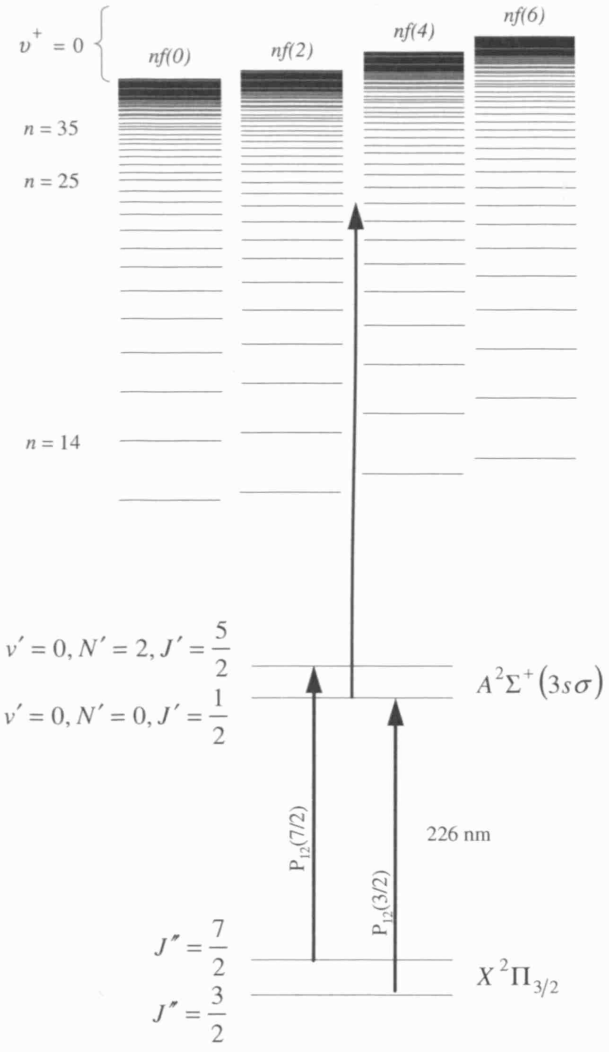

Figure 3.2 A two photon excitation scheme accessing the bound Rydberg states of NO. The Rydberg states are excited *via* either the $v' = 0, N' = 0$ or $v' = 0, N' = 2$ ro-vibrational state of the $A^2\Sigma^+$ state of NO

3.2.1 THE HUNDS COUPLING CASES

The complexity of the Rydberg spectrum, which arises from the simultaneous excitation of vibrational and rotational transitions within the electronic transition, can be interpreted by understanding the various angular momentum coupling processes that occur within the molecule. Hund's coupling cases formalise the limiting cases (most molecules lie somewhere in between), by providing a model explaining how these various angular momenta are coupled within the molecule. Hund's model dictates the selection rules that govern the transitions to and from the A-state, and by understanding the coupling we are able to assign the spectrum obtained.

In brief, Hunds coupling cases look at the coupling of angular momenta in four limiting cases, three of which are described here. The angular momenta considered in a molecule are:

- Total electronic spin angular momentum, S
- Total electronic orbital angular momentum, L
- Rotation of the nuclei, R

As well as these angular momenta, a Rydberg electron also possesses its own angular momentum

- Spin angular momentum of a Rydberg electron, s
- Orbital angular momentum of a Rydberg electron, l

For the Rydberg states of NO, $l \equiv L$ and $s \equiv S$.

Hunds case (a)

In this case, the spin-orbit coupling is very strong as well as the coupling between the orbital angular momentum and the internuclear axis. Hence both L and S are well defined along the internuclear axis and the projections are given quantum numbers Λ and Σ respectively. The total electronic angular momentum given by the sum of these quantum numbers

$$\Lambda + \Sigma = \Omega . \tag{3.1}$$

The total electronic angular momentum then couples with R, to give the total angular momentum, J

$$\Omega + R = J \tag{3.2}$$

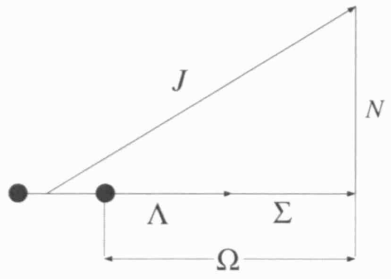

Figure 3.3 Vector diagram representing the Hund's coupling case (a)

Hunds case (b)

In this case, the spin-orbit coupling is weak when $\Omega \neq 0$ and absent when $\Lambda = 0$. As before the orbital angular momentum, L strongly couples with the internuclear

axis with quantum number Λ. This then combines with R to give N, which in turn couples with S to give the total angular momentum, J.

$$\Lambda + R = N \tag{3.3}$$

$$N + S = J \tag{3.4}$$

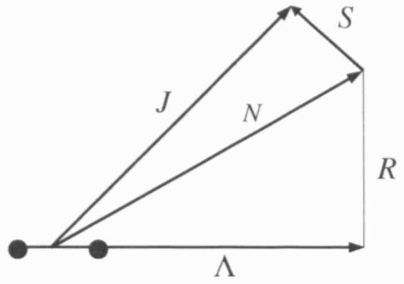

Figure 3.4 Vector diagram representing the Hund's coupling case (b)

Hunds case (d)

This case arises when coupling between the electron and molecular axis is weak, which occurs when the excited electron is far from the remaining core electrons. The rotation of the ion core is labelled as N^+. The Rydberg orbital angular momentum, l couples with the rotational angular momentum of the core, N^+ to give N. N then couples with the spin angular momentum of the Rydberg electron, s to give the total angular momentum, J.

$$J = N^+ + l + s = N + s \tag{3.5}$$

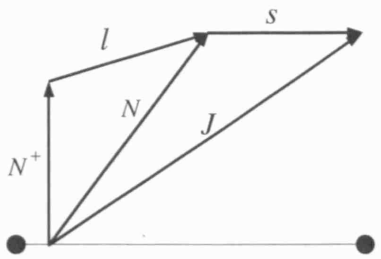

Figure 3.5 Vector diagram representing the Hund's coupling case (d).

3.2.2 THE GROUND STATE OF NO

The angular momentum coupling in the ground state of NO is intermediate between Hund's case (a) and (b). In this intermediate coupling scheme, each rotational state is split into two spin-orbit components, with $\Omega = 1/2$ and $\Omega = 3/2$. These states are labelled $^2\Pi_{1/2}$ and $^2\Pi_{3/2}$. The lower rotational levels are described well using Hund's case (a) coupling, whereas higher rotational levels tend to Hund's case (b). As the two spin-orbit states are only separated by 124.89 cm^{-1} [17], rotational levels of both the $^2\Pi_{1/2}$ and $^2\Pi_{3/2}$ states are populated in our molecular beam. In this work we use transitions from the $^2\Pi_{3/2}$ ground state. The energy of the ground state rotational levels, $^2\Pi_{3/2}$ can be calculated from the following equation

$$E\left(^2\Pi_{3/2}\right) = G_v'' - D_v'' + \alpha_v''/2 + B_{v2}''\left(J'' + \frac{1}{2}\right)^2 - D_{v2}''\left(J'' + \frac{1}{2}\right)^4, \tag{3.6}$$

where

$$G_v'' = \omega_e''\left(v'' + \frac{1}{2}\right) - \omega_e x_e''\left(v'' + \frac{1}{2}\right)^2 + \omega_e y_e''\left(v'' + \frac{1}{2}\right)^3 \ldots \tag{3.7}$$

is the vibrational energy. ω_e'' is the harmonic vibrational frequency and $\omega_e x_e''$, $\omega_e y_e''$ are the 1st and 2nd order anharmonicity constant respectively. v'' represents the vibrational quantum number. D_v'' is the true rotational constant and D_{vi}'' and B_{vi}'' are the effective rotational constants where i is either 1 or 2 which refers to the $^2\Pi_{1/2}$ or $^2\Pi_{3/2}$ states respectively. $\alpha''/2$ refers to the zero point energy, given half way between the two states where α'' is the electronic splitting between $^2\Pi_{1/2}$ and $^2\Pi_{3/2}$ states. Table 3.1 lists the values of the constants used to calculate ground state energy levels.

	$X\,^2\Pi_{3/2}$
ω_e''	1903.68
$\omega_e x_e''$	13.97
$\omega_e y_e''$	0.0077
α''	119.770
D_0''	5.5×10^{-6}
D_{02}''	9.8×10^{-6}
B_{02}''	1.72002

Table 3.1 Spectroscopic constants used in equations *3.6 and 3.7* to calculate the energy of the $X\,^2\Pi_{3/2}$ ground state of NO. All values are given in cm^{-1} and are taken from [26,27]

3.2.3 THE *A*-STATE OF NO

The $A^2\Sigma^+$ state is the lowest Rydberg state of NO and is predominantly a $3s\sigma$ Rydberg state. The most appropriate angular momentum coupling scheme to

describe this state is Hund's case (b), and the energy of the intermediate rovibrational states may be calculated using the Dunham series [28]

$$E_{v,N} = T_e' + G_v' + F_v' \tag{3.8}$$

$$F_v' = B_v N'(N'+1) - D_v N'(N'+1)^2 \tag{3.9}$$

Were

$$G_v' = \omega_e'\left(v'+\frac{1}{2}\right) - \omega_e\chi_e'\left(v'+\frac{1}{2}\right)^2 + \omega_e Y_e'\left(v'+\frac{1}{2}\right)^3 \ldots \tag{3.10}$$

$$B_v' = B_e' - \alpha_e'\left(v'+\frac{1}{2}\right) - \gamma_e'\left(v'+\frac{1}{2}\right)^2 \ldots \tag{3.11}$$

$$D_v' = D_e' + \beta_e'\left(v'+\frac{1}{2}\right) \ldots \tag{3.12}$$

and v' and N' are the vibrational and rotational quantum numbers respectively and T_e' is the energy from the bottom of the A-state potential well to the bottom of the ground state potential well. Each rotational level N' is split by spin-rotation coupling into two levels, $J' = N' + 1/2$ and $J' = N' - 1/2$, with even and odd parity respectively. The coupling between these two is weak so is negligible in equation 3.9. The molecular constants used to calculate the energy of the A-state are listed in table 3.2. For the work presented in this thesis the two intermediate levels accessed have even parity and are, $v' = 0, N' = 0, J' = 1/2$ and

$v' = 0, N' = 2, J' = 5/2$.

	$A^2\Sigma^+$
T_e'	43965.7
ω_e'	2374.31
$\omega_e x_e'$	16.1601
$\omega_e y_e'$	−0.0465
α_e'	0.019195
B_e'	1.9965
D_e'	4.9×10^{-6}
γ_e'	negligible
β_e'	negligible

Table 3.2 Spectroscopic constants used in equations *3.8 to 3.12* to calculate the energy of the $A^2\Sigma^+$ Rydberg state of NO. All values are given in cm^{-1} and are taken from [26,27,29]

3.2.4 THE RYDBERG STATES OF NO

As the Rydberg electron spends most of its time away from the core region it is regarded as separate from the core, and so the most appropriate coupling scheme is Hund's case (d). The core is described by the vibrational, v^+ and rotational, N^+ quantum numbers while the quantum numbers for the Rydberg electron are the principal quantum number, n, the electron orbital angular momentum, l and the spin s. The higher Rydberg states accessed in this work are described most appropriately using Hund's case (d) coupling and are labelled using the following nomenclature: N^+, l, s, J, p^+. The energy of the Rydberg states are calculated to the 1st order (excluding interseries coupling) using

$$E = IP_{v^+N^+} - \frac{R}{(n-\delta_l)^2} \tag{3.13}$$

Where R is the Rydberg constant and δ_l is the l dependent quantum defect. IP_{v^+,N^+} is the ionisation potential that a Rydberg series converges to, where the series is characterised by the same N^+, v^+ and l, differing only by n. The IP value for a particular Rydberg series (equation 3.14) is determined by the total energy of excitation from the $X^2\Pi_{3/2}$ level, which is defined by the zero point energy of the system. In this case the zero point energy is defined as the ionisation potential for excitation from the $X^2\Pi_{1/2}$ level to the Rydberg series converging to $X^1\Sigma^+(v^+ = 0, N^+ = 0)$ in NO, 74721.51 cm^{-1} [29].

$$IP_{v^+N^+} = 74721.51 + G_{v^+} + F_{v^+(J)} - G_{v^+=0} \tag{3.14}$$

The terms F_{v^+} and G_{v^+} are defined as in equations 3.9 and 3.10 and the spectroscopic constants used to calculate these are listed in table 3.3. The final calculation of the excitation from the $X^2\Pi_{3/2}$ level to a Rydberg series must incorporate the energy gap of 124.89 cm^{-1} [17] between the $X^2\Pi_{1/2}$ and $X^2\Pi_{3/2}$ levels.

ω_e^+	2376.42
$\omega_e x_e^+$	16.626
$\omega_e y_e^+$	negligible
α_e^+	0.01889
B_e^+	1.99727
D_e^+	5.6×10^{-6}
γ_e^+	negligible
β_e^+	negligible

Table 3.3 Spectroscopic constants used in equations 3.14 to calculate the IP_{v^+,N^+} value for a particular Rydberg series from the $X\,^2\Pi_{3/2}$ level of NO. All values are given in cm^{-1} and are taken from [26,27,29]

3.2.5 TRANSITION FROM GROUND TO *A*-STATE

Possible transitions from the ground state to the *A*-state are governed by the following selection rules

$$\Delta\Lambda = \pm 1 \tag{3.15}$$

$$\Delta J = 0,\pm 1 \tag{3.16}$$

The latter rule gives rise to different branches in the spectrum.

When $\Delta J = -1$ P branch

$\Delta J = 0$ Q branch

$\Delta J = 1$ R branch

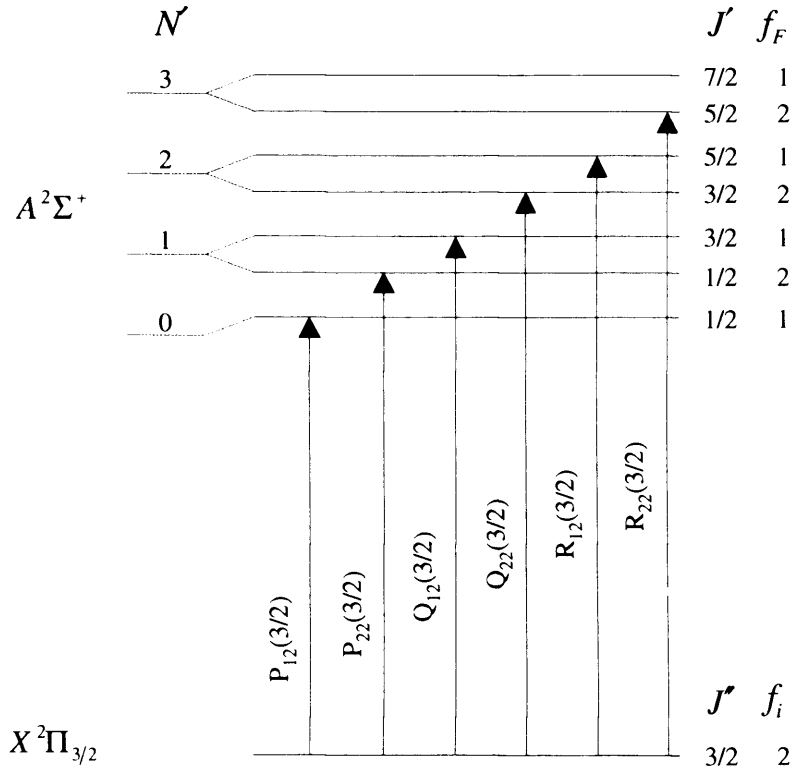

Figure 3.6 A schematic diagram showing the six possible branches (arrows) from the $X^2\Pi_{1/2}(J''=3/2)$ state to the $A^2\Sigma^+(3s\sigma)$ intermediate state in NO. For experiments presented in this thesis the intermediate states are accessed *via* the P_{12} branch.

In total there are six possible branches accessible from the $X^2\Pi_{3/2}$ state to the $A^2\Sigma^+$ state, and these are labelled as P_{12}, P_{22}, Q_{12}, Q_{22}, R_{12} and R_{22} (figure 3.6). The subscripts 1 and 2 for all the branches indicate the rotational term for the final $(A^2\Sigma^+)$ and initial $(X^2\Pi_{3/2})$ states of the transition. In figures 3.6 and 3.7 these initial and final rotational terms are labelled as f_i and f_F respectively.

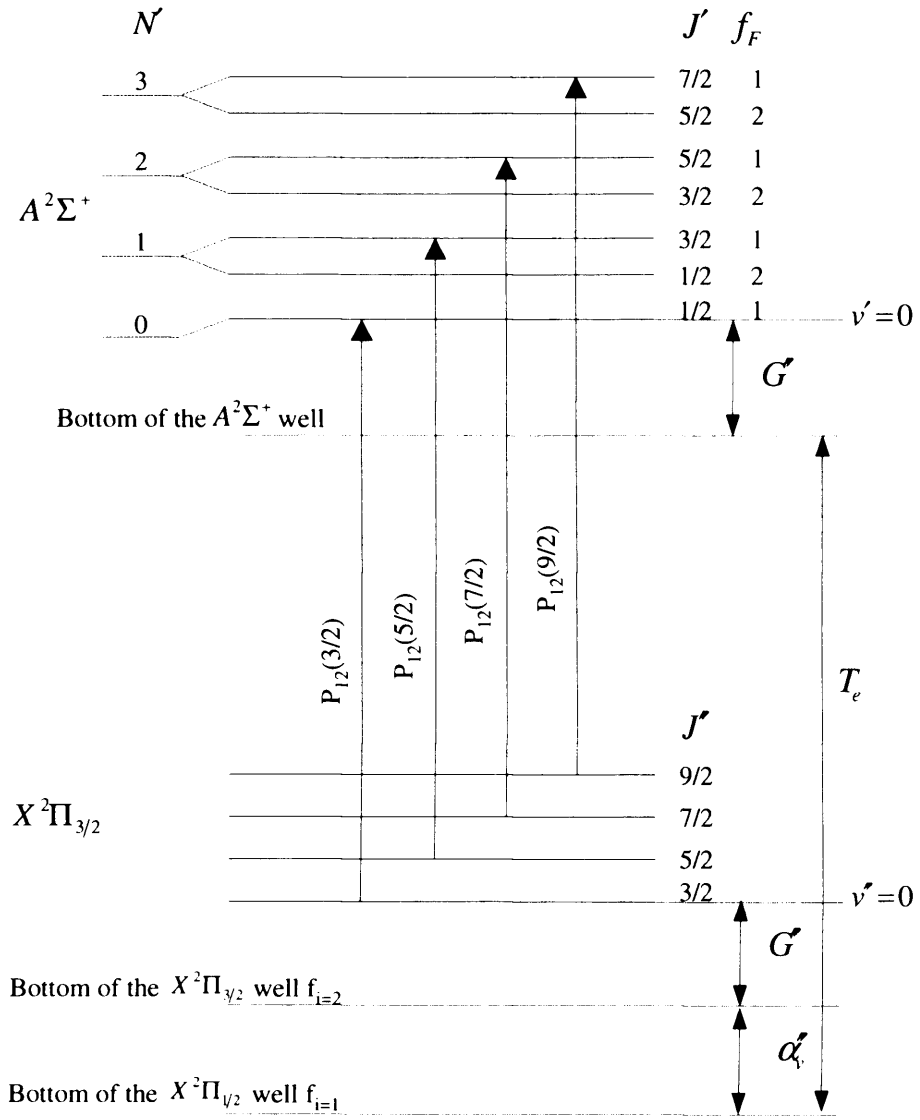

Figure 3.7 A schematic diagram showing the transition from the $X^2\Pi_{1/2}$ ground state to the $A^2\Sigma^+(3s\sigma)$ intermediate state in NO. Highlighted are some of the spectroscopic constants used to calculate the energy levels of the two electronic states. The arrows indicate the first four transitions of the P_{12} branch. For experiments presented in this thesis the intermediate states are accessed *via* the P_{12} branch.

For the work presented in this thesis the intermediate state is accessed from the $^2\Pi_{3/2}$ ground state *via* the P_{12} branch of the $A^2\Sigma^+ \leftarrow X^2\Pi_{3/2}$ transition. The P_{12}

branch was chosen because there were no other branches obstructing these lines, allowing easy selection of any given rovibrational level.

A spectrum of the $A^2\Sigma^+ \leftarrow X^2\Pi_{3/2}$ transition is obtained by recording a $1+1$ resonance enhanced multiphoton ionisation (REMPI) spectrum. The laser light is scanned through the rotational structures of the $v' = 0$ vibrational state of the intermediate state. When the frequency of the light is in resonance with an allowed transition, another photon in the laser field ionises the electron to produce photoelectrons and NO^+ ions. A small portion of the spectrum is presented below in figure 3.8.

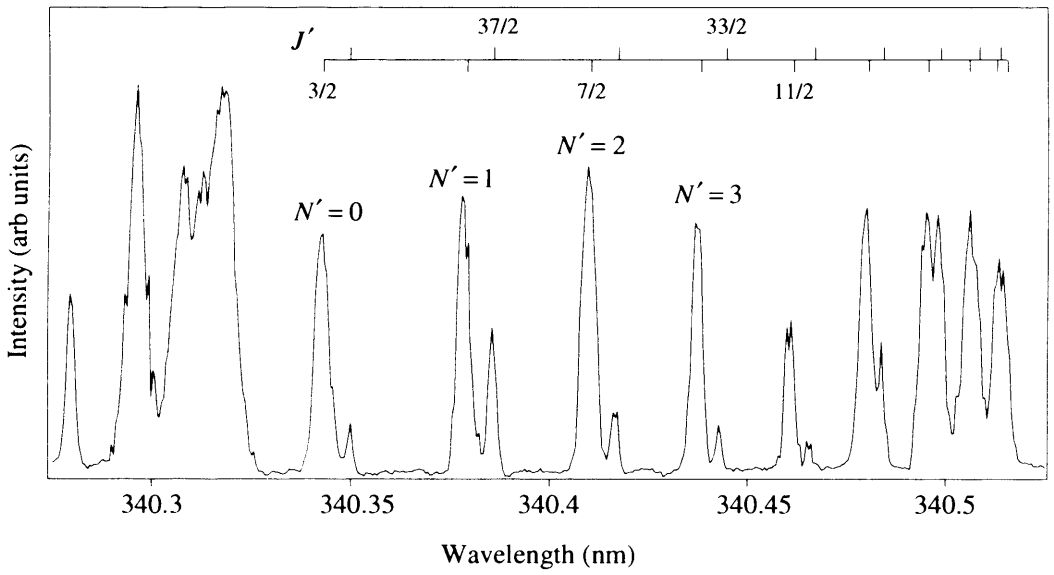

Figure 3.8 Frequency spectrum of the P_{12} branch in NO of the $A \leftarrow X$ transition showing relatively undulated spectrum enabling one to select single states. We excite *via* this branch since it does not have any other branches running through it, hence enabling one to select a well resolved rotational state. Highlighted are the $N' = 0$, $N' = 1$, $N' = 2$ and $N' = 3$ rotational levels of the A-state from which the Rydberg states are accessed for experiments presented in this thesis. Also observed is the P_{12} bandhead at about 340.5 nm and the bandhead for the neighbouring R_{12} bandhead at 340.3 nm.

The states are labelled with their J' values with a comb. The Rydberg states excited for experiments presented in this thesis are accessed *via* the $N'=0$, $N'=1$, $N'=2$ or $N'=3$ rotational levels of the *A*-state. These rotational levels are indicated in figure 3.8. Also observed in this spectrum are the band heads of the P_{12} branch at 340.5 nm and the neighbouring R_{12} branch at 340.3 nm. The P_{12} branch was selected for the experiments presented in this thesis as it is the least congested branch and thus experimentally viable [30].

3.2.6 TRANSITION FROM *A*-STATE TO RYDBERG STATES

The relatively large distance between the Rydberg electron and the remaining core electrons leads to a weak coupling between the electron and the molecular axis. Hence the Rydberg electron orbital angular momentum, *l*, the core rotational angular momentum, N^+, and the spin angular momentum of the Rydberg electron, *s*, all couple to give the total angular momentum, $J = s + l + N^+$. Conservation of the total angular momentum dictates

$$\mathbf{J}' + \boldsymbol{\gamma} = \mathbf{J} = \mathbf{N}^+ + \mathbf{l} + \mathbf{s} \tag{3.17}$$

Where γ is the angular momentum of one photon, and the total angular momentum of the intermediate state $J' = N' + s'$. The electron spin remains the same during a transition from the *A*-state to a Rydberg state, which leads to

$$\mathbf{N}' + \boldsymbol{\gamma} = \mathbf{N}^+ + \mathbf{l} \tag{3.18}$$

and there is a requirement for a change in overall parity

$$p_{Ryd}\, p' = -1 \tag{3.19}$$

where the parity of a Rydberg state is given by $p_{Ryd} = (-1)^{N^+ + l}$.

The Rydberg series accessed from the *A*-state are labelled using the notation $nl(N^+)$, where n is the principal quantum number, l is the orbital angular momentum quantum number and N^+ is the rotational quantum number of the molecular ion core. Taking into account the angular momentum composition of the *A*-state, which is 94% *s* and 5% *d*, and the selection and propensity rules, we expect to access *np*(0), *np*(2), *nf*(2), *nf*(4) Rydberg series from the $v' = 0, N' = 0, J' = 1/2$ intermediate, and *np*(0), *np*(2), *np*(4), *nf*(0), *nf*(2), *nf*(4), *nf*(6) Rydberg series from the $v' = 0, N' = 2, J' = 5/2$ intermediate. Weak transitions from the 1% *p* component of the *A*-state to *ns* and *nd* series are also possible and have been observed [10,31,32]. Also only the $v^+ = 0$ vibrational state is populated due to good Frank Condon overlap between the *A*-state and the high Rydberg states. Figure 3.9 is an example of a Rydberg spectrum of NO excited *via* the $v' = 0, N' = 0, J' = 1/2$ intermediate level. Clearly the dominant Rydberg series observed is the *nf*(2) Rydberg series and is distinguishable up to around n = 50. In accordance to selections rules described in chapter two, one would also expect to access the *np*(0) Rydberg series from this intermediate level. However due to the relatively short lifetime of the *p* states there is little evidence of the *np*(0) Rydberg series. This is discussed further in chapter 4.

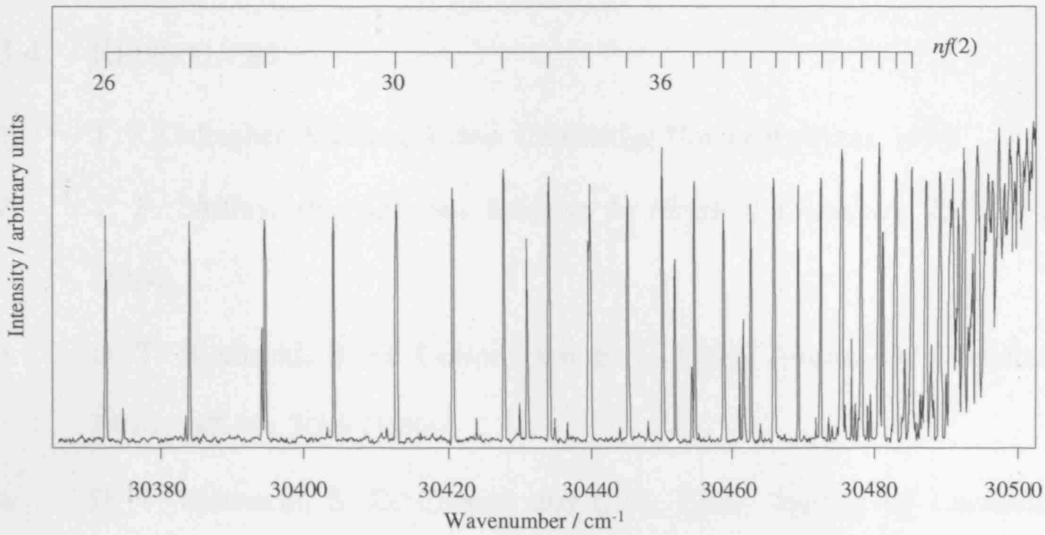

Figure 3.9 Zero field $(1+1')$ pulsed-field ionisation spectrum of the Rydberg states of NO converging on $v^+ = 0$ ionisation limit *via* the $N' = 0$ rotational level of the $A^2\Sigma^+(3s\sigma)$ state. The *nf*(2) Rydberg series is the dominant series observed which is consistent with the selection rules given in the text. The *nf*(2) Rydberg series is indicated by a comb which is calculated using $E = -R/(n-\delta_l)^2$, where R is the Rydberg constant, 109735.3 cm^{-1} for NO, n is the principal quantum number and δ_l is the quantum defect. The quantum defect is dependent on the angular momentum of the series and the value used to calculate the *nf* series is 0.01 [33].

3.3 SUMMARY

This chapter has described the calculations required for assignment of Rydberg frequency spectra in NO for Rydberg states which have been accessed from the $X^2\Pi_{3/2}$ ground state of NO *via* the $A^2\Sigma^+$ state. The energies of these states and the transition energies between these states have been calculated. The selection rules for these transitions were also derived with consideration of angular momentum coupling within the molecule.

3.4 REFERENCES

1. T. F. Gallagher, *Rydberg Atoms*. Cambridge University Press, 1994.
2. T. P. Softley, *International Reviews In Physical Chemistry* **23** (1), 1 (2004).
3. D. T. Biernacki, S. D. Colson, and E. E. Eyler, *Journal Of Chemical Physics* **88** (4), 2099 (1988).
4. D. T. Biernacki, S. D. Colson, and E. E. Eyler, *Journal Of Chemical Physics* **89** (5), 2599 (1988).
5. S. Fredin, D. Gauyacq, M. Horani, C. Jungen, G. Lefevre, and F. Masnouseeuws, *Molecular Physics* **60** (4), 825 (1987).
6. K. P. Huber, M. Huber, and E. Miescher, *Physics Letters* **3** (7), 315 (1963).
7. S. T. Pratt, C. Jungen, and E. Miescher, *Journal Of Chemical Physics* **90** (11), 5971 (1989).
8. K. P. Huber, M. Vervloet, C. Jungen, and A. L. Roche, *Molecular Physics* **61** (2), 501 (1987).
9. Y. Anezaki, T. Ebata, N. Mikami, and M. Ito, *Chemical Physics* **97** (1), 153 (1985).
10. K. Kaufmann, C. Nager, and M. Jungen, *Chemical Physics* **95** (3), 385 (1985).
11. M. Raoult, S. Guizard, and D. Gauyacq, *Journal Of Chemical Physics* **95** (12), 8853 (1991).
12. E. Miescher, *Journal Of Molecular Spectroscopy* **20** (2), 130 (1966).
13. E. Miescher, *Canadian Journal Of Physics* **49** (18), 2350 (1971).

14. E. Miescher, *Journal Of Molecular Spectroscopy* **53** (2), 302 (1974).

15. E. Miescher, *Journal Of Molecular Spectroscopy* **69** (2), 281 (1978).

16. E. Miescher, Y. T. Lee, and P. Gurtler, *Journal Of Chemical Physics* **68** (6), 2753 (1978).

17. E. Miescher, *Canadian Journal Of Physics* **54** (20), 2074 (1976).

18. A. Fujii and N. Morita, *Chemical Physics Letters* **182** (3-4), 304 (1991).

19. A. Fujii and N. Morita, *Journal Of Chemical Physics* **97** (1), 327 (1992).

20. A. Fujii and N. Morita, *Journal Of Chemical Physics* **98** (6), 4581 (1993).

21. A. Fujii and N. Morita, *Laser Chemistry* **13** (3-4), 259 (1994).

22. A. Fujii and N. Morita, *Journal Of Chemical Physics* **103** (14), 6029 (1995).

23. A. Giustisuzor and C. Jungen, *Journal Of Chemical Physics* **80** (3), 986 (1984).

24. M. Raoult, *Journal Of Chemical Physics* **87** (8), 4736 (1987).

25. R. S. Minns, R. Patel, J. R. R. Verlet, and H. H. Fielding, *Physical Review Letters* **91** (24) (2003).

26. D. B. Keck and C. D. Hause, *Journal Of Molecular Spectroscopy* **26** (2), 163 (1968).

27. G. Hertzberg, *Spectra of diatomic molecules*. Cornell university press, 1971.

28. J. B. a. A. Carrington, *Rotational Spectroscopy of Diatomics Molecules*. Cambridge University Press, 2003.

29. G. Herzberg and K. P. Huber, *Constants of Diatomic Molecules*. Van Nostrad, 1979.

30. V. G. Stavros and H. H. Fielding, *Physical Review A* **60** (6), 4774 (1999).

31. V. G. Stavros, J. A. Ramswell, R. A. L. Smith, J. R. R. Verlet, J. Lei, and H. H. Fielding, *Physical Review Letters* **83** (13), 2552 (1999).

32. S. N. Dixit, D. L. Lynch, V. McKoy, and W. M. Huo, *Physical Review A* **32** (2), 1267 (1985).

33. C. Jungen and E. Miescher, *Canadian Journal Of Physics* **47** (17), 1769 (1969).

CHAPTER 4

OBSERVATION OF THE STARK EFFECT IN $v^+ = 0$ RYDBERG STATES OF NO WITH A MATRIX DIAGONALISATION ASSIGNMENT

ABSTRACT

Rydberg states with principal quantum number n = 25 – 32, below the $v^+ = 0$ ionisation limit, are excited by double-resonance *via* the $v' = 0, N' = 0$, and $v' = 0, N' = 2$ rovibrational states of the $A^2\Sigma^+$ state. In the presence of dc electric fields in the range 0 – 120 V cm^{-1}, new resonances and hydrogenic manifolds are observed. The experimental spectra are simulated using a hybrid MQDT/matrix-diagonalisation approach.

4.1 INTRODUCTION

In molecular Rydberg systems there are Rydberg series converging to each rovibronic state of the ion. Not only is the density of states very high, but these series interact with one another leading to complex and irregular Rydberg spectra. NO is an ideal model Rydberg molecule as it has a low ionisation limit and a reasonably simple structure – the spectroscopy of the bound, autoionising and predissociating Rydberg states has been investigated in detail by numerous groups [1-6] and there have been a great number of theoretical studies of the Rydberg states [2,3,7-9]. Moreover, the first experimental observations of molecular Rydberg wave packets were carried out in NO [10-12], as were the first demonstrations of coherent control in a Rydberg molecule [13,14].

In this chapter an investigation of the Stark effect in Rydberg states of NO below the lowest ionisation threshold, in the region of the spectrum where the rotational and electronic spacings are comparable and the breakdown of the Born Oppenheimer approximation is most evident is reported. NO remains one of the few molecules whose Rydberg states have been investigated experimentally in the frequency domain in the presence of an electric field. Goodgame *et al.* [15] presented a detailed study of the Stark effect on autoionising Rydberg states of NO converging to the $v^+ = 1$ ionisation limit with a comparison of matrix diagonalisation and MQDT theoretical approaches. The Stark effect in very high (n = 40 – 120) Rydberg states converging to the $v^+ = 0$ ionisation limit has been reported by Vrakking *et al.* [16]. Warntjes *et al.* [17] also investigated Rydberg states converging to the $v^+ = 0$ ionisation limit, but above the field-ionisation

limit. This work presents Stark studies focused on intermediate (n = 25 – 32) Rydberg states converging to the $v^+ = 0$ ionisation limit well below the field ionisation threshold in dc fields in the range 0 – 120 V cm^{-1}. This work was motivated by our ongoing interest in developing intuitive optical control strategies to control molecular Rydberg wave packet dynamics, in particular a wish to control the composition of a wave packet created from Rydberg states belonging to a number of Rydberg series converging to the lowest vibrational state of the molecular ion core. The composition of the wave packet will be measured using selective field-ionisation (SFI), and in order to model the SFI process it is necessary to develop an understanding of how these Rydberg states behave and interact with one another in a dc electric field.

4.2 THEORY: SIMULATION OF RYDBERG STARK SPECTRA

4.2.1 RYDBERG STATES SELECTION RULES

The Rydberg series are accessed *via* the $v' = 0, N' = 0, J' = 1/2$ and $v' = 0, N' = 2, J' = 5/2$ levels of the A-state. They are labelled using the notation $nl(N^+)$, where n is the principal quantum number, l is the orbital angular momentum quantum number and N^+ is the rotational quantum number of the molecular ion core. The most appropriate coupling scheme for these Rydberg states is Hund's case (d). The selection rules which govern the excitation of the Rydberg states are described in detail in section 3.2.6. According to these selection and propensity rules, one would expect to access $p(0)$, $p(2)$, $f(2)$, $f(4)$

Rydberg series from the $v' = 0, N' = 0, J' = 1/2$ intermediate, and $p(0)$, $p(2)$, $p(4)$, $f(0)$, $f(2)$, $f(4)$, $f(6)$ Rydberg series from the $v' = 0, N' = 2, J' = 5/2$ intermediate. Weak transitions from the 1% p component of the A-state to s and d series are also possible and have been observed, e.g. [12]. Vibrational transitions are controlled by the fact that the overriding Franck-Condon factor is for $\Delta v = 0$ transitions due to the similarity in potential energy surfaces for the Rydberg and A-state.

In all the zero field spectra, the dominant Rydberg series observed are f in character. This may be surprising considering the launch state used; however, the np Rydberg series are known to rapidly predissociate and will have almost completely decayed on our detection timescale. So while the dominant transition is to the np Rydberg states, these are not detected in the current scheme. The predissociating Rydberg states of NO, have been studied in detail by Fujii and Morrita [18-22] and others [23,24], revealing a rotational dependence of the predissociation lifetime as well as confirming calculations that the np states predissociate more rapidly than other orbital angular momentum states [8,25].

4.2.2 MATRIX DIAGONALISATION CALCULATION

The energy of the Hydrogen atom Stark levels is sufficiently accurately calculated to 2nd order using the equation

$$E = -1/2n^2 + 3nkF/2 - (1/16)n^4\left[17n^2 - 3k^2 - 9m^2 + 19\right]F^2 \qquad (4.1)$$

Although equation 4.1 is suitable for the simulation of Stark spectra in the Hydrogen atom, more sophisticated calculations are required to simulate Stark spectra in more complex molecules. Essentially there are two main computational approaches used to calculate the effect of an electric field on the spectroscopy and dynamics of Rydberg states: MQDT and matrix diagonalisation. Matrix diagonalisation is a perturbative method which calculates the altered energy levels of Rydberg systems by diagonalising the total Hamiltonian of the perturbed system. It was first employed by Zimmerman *et al.* [26] to simulate alkali metal energy levels of Rydberg states in an electric field. Later this method was applied to more atomic systems [26-29] and developed further for use on molecular systems [30]. Specifically, the work presented in this chapter is based on a hybrid method developed by Vrakking [16].

The second computational method, MQDT was the first method applied to investigate the Stark effect of molecules by Sakimoto [31]. It is based on the idea that a Rydberg electron with low angular momentum, l, spends the majority of its time in two distinct regions of the orbit: the core and outer turning point. More importantly, the behaviour of the electron in these two regions differs. In the core region the electron travels with high velocity. This electron is characterised as Hunds case (b) (l coupled to molecular internuclear axis) and its motion satisfies the Born Oppenheimer approximation. Away from the core, the velocity of the Rydberg electron is considerably slower and its dynamics follow the inverse Born Oppenheimer approximation. Here, the electron is independent of the ion core and therefore the electronic orbital angular momentum is no longer coupled to the internuclear axis. This electron is thus characterised by Hunds case (d) coupling.

The MQDT computation connects the two regions by applying a frame transformation.

A comparison between the two approaches used to calculate the Stark state energies of NO was presented by Goodgame *et al.* [15]. In my mind, their results showed that the matrix diagonalisation simulations provided a slightly better fit to the experimental spectra. In addition, it is relatively straightforward to apply the matrix diagonalisation calculations to NO and therefore it is the more appealing technique. In comparison to MQDT, using matrix diagonalisation usually only requires one diagonalisation calculation at a given field to give a complete set of results. In this approach the Hamiltonian Matrix must ideally contain all states of the system, but due to computational limitations this is not possible and the size of the basis set is reduced. However this is achievable without loss of accuracy due to, firstly, the relevance of the off diagonal matrix elements (perturbations) decreasing as the energy gap between adjacent states increases. Since in this work only the high Rydberg states are excited, this is a viable approximation. Secondly adequate truncation of the matrix is attained by excluding states to which coupling is forbidden due to zero field coupling selection rules. A potential disadvantage of using the matrix diagonalisation method is the possibility that it could miss calculations involving certain critical processes, for example, the coupling between states converging to different vibrational thresholds (due to the numbers of bound-bound and bound-continuum coupling parameters). A global MQDT representation is being developed to include small interseries couplings such as $s\sigma$—$f\sigma$, $s\sigma$—$p\sigma$, $f\pi$—$p\pi$ and $f\pi$—$d\pi$ as well as the larger *s-d* interactions [32] and this is something our group will exploit in the future.

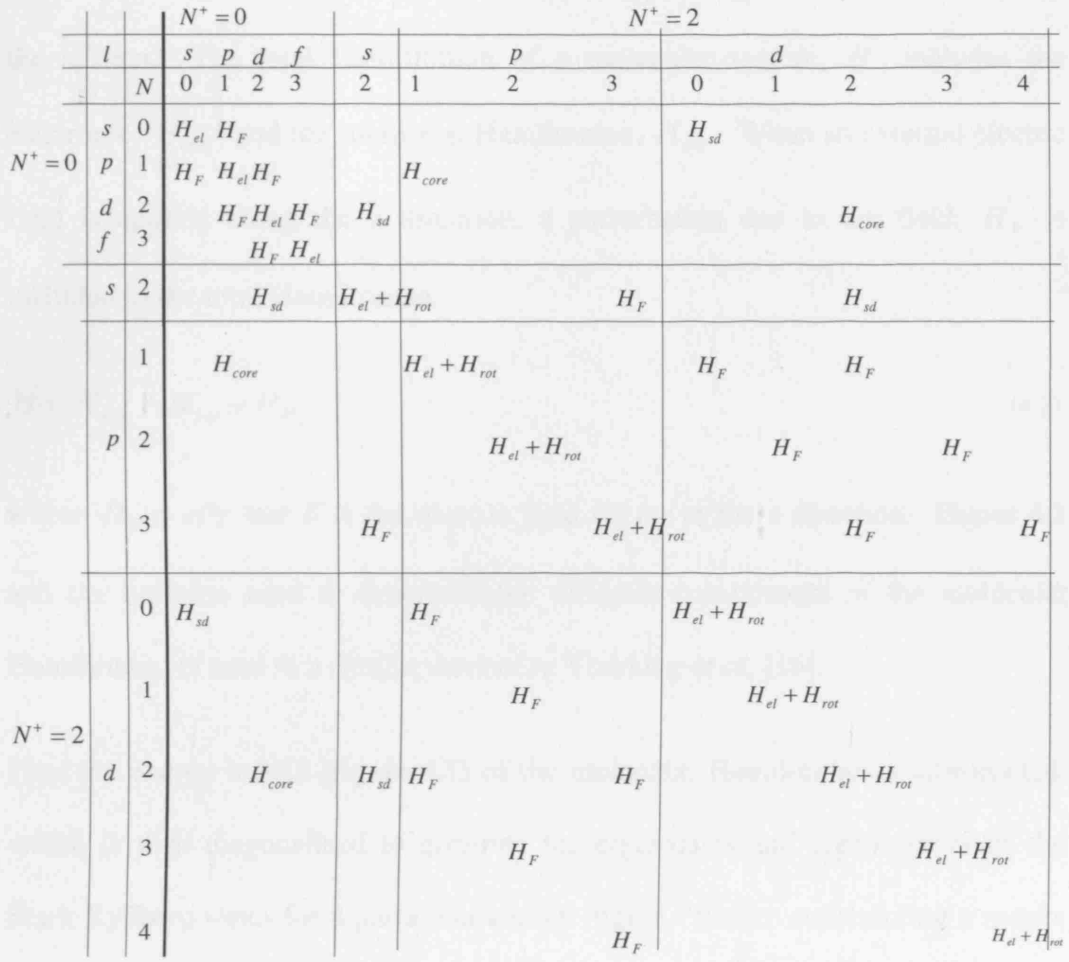

Figure 4.1 A schematic of the Hunds case (d) energy matrix of the total molecular Hamiltonian illustrating the various components included in the matrix diagonalisation calculations. The total Hamiltonian is the sum of the electronic Hamiltonian, H_{elec}, the rotational Hamiltonian, H_{rot} and the perturbed Hamiltonian due to the applied electric field, H_F. The diagonal matrix elements are given by the sum $H_{elec} + H_{rot}$, where by H_{elec} is converted to case (d) *via* a frame transformation. The off diagonal matrix elements arise due to perturbations to the molecular system, including short and long range core – electron interactions, where H_F is a result of a long range coupling. The short range interactions $(l \leq 3)$ included in the calculation are the $s\sigma / d\sigma$ coupling denoted by H_{sd} and the $l - l$ coupling, H_{core}, which is a coupling of Rydberg states with the same *l*, *N*, but with N^+ differing by two quanta. This diagram only shows the matrix elements for Rydberg states associated for the $N^+ = 0$ and 2 and for states with l =0, 1 and 2. In the actual calculations the Rydberg states included ranged between $n = 25 - 32$, N^+ = 0, 2, 4 and 6 and with l =0, 1, 2 and 3, which resulted in a basis set of 10017 Hund's case (d) states.

The matrix diagonalisation calculations require knowledge of the Hamiltonian for the system. The total Hamiltonian of a molecular system, H, includes the electronic, H_{elec}, and the rotational Hamiltonian, H_{rot}. When an external electric field is applied along the z direction, a perturbation due to the field, H_F is included in the total Hamiltonian.

$$H = H_{elec} + H_{rot} + H_F \tag{4.2}$$

where $H_F = eFz$ and F is the electric field vector in the z direction. Figure 4.1 and the notation used to described the different components of the molecular Hamiltonian is used in a similar manner to Vrakking *et al.* [16].

First the energy matrix (figure 4.1) of the molecular Hamiltonian is constructed, which is then diagonalised to generate the eigenstates and eigenvectors of the Stark Rydberg states for a particular energy region. Before constructing a matrix one needs to decide whether to construct it using Hunds case (b) or (d) basis sets. Since high-n Rydberg states are most effectively described using Hunds case (d) basis set, the matrix will be constructed using Hunds case (d) basis set, where the case (d) basis functions are written $\left|n,l,N^+,N,M_N\right\rangle$. This simplifies the calculations as the rotational part of the Hamiltonian is diagonal. However, the electronic part of the Hamiltonian is not diagonal in a case (d) basis but is almost diagonal in case (b), except for $s\sigma - d\sigma$ configuration mixing and $l-l$ interseries coupling (discussed in more detail later). Hence the electronic part of the Hamiltonian is converted to case (d) basis set from case (b) by applying a

frame transformation. The case (b) matrix elements of the electronic Hamiltonian are (the square bracket notation used for the matrix elements is taken from [16])

$$H_{el}^{(b)}[lN\Lambda, lN\Lambda] = -\mu_{l\Lambda}/\nu^3 \tag{4.3}$$

where $\mu_{l\Lambda}$ is the case (b) quantum defect, which describe the electron-core interactions in the core region. Λ is the projection of the orbital angular momentum of the Rydberg electron along the internuclear axis, ν is the effective principal quantum number, and N is the total angular momentum excluding spin. The values employed in our calculations are taken from [15,16] unless otherwise stated in the text and are listed in Table 4.1.

Λ / l	*0*	*1*	*2*	*3*
0	0.210			
1	0.7038	0.7410		
2	0.05	-0.053	0.089	
3	0.0182	0.0172	0.0128	0.0057

Table 4.1 Hund's case (b) quantum defects used in the matrix diagonalisation calculations in this thesis [15,16]

A frame transformation is required to map the electronic part of the Hamiltonian from this diagonal case (b) basis to the case (d) basis set required for the matrix diagonalisation.

$$H_{el}^{(d)}\left[l, N, N^+; l', N, N^{+'}\right] = \sum_{\Lambda\Lambda'} A_{N^+\Lambda} H_{el}^{b}[l, N, \Lambda; l', N, \Lambda'] A_{N^{+'}\Lambda'} \tag{4.4}$$

where

$$A_{N^+\Lambda} = (-1)^{l+\Lambda-N^+} \begin{pmatrix} l & N & N^+ \\ -\Lambda & \Lambda & 0 \end{pmatrix} (2N^+ + 1)^{\frac{1}{2}} [2/(1+\delta_{\Lambda 0})]^{\frac{1}{2}} \tag{4.5}$$

The matrix elements for the rotational part of the case (d) Hamiltonian are

$$H_{rot}^{(d)}\left[l, N, N^+; l, N, N^+\right] = B_0^+ N^+ (N^+ + 1) - D_0^+ \left(N^+ (N^+ + 1)\right)^2 \tag{4.6}$$

where B_0^+ =1.987825 cm^{-1} is the rotational constant of NO^+ core and D_0^+ = 5.64 x 10^{-6} cm^{-1} is the first centrifugal term [33]. The diagonal matrix elements of the case (d) matrix are $H_{rot}^{(d)}\left[l, N, N^+; l, N, N^+\right] + H_{el}^{(d)}\left[l, N, N^+; l, N, N^+\right]$.

4.2.3 INTRAMOLECULAR COUPLING (SHORT RANGE INTERACTIONS)

Interactions in the core region (short range $l \leq 3$) perturb the energies and positions of the Rydberg states and these interactions are included as off-diagonal matrix elements. The calculations in this thesis include two short-range electron-core interactions.

The $s\sigma - d\sigma$ configuration mixing is accounted for by modifying the case (b) matrix elements in (1):

$$H_{el}^{(b)}[s,N,0;s,N,0] = -\left(\mu_{s\sigma}\cos^2\theta + \mu_{d\sigma}\sin^2\theta\right)/\nu_{s\sigma}^{3/2}\nu_{d\sigma}^{3/2}, \tag{4.7}$$

$$H_{el}^{(b)}[d,N,0;d,N,0] = -\left(\mu_{s\sigma}\sin^2\theta + \mu_{d\sigma}\cos^2\theta\right)/\nu_{s\sigma}^{3/2}\nu_{d\sigma}^{3/2}, \tag{4.8}$$

$$H_{el}^{(b)}[s,N,0;d,N,0] = -\tfrac{1}{2}\left(\mu_{s\sigma} - \mu_{d\sigma}\right)\sin 2\theta/\nu_{s\sigma}^{3/2}\,\nu_{d\sigma}^{3/2}. \tag{4.9}$$

The mixing angle θ, represents the degree of $s\sigma - d\sigma$ mixing, and has a value of -38.7° for NO [3].

The other short-range electron-core interaction is $l-l$ coupling. Rydberg states with the same l, N, but with N^+ differing by two quanta, can be expressed as a sum of case (b) matrix elements for l = 0 or 2. For l = 1 and $l > 2$ the case (b) matrix elements are,

$$H_{el}^{(b)}[l,N,\Lambda;l,N,\Lambda'] = -\mu_{l\Lambda}/\nu_{l\Lambda}^{3/2}\,\nu_{l\Lambda}'^{3/2}. \tag{4.10}$$

The matrix elements for this interaction are labelled as H_{core} [16].

4.2.4 EXTERNAL FIELD COUPLING (LONG RANGE INTERACTIONS)

Having set up the field-free case (d) matrix, the next step is to incorporate the external electric field. The external electric field couples angular momentum states with selection rules

$$\Delta l = \pm 1$$

$$\Delta N = 0, \pm 1$$

$$\Delta N^+ = 0 .$$

The off-diagonal matrix elements of the Stark Hamiltonian are [15,16,29,30],

$$\begin{aligned} H^{(d)}_{Stark}\left[l, N, N^+; l', N', N^{+\prime}\right] &= F\left\langle vN^+ lNM_N \middle| z \middle| v'N^{+\prime} l'N'M'_N \right\rangle \\ &= (-1)^{N-M_N+N'+N^+ +l+1}\left[(2N+1)(2N'+1)\right]^{\frac{1}{2}} \times \\ &\begin{pmatrix} N & 1 & N' \\ -M_N & 0 & M'_N \end{pmatrix} \begin{Bmatrix} l & N & N^+ \\ N' & l' & 1 \end{Bmatrix} \left\langle vl \| r \| v'l' \right\rangle \delta_{N^+ N^{+\prime}} \end{aligned} \tag{4.11}$$

where F is the electric field. The reduced matrix elements are calculated using the Coulomb approximation,

$$\left\langle vl \| r \| v'l' \right\rangle = \begin{cases} -(l+1)^{\frac{1}{2}} \left\langle vl \middle| r \middle| v'l' \right\rangle & l' = l+1 \\ l^{\frac{1}{2}} \left\langle vl \middle| r \middle| v'l' \right\rangle & l' = l-1 \end{cases} \tag{4.12}$$

where

$$\left\langle vl \| r \| v'l' \right\rangle = \left[\tfrac{3}{2} v_c^2 \left(1 - (l_c / v_c)^2\right)^{\frac{1}{2}} \right] \sum_{p=0,3} \gamma^p g_p (v - v') . \tag{4.13}$$

$\gamma = \Delta l (l_c / v_c)$, $l_c = \max(l, l')$, $\Delta l = (l' - l)$ and $v_c = 2/(1/v - 1/v')$. The function $g_p(v - v')$ is tabulated in [34].

4.2.5 INTENSITY

The next step is diagonalisation of the matrix to obtain the eigenvalues E_k and eigenvectors $\phi_k = \sum_i c_{ki}\phi_i^{(d)}$ in the electric field. The intensity of a transition to a particular eigenstate is

$$\left|\langle \phi_k | T | \phi_A \rangle\right|^2 = \left|\sum_i c_{ki} \langle \phi_i^{(d)} | T | \phi_A \rangle\right|^2 \tag{4.14}$$

where $\phi_i^{(d)}$ are the Hund's case (d) basis functions and ϕ_A is the wavefunction of the intermediate level. The zero-field dipole transition moments are determined using [15,16,30]

$$\langle \phi_i^{(d)} | T | \phi_A \rangle = \sum_{l'} (2N'+1)^{\frac{1}{2}} (2N+1)^{\frac{1}{2}} \begin{Bmatrix} N' & l & N^+ \\ l' & N & 1 \end{Bmatrix} \begin{pmatrix} l & N^+ & N' \\ 0 & 0 & 0 \end{pmatrix} A_{l'}(l) \tag{4.15}$$

where $A_{l'}(l)$ are adjustable parameters that give the best fit for the zero-field spectra. The 4 best parameters used for our calculations *via* the two rovibrational intermediate states $A^2\Sigma^+(v'=0, N'=0)$ and $A^2\Sigma^+(v'=0, N'=2)$ are listed in Table 4.2

$l'-l$	$A_{l'}(l)$
$p-s$	0.1
$s-p$	0.7
$d-p$	0.1
$d-f$	1.0

Table 4.2 $A_{l'}(l)$ values used for simulations of spectra *via* the $A^2\Sigma^+(v'=0, N'=0)$ and $A^2\Sigma^+(v'=0, N'=2)$ intermediate states.

In our experiments there is a delay, t = 70 ns, between the laser pulse employed to excite the Rydberg states and the pulsed electric field employed to field-ionise them. During this time, the Rydberg states can predissociate. The predissociation rate of a particular eigenstate, k, is the weighted average of the predissociation rates of its component case (d) states

$$\Gamma_k = \sum_i c_{ki}^2 \Gamma_i^{(d)} \tag{4.16}$$

Therefore, the intensity of a transition to an eigenstate, k, is weighted by a decay factor, $\exp(-t/\tau_k)$, where $\tau_k = h/(2\pi\Gamma_k)$. Table 4.3 lists the decay rates found in literature. The decay rates employed in these calculations are the same as Vrakking [16] as these gave the most accurate fit with our experimental data. The

resulting line spectra are then convoluted with a Gaussian frequency profile. The FWHM is 0.15 cm^{-1}, which provides the best fit to the experimental spectra.

	Zero Field Decay Parameters (cm^{-1})	
$\Gamma_i^{(d)}$	Vrakking	Goodgame
s	500	3750
p	1610	4000
d	1000	1000
f	43	1500

Table 4.3 Zero field decay parameters reported in literature, used in the matrix diagonalisation calculations. The calculations in this thesis use the Vrakking decay rates.

4.3 RESULTS

4.3.1 ZERO-FIELD SPECTRA

Pulsed-field ionisation spectra recorded by $(1+1')$ double-resonance excitation *via* the $N' = 0, 1, 2$ and 3 rotational states (J' = 1/2, 3/2, 5/2 and 7/2) of the

intermediate *A*-state $(v' = 0)$ are presented in figures 4.2(a)-(d). In all spectra, the Rydberg series converge to different rotational states of the ground vibrational state of the molecular ion and are distinguishable up to around n = 50. In accordance with the angular momentum and parity selection rules $\mathbf{N}' + \boldsymbol{\gamma} = \mathbf{N}^+ + \mathbf{l}$ and $p_{Ryd}\, p' = -1$ (section 4.2.1), one would expect to see p and f Rydberg series; however, the f Rydberg series dominate all our spectra, suggesting that the lifetime of the *np* states is shorter than the delay between the laser excitation and pulsed-field ionisation. The relatively simple spectrum recorded *via* the rotationless $N' = 0$ intermediate presented in figure 4.2(a) illustrates this nicely. The *f*(2) Rydberg series has the greatest intensity, although the *p*(0) series is also observed. Below 30430 cm^{-1} the *nf*(2) Rydberg states dominates the spectrum. The first evidence of the *p*(0) series is observed at 28*p*(0). The intensity of this series is considerably lower than the *f*(2) series. One exception to this is the 30*p*(0) state, which is almost degenerate with the 28*f*(2) state and as a consequence undergoes intensity sharing, most probably through $p\sigma - f\sigma$ or $p\pi - f\pi$ interactions that are not included in our matrix diagonalisation model.

The zero-field spectra recorded *via* the $N' = 1, 2$ and 3 rotational intermediate states are more congested due to the larger number of spectroscopically allowed Rydberg series. According to parity rules, a Rydberg spectrum recorded *via* the N' = 1 rotational state should result in transitions to p and f series converging to rotational states of the ion with angular momenta N^+ = 1, 3 and 5. Although there does not appear to be one dominant series in figure 2(b), it is apparent that both the *f*(1) and *f*(3) Rydberg series have significant intensity. At higher n a new

rather weak series emerges, which has been assigned as the *f*(5) series on the basis of the quantum defects.

The spectrum presented in figure 4.2(c) is recorded *via* the $N' = 2$ intermediate state and, like figure 4.2(a) which was recorded *via* the $N' = 0$ state, is dominated by Rydberg series converging to rotational states of the ion core with even quantum numbers N^+ = 0, 2 and 4. In figure 4.2(c), the *f*(0), *f*(2) and *f*(4) Rydberg series all have similar intensity, whereas in figure 4.2(a), only *f*(2) Rydberg series has significant intensity.

The spectrum recorded *via* the $N' = 3$ rotational intermediate state, illustrated in figure 4.2(d), is dominated by Rydberg series converging to rotational states of the ion core with odd quantum numbers N^+ = 1, 3 and 5, similar to 4.2(b). The two main series observed are the *f*(1) and *f*(3) Rydberg series with little contribution from the *f*(5) series. A significant difference between 4.2(d) and 4.2(b) is the appearance of the *p*(3) series at high *n*. Since the measurable predissociation lifetime of Rydberg states is proportional to the cube of the principal quantum number, *n*, states with higher *n* are expected to have a longer lifetime.

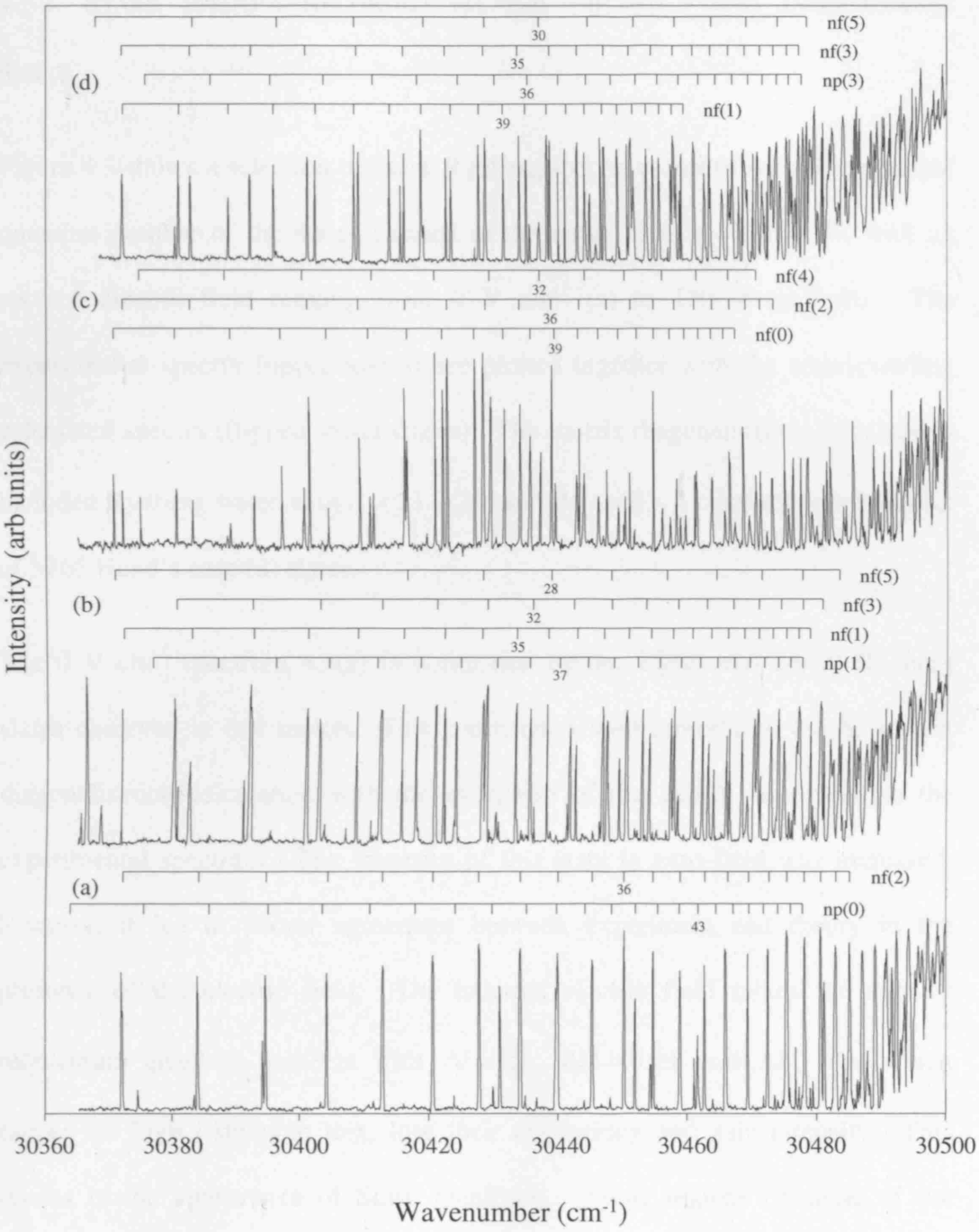

Figure 4.2 Zero field $(1+1')$ pulsed-field ionisation spectra of Rydberg states of NO converging on the $v^+ = 0$ ionization limit *via* (a) $N' = 0$, (b) $N' = 1$, (c) $N' = 2$, and (d) $N' = 3$ rotational states of the intermediate

4.3.2 STARK SPECTRA RECORDED *VIA* THE $A(v' = 0, N' = 0)$ INTERMEDIATE STATE

Figure 4.3 shows a selection of Stark Rydberg spectra recorded with the principal quantum number of the states excited in the range from n = 25 – 27, with an applied electric field ranging from 0 V cm^{-1} (a) to 120 V cm^{-1} (h). The experimental spectra (upper traces) are plotted together with the corresponding calculated spectra (flipped lower traces). The matrix diagonalisation calculations included Rydberg states with n = 21 – 29, and N^+ = 0 – 4 resulting in a basis set of 5265 Hund's case (d) states.

The 0 V cm^{-1} spectrum 4.3(a) is dominated by the 25*f*(2) and 26*f*(2) Rydberg states observed in this region. This spectrum is well reproduced by the matrix diagonalisation calculation with the exception of the 28*p*(0) state seen in the experimental spectrum. The intensity of this state in zero-field was increased; however, it led to poorer agreement between experiment and theory in the presence of the electric field. The external electric field mixes the angular momentum quantum numbers with $\Delta l = \pm 1$, $\Delta N = 0, \pm 1$ and $\Delta N^+ = 0$, which causes the high l states to mix, lose their degeneracy and gain intensity. This results in the appearance of Stark manifolds. Some regions of some of the experimental spectra have been magnified to aid comparison with calculated spectra, although it should be noted that the original experimental intensities are real and reproducible. For example, in the 20 V cm^{-1} spectrum around 30364.3 cm^{-1} the experimental spectrum has been magnified by a factor of 5 to highlight the presence of the 26*d*(1) manifold which is not otherwise obvious.

In the lowest fields, a change in the peak structures emerges: the intensity distribution of the *nf*(2) states spreads (both in the experimental and calculated spectra) and a double peak structure begins to appear at 20 V cm^{-1}. The double peaks at 30360 cm^{-1} and 30372 cm^{-1} belong to the 25(2), 26(0) pair and the 26(2), 27(0) pair of Stark manifolds, respectively. In fields of 40 V cm^{-1} (and higher) the manifolds become more distinguishable as the splitting increases and they gain intensity. At the higher fields, the expanding manifolds begin to overlap with neighbouring manifolds leading to a more complex structure. This is well reproduced in the simulations. The intensity of the 28*p*(0) state observed at zero field decreases with increasing field strength, and almost disappears into the neighbouring $N^+ = 1$ and 0 manifolds. An applied electric field does not mix different core states directly and so it has most likely mixed into the neighbouring 27(0) manifold.

The *d*(1) Rydberg series is also observed when an electric field is applied and is reproduced by the calculated spectrum. As the applied field increases, a manifold with $N^+ = 1$ character develops. Although there may be some *s* character in the same region, it is hard to distinguish due to *s*/*d* mixing. In comparison to the $N^+ = 2$ manifolds, the $N^+ = 1$ manifolds have lower intensity and almost vanish at high fields.

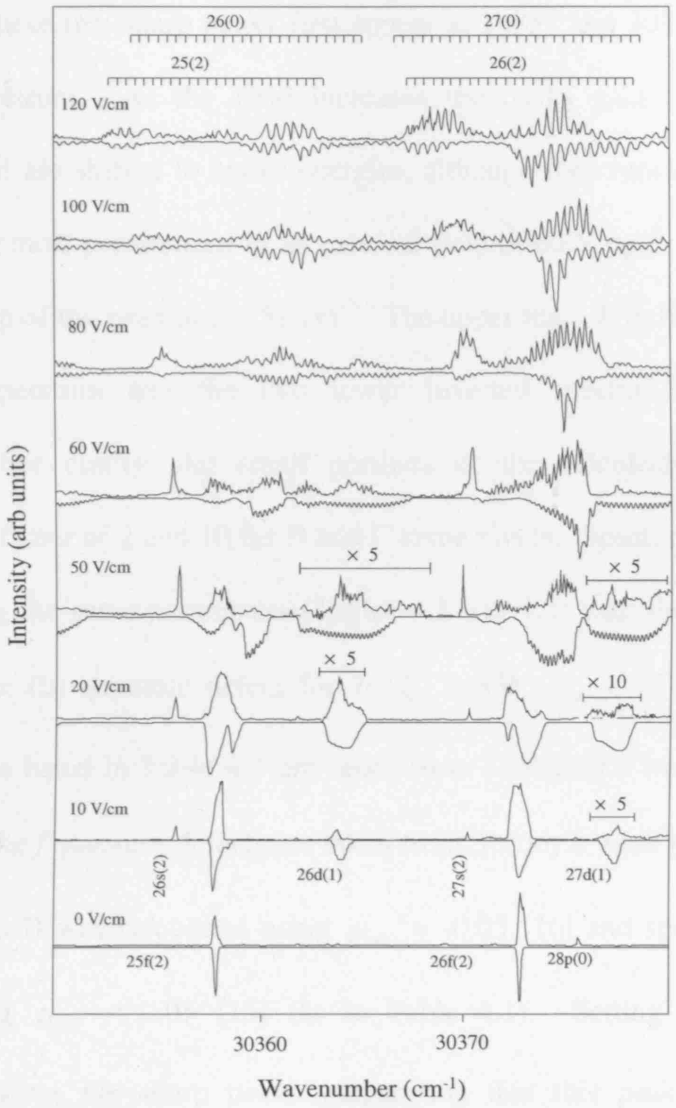

Figure 4.3 Stark spectra of Rydberg states of NO converging to the $v^+ = 0$ ionisation limit with principal quantum number n = 25-26 excited *via* the $A^2\Sigma^+(v' = 0, N' = 0)$ state. The different traces correspond to applied electric fields ranging from 0 – 120 V cm^{-1}. The upper traces are the experimental spectra and the lower inverted spectra are the corresponding calculated simulations. The relative intensities of the spectra have been adjusted for clarity. Some regions of the spectra have been magnified.

Another new feature emerging on application of the applied field are two very sharp peaks. These two sharp peaks first appear at 30357 and 30370 cm^{-1} in the 10 V cm^{-1} spectrum. As the field increases the peaks gain intensity quite dramatically and are shifted to lower energies, although they remain very sharp. These peaks are most pronounced in an external field of 60 V cm^{-1}. Figure 4.4(b) shows a close up of the peak at 30357 cm^{-1}. The upper trace A in figure (b) is the experimental spectrum and the two lower inverted spectra B and C are calculations. For clarity, the small portions of the calculated spectra are magnified by a factor of 2 and 10 for B and C respectively. Spectra B and C were calculated using the same parameters (Tables 4.1 and 4.2) with the exception of the Hund's case (b) quantum defect for $l=2$, $\Lambda=0$ ($\mu_{d\sigma}$). The *s*, *p*, and *d* quantum-defects listed in Table 4.1 are taken from Vrakking's work [16] (other than $\mu_{d\sigma}$) and the *f* quantum-defects are taken from Softley's work [15]. In figure 4.4(b), spectrum B was calculated using $\mu_{d\sigma}$ = -0.05 [16] and spectrum C was calculated using $\mu_{d\sigma}$ = 0.05 [15] (as in Table 4.1). Setting $\mu_{d\sigma}$ = -0.05 completely removes the sharp peak, suggesting that this peak has some *d* character; however, when compared with energies calculated using the Rydberg equation $E = IP - R_{NO}/(n-\delta_l)^2$, it becomes clear that these peaks do not originate from Rydberg states of *d* character but belong to the *s*(2) series. According to the selection rules given in section 4.2.1, these states have almost no intensity in zero-field and so it is assumed that they are gaining significant intensity through the process of field induced coupling with allowed Rydberg states. Since the intensity of these peaks is so dependent on the value of the *d* quantum defect it is

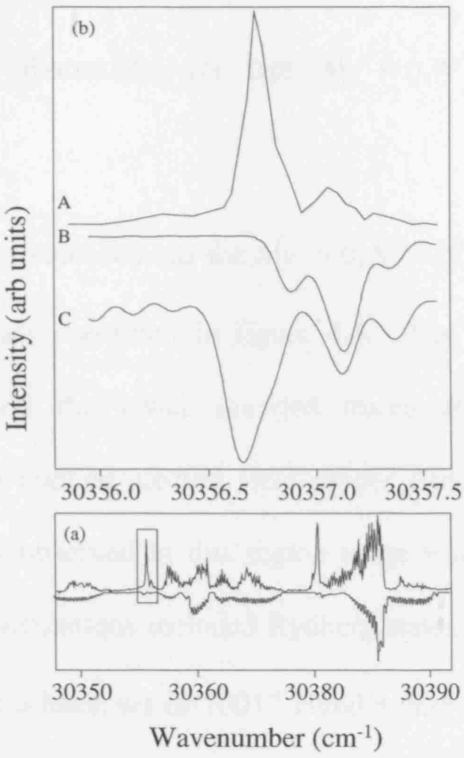

Figure 4.4 Rydberg spectrum recorded *via* the $A^2\Sigma^+(v' = 0, N' = 0)$ state in an applied electric field of 60 V cm^{-1}. The upper trace is the experimental spectrum and the lower flipped trace is the corresponding calculated spectrum. The highlighted peak in (a) is expanded in (b). (b) The upper trace A is the experimental spectrum and the flipped traces are matrix diagonalisation simulations. Trace C was calculated using the parameters listed in table 4.1 and 4.2. Trace B is as trace C except the $l = 2$, $\Lambda = 0$ Hunds case (d) quantum defect which has a value of -0.05 (Vrakking, [16]). For clarity B and C are magnified by factors of 2 and 10 respectively.

reasonable to assume that the appearance of these peaks is due to $s\sigma - d\sigma$ coupling [3,35] and $d(2) - f(2)$ Stark mixing. A more quantitative analysis would require precise MQDT calculations incorporating all the small inter-series couplings. As the applied electric field increases above 60 V cm^{-1}, these sharp peaks begin to spread and mix into neighbouring $N^+ = 2$ manifolds, which supports our assignment of $N^+ = 2$ character.

4.3.3 STARK SPECTRA RECORDED *VIA* THE $A(v' = 0, N' = 2)$ INTERMEDIATE STATE

A range of Stark spectra, recorded *via* the $A(v' = 0, N' = 2)$ intermediate state at various electric fields, are presented in figure 4.5. The upper traces are the experimental spectra and the lower inverted traces are the corresponding calculated spectra. The applied electric field ranges from (a) 0 V cm^{-1} to (f) 100 V cm^{-1}. The states observed in this region range from n = 25 – 32. The matrix diagonalisation calculations included Rydberg states with n = 21 – 29, and N^+ = 0 – 6 resulting in a basis set of 10017 Hund's case (d) states. As above, some regions of some of the experimental spectra have been magnified to show the agreement between the spectral features in the experimental and calculated spectra, although it should be noted that the original experimental intensities are real and reproducible.

The experimental zero field spectrum in this energy range is dominated by the $f(0)$ and $f(2)$ Rydberg series with a smaller contribution from the $f(4)$ series. An exception to this observation is the 28$f(2)$ state, which in comparison to the other $nf(2)$ states has a much lower intensity. This intensity anomaly is present at both low and high electric fields. As the electric field increases, the 28$f(2)$ state begins to split and at 10 V cm^{-1} two distinctive sharp peaks appear at 30382.61 cm^{-1} and 30383.13 cm^{-1}. These peaks are assigned to the 28$f(2)$ and the 30$p(0)$ states. In zero-field the 28$f(2)$ state is almost degenerate with the 30$p(0)$ which is interpreted to imply that in a field, d-f and d-p coupling can force an intensity transfer from the f to p state.

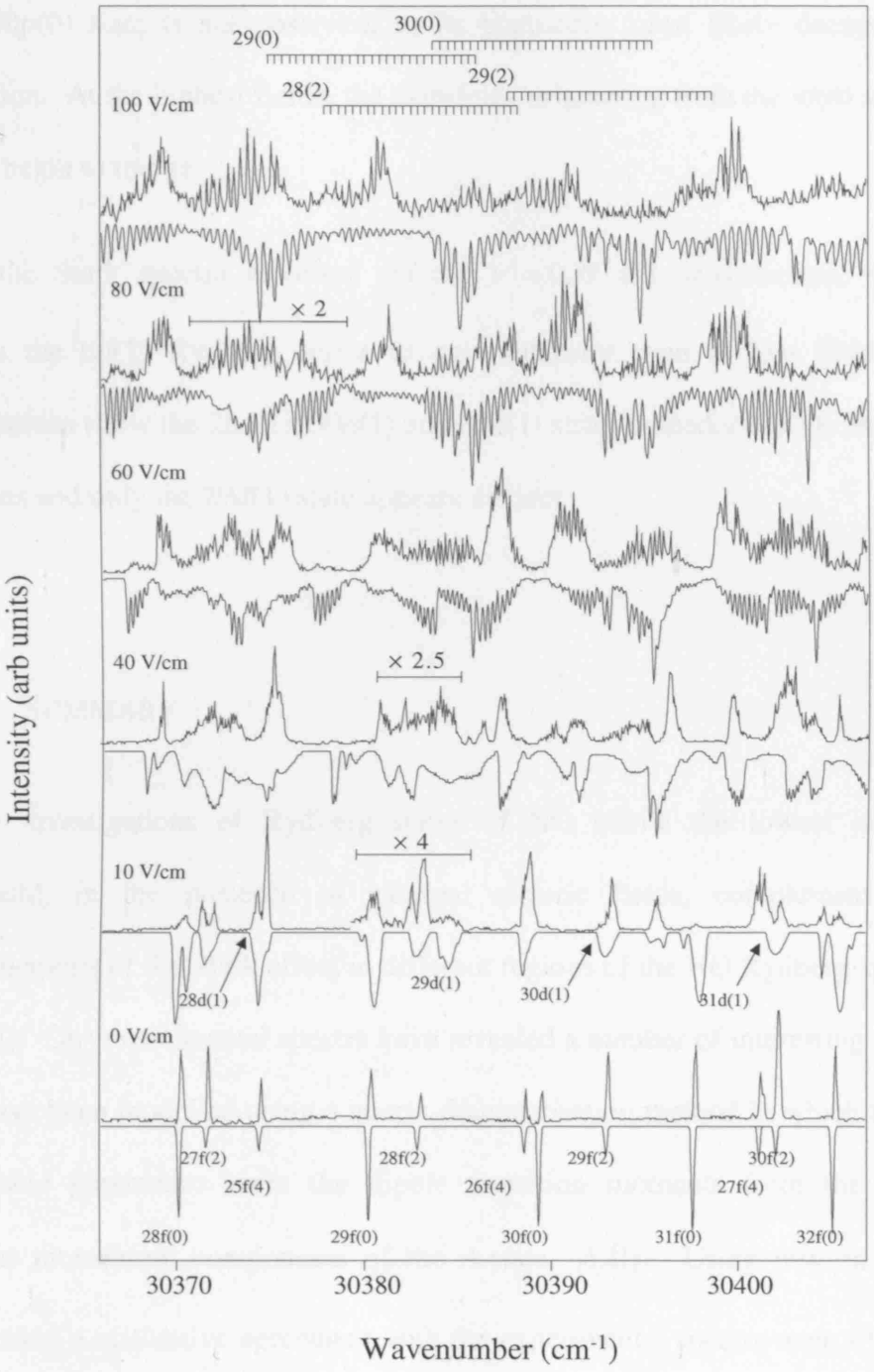

Figure 4.5 Stark spectra of Rydberg states of NO converging to the $v^+ = 0$ ionisation limit with principal quantum number n = 25 - 26 excited *via* $A^2\Sigma^+(v' = 0, N' = 2)$ state. The different traces correspond to applied electric fields ranging from 0 – 100 V cm^{-1}. The upper traces are the experimental spectra and the lower inverted traces are the corresponding calculated spectra. The relative intensities of the spectra have been adjusted for clarity. Some regions of the spectra have been magnified.

The $30p(0)$ state is not observed, as its population most likely decays before detection. At the highest fields, the manifolds originating from the $nf(0)$ and $nf(2)$ states begin to merge.

Like the Stark spectra recorded *via* the $v' = 0, N' = 2$ intermediate, the field causes the $nd(1)$ Rydberg series to gain intensity even at low fields. Our calculations show the $28d(1)$, $30d(1)$ and $31d(1)$ states embedded in the expanding nf states and only the $29d(1)$ state appears distinct.

4.4 SUMMARY

These investigations of Rydberg states of NO below the lowest ionisation threshold, in the presence of external electric fields, complement earlier investigations of the Stark effect in different regions of the NO Rydberg spectrum [15-17]. Our experimental spectra have revealed a number of interesting features that have been modelled using a matrix diagonalisation method in which the only adjustable parameters were the dipole transition moments from the various angular momentum components of the A-state, $A_{l'}(l)$. Using just one set of parameters a qualitative agreement with the experimental spectra over a range of principal quantum numbers, n = 25 – 32, in fields of 0 – 120 V cm^{-1} was obtained, *via* two different rotational states of the A-state.

4.5 REFERENCES

1. D. T. Biernacki, S. D. Colson, and E. E. Eyler, *Journal Of Chemical Physics* **88** (4), 2099 (1988).
2. D. T. Biernacki, S. D. Colson, and E. E. Eyler, *Journal Of Chemical Physics* **89** (5), 2599 (1988).
3. S. Fredin, D. Gauyacq, M. Horani, C. Jungen, G. Lefevre, and F. Masnouseeuws, *Molecular Physics* **60** (4), 825 (1987).
4. K. P. Huber, M. Huber, and E. Miescher, *Physics Letters* **3** (7), 315 (1963).
5. S. T. Pratt, C. Jungen, and E. Miescher, *Journal Of Chemical Physics* **90** (11), 5971 (1989).
6. K. P. Huber, M. Vervloet, C. Jungen, and A. L. Roche, *Molecular Physics* **61** (2), 501 (1987).
7. E. Miescher, *Canadian Journal Of Physics* **54** (20), 2074 (1976).
8. M. Raoult, *J. Chem. Phys.* **87** (8), 4736 (1987).
9. D. Uy, C. M. Gabrys, T. Oka, B. J. Cotterell, R. J. Stickland, C. Jungen, and A. Wuest, *Journal Of Chemical Physics* **113** (22), 10143 (2000).
10. R. A. L. Smith, V. G. Stavros, J. R. R. Verlet, H. H. Fielding, D. Townsend, and T. P. Softley, *Journal Of Chemical Physics* **119** (6), 3085 (2003).
11. R. A. L. Smith, J. R. R. Verlet, E. D. Boleat, V. G. Stavros, and H. H. Fielding, *Faraday Discussions* **115** (63) (2000).
12. V. G. Stavros, J. A. Ramswell, R. A. L. Smith, J. R. R. Verlet, J. Lei, and H. H. Fielding, *Physical Review Letters* **83** (13), 2552 (1999).

13. R. S. Minns, R. Patel, J. R. R. Verlet, and H. H. Fielding, *Physical Review Letters* **91** (24) (2003).

14. R. S. Minns, J. R. R. Verlet, L. J. Watkins, and H. H. Fielding, *Journal Of Chemical Physics* **119** (12), 5842 (2003).

15. A. L. Goodgame, H. Dickinson, S. R. Mackenzie, and T. P. Softley, *Journal Of Chemical Physics* **116** (12), 4922 (2002).

16. M. J. J. Vrakking, *Journal Of Chemical Physics* **105** (17), 7336 (1996).

17. J. B. M. Warntjes, F. Robicheaux, J. M. Bakker, and L. D. Noordam, *Journal Of Chemical Physics* **111** (6), 2556 (1999).

18. S. N. Dixit, D. L. Lynch, V. McKoy, and W. M. Huo, *Physical Review A* **32** (2), 1267 (1985).

19. K. Kaufmann, C. Nager, and M. Jungen, *Chemical Physics* **95** (3), 385 (1985).

20. A. Fujii and N. Morita, *Chemical Physics Leters* **182** (3-4), 304 (1991).

21. A. Fujii and N. Morita, *Journal Of Chemical Physics* **97** (1), 327 (1992).

22. A. Fujii and N. Morita, *Journal Of Chemical Physics* **98** (6), 4581 (1993).

23. A. Fujii and N. Morita, *Laser Chemistry* **13** (3-4), 259 (1994).

24. A. Fujii and N. Morita, *Journal Of Chemical Physics* **103** (14), 6029 (1995).

25. L. E. Jusinski, G. E. Gadd, G. Black, and T. G. Slanger, *Journal Of Chemical Physics* **90** (8), 4282 (1989).

26. H. Umemoto and K. Matsumoto, *Journal Of the Chemical Society-Faraday Transactions* **92** (8), 1315 (1996).

27. A. Giusti-Suzor and Ch. Jungen, *Journal Of Chemical Physics* **80** (3), 986 (1984).

28. M. L. Zimmerman, M. G. Littman, M. M. Kash, and D. Kleppner, *Physical Review A* **20** (6), 2251 (1979).

29. W. E. Ernst, T. P. Softley, and R. N. Zare, *Physical Review A* **37** (11), 4172 (1988).

30. M. Bixon and J. Jortner, *Journal Of Chemical Physics* **103** (11), 4431 (1995).

31. R. D. Knight and L. G. Wang, *Physical Review A* **32** (2), 896 (1985).

32. H. H. Fielding and T. P. Softley, *Chemical Physics Letters* **185** (3-4), 199 (1991).

33. K. Sakimoto, *Journal Of Physics B-Atomic Molecular And Optical Physics* **22** (17), 2727 (1989).

34. C. Jungen, *Private communication.*

35. G. Herzberg, *Spectra of Diatomic molecules.* Van-Nostrand-Reinhold, Princton, New Jersey, 1950.

36. A. R. Edmonds, J. Picart, N. Tranminh, and R. Pullen, *Journal Of Physics B-Atomic Molecular And Optical Physics* **12** (17), 2781 (1979).

37. D. Gauyacq, A. L. Roche, M. Seaver, S. D. Colson, and W. A. Chupka, *Molecular Physics* **71** (6), 1311 (1990).

CHAPTER 5

ROTATION-STATE SELECTIVE FIELD IONISATION OF MOLECULAR RYDBERG STATES

ABSTRACT

In this chapter selective field ionisation spectra of highly excited Rydberg states of NO are presented, and the competition between electron-nuclear coupling and electron-field coupling is investigated. It is shown that the slew rate of the electric field can be used as a control parameter for steering molecules prepared in one rotational quantum state, into molecular ions in different rotational quantum states, i.e. to control the field-ionisation product.

5.1 INTRODUCTION

Selective field-ionisation (SFI) has been exploited widely as an experimental tool to measure the composition and character of highly excited Rydberg states of atoms. In SFI, a ramped electric field applied to a Rydberg atom has the effect of creating a saddle point in the Coulomb potential and lowering the classical ionisation limit, which eventually leads to ionisation. The mechanism of field-ionisation, and hence the field at which a particular Rydberg state is ionised, is highly dependent on the rate at which the electric field is increased; however, atoms in different Rydberg states tend to ionise at different fields, so it is possible to identify Rydberg states by their field-ionisation signal. There have been numerous investigations of SFI mechanisms in atomic Rydberg systems [1-7], in particular Na [1,5-8] and the heavier alkali metals Rb and Cs [9-13]. SFI has been applied to infer Rydberg state populations from ionisation signals in various wave packet experiments [8,14-16], e.g. to determine the amplitude of shaped wave packets in Cs [14] and to assess fitness in a coherent control experiment in Na [8]. It has been shown that changing the shape of the ramped field can improve the selectivity of field-ionisation, e.g. [11]. Shaped SFI ramps have also proved a useful tool in pulsed-field ionisation zero-kinetic energy (PFI-ZEKE) photoelectron spectroscopy [9,17-19]. In the context of ZEKE spectroscopy, there have been several investigations of the effects of electric fields on the lifetimes of very high molecular Rydberg states [19-26]. SFI has also been applied to control the diabatic versus adiabatic field dissociation of heavy Rydberg systems [27]. However, the dynamics of SFI of molecular Rydberg states has not been investigated. In a molecular Rydberg system, there are Rydberg series converging

to each rovibronic state of the ion, and not only is the density of states very high but these series interact with one another leading to a very complex and irregular Rydberg spectrum. On the application of a slow rising electric field pulse, the field-ionisation routes become more complicated than in an atomic system because there is the additional possibility of transferring population between Rydberg series associated with different rotational states of the ion core.

In this chapter, the SFI of highly excited Rydberg states of NO in a densely populated region of the spectrum below the first ionisation limit are investigated. Following this, the competition between electron-nuclear coupling and electron-field coupling is explored.

5.2 STARK EFFECT/FIELD IONISATION

In a Rydberg system, an applied electric field mixes orbital angular momentum states with $\Delta l = \pm 1$. The high angular momentum states ($l \geq 3$) that are nearly degenerate in zero-field, fan out almost linearly with increasing field until neighbouring n manifolds cross ($F = 1/3n^5$). In non-hydrogenic atoms or molecules, all the levels of the manifold are coupled by the Rydberg-ionic core interaction and form multilevel avoided crossings (or Landau-Zener crossings) in the region $F > 1/3n^5$. When the electric field is ramped, the mechanism by which these avoided crossings are traversed depends on the speed at which they are approached, which in turn depends on the gradients of the potential curves,

dE/dF, and the slew rate of the electric field, dF/dt. The probability of making a diabatic transition is approximately [28-31]

$$P_{diabatic} = \exp\left[-\frac{2\pi|V_{12}|^2}{|dE_1/dF - dE_2/dF| \cdot dF/dt}\right], \tag{5.1}$$

where V_{12} is the coupling matrix of the interaction causing the avoided crossing and the separation of states at the crossing $W_{12} = 2V_{12}$ (atomic units). The rate of change of the energy separation is, $dW_{12}/dt = |dE_1/dF - dE_2/dF| \cdot dF/dt$. For slow enough slew rates (a few hundred V cm^{-1} μs^{-1}), the preferential route to the ionisation continuum tends to be *via* the adiabatic path, in which case the electron is ionised at the classical field-ionisation threshold, $F = 1/16n^4$. For rapid slew rates (a few hundred V cm^{-1} ns^{-1}), the system tends to follow the diabatic path and the electron is ionised at the higher field strength, $F = 1/9n^4$. In a Rydberg molecule, there are series of Stark manifolds, $n(N^+)$, associated with each rotational state of the molecular ion, N^+, each of which is independently characterised by its own adiabatic and diabatic field-ionisation thresholds. Furthermore, manifolds associated with different rotational states that are coupled by zero-field core interactions will form additional avoided crossings, and when the electric field is ramped there is the possibility for population to be transferred adiabatically from one rotational quantum state to another.

5.3 RESULTS

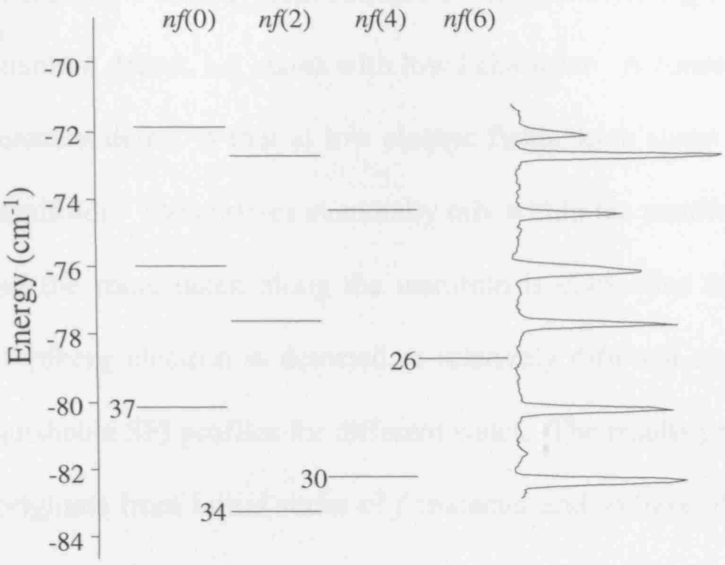

Figure 5.1 An energy level diagram showing the interleaved $f(N^+)$ Rydberg series accessible from the $A^2\Sigma^+(v'=0, N'=2, J'=5/2)$ state of NO, together with a portion of the corresponding 1+1 resonance – enhanced multiphoton ionisation spectrum. The vertical scale represents the binding energy with respect to the $N^+=0$ ionisation limit.

A portion of the Rydberg spectrum, obtained by collecting the total electron yield as a function of the wavenumber of the second laser is plotted in figure. 5.1. The Rydberg series accessed from the *A*-state are labelled using the notation $nl(N^+)$. Taking into account the angular momentum composition of the *A*-state, which is 94% *s* and 5% *d*, [32,33] and the selection and propensity rules, we would expect to access *p*(0), *p*(2), *p*(4), *f*(0), *f*(2), *f*(4), *f*(6) Rydberg series from the $v'=0, N'=2, J'=5/2$ intermediate; however, the *f* Rydberg series dominate the spectrum, indicating that the lifetime of the *np* states is shorter than the delay between the laser excitation and pulsed-field ionisation [34,35].

Previous experiments [2,5,7,8,10,11,36] that have employed ramped fields to ionise Rydberg states have mainly concentrated on atomic Rydberg states with relatively high quantum defect, i.e. states with low l character. A consequence of having a high quantum defect is that at low electric fields these states are offset from the Stark manifolds. These states eventually mix within the manifold at high enough fields and the route taken along the manifold is distinctive for specific states, thus the Rydberg electron is detected at relatively different times. This generates distinguishable SFI profiles for different states. The results presented in this chapter all originate from initial states of f character and so have almost zero quantum defect. As a result these states mix heavily into their adjacent manifolds at very low fields and so one might expect their SFI profiles to be similar in structure. However the results presented in this chapter show otherwise. Figure. 5.2 presents a set of SFI profiles recorded using a ramped field with a slew rate of 2.3 V cm^{-1} ns^{-1}, comparing the change in structure when ionising Rydberg states differing in n and N^+. The field ionisation profiles for the 34f(2), 30f(4), 37f(0), 35f(2), 38f(0), 31f(4), 36f(2) and 39f(0) Rydberg states are plotted in the order they appear in the zero field frequency spectrum. It is apparent that the profiles for the different states differ significantly. A consequence of the 34f(2) state lying lower in energy is that it catches a slower part of the ramped electric field pulse. This suggests that the route to ionisation along the Stark map includes significant adiabatic crossings, resulting in a more complicated structured profile. In contrast the 39f(0) ionisation profile is more simple and contains one dominant peak which is assigned as the pure diabatic route to ionisation (into the $N^+ = 0$ continuum).

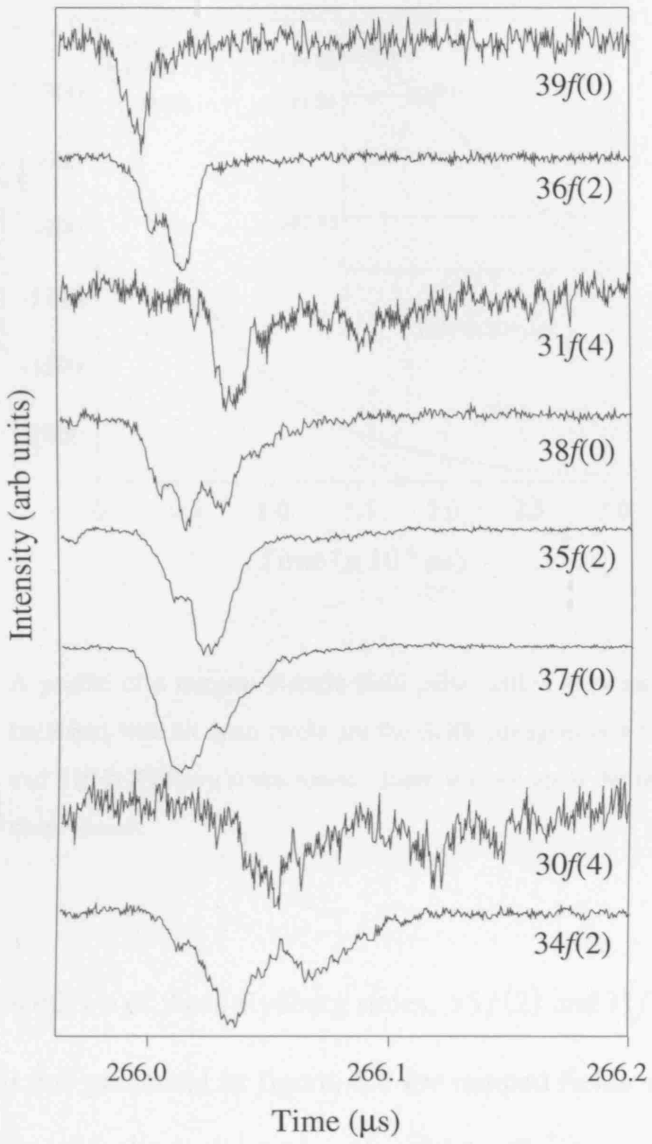

Figure 5.2 Measured SFI signal excited from a range of Rydberg states differing in principal quantum number, n, electronic angular momentum, l and in core rotational quantum number N^+. The pulsed field used to ionise the states is ramped from 0 V cm^{-1} to 2000 V cm^{-1} with a rise time of 870 ns (slew rate 2.3 V cm^{-1} ns^{-1}).

In figure 5.3 a plot of a ramped electric field pulse with a slew rate of 1.3 V cm^{-1} ns^{-1} is given. Highlighted are the field strengths at which the 39*f*(0), 36*f*(2) and 31*f*(4) Rydberg states field ionise.

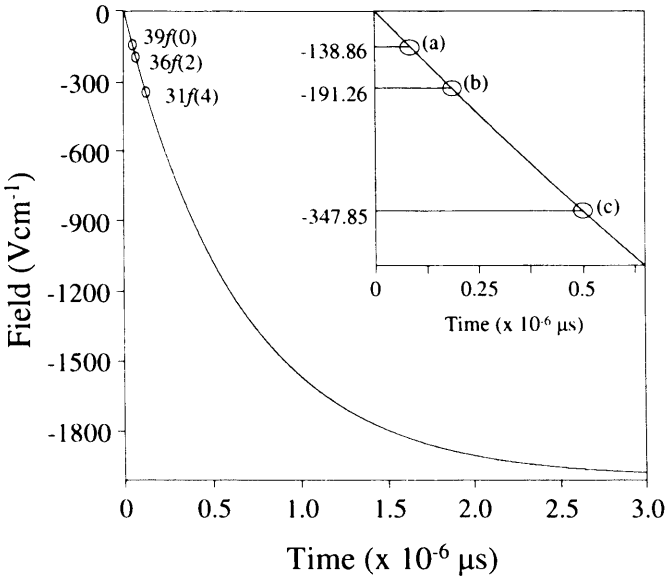

Figure 5.3 A profile of a ramped electric field pulse with a slew rate of 1.3 V cm^{-1} ns^{-1}. Indicated with an open circle are the fields strengths at which the 39*f*(0), 36*f*(2) and 31*f*(4) Rydberg states ionise. Inset: a close up of the region where the three states ionise.

The SFI profiles of two of these Rydberg states, $35f(2)$ and $31f(4)$, are analysed in greater detail and presented in figure. 5.4 for ramped fields with slew rates in the range 6.9 V cm^{-1} ns^{-1} (a) to 1.3 V cm^{-1} ns^{-1} (e). The *f* states have very small quantum defects (~0.01) [37-39] and are mixed rapidly into their adjacent Stark manifolds even in weak fields. As the ramped electric field is applied, population placed initially in one $nf(N^+)$ Rydberg state will follow the path of the lowest energy Stark state of the $n(N^+)$ manifold until it crosses an adjacent manifold. The first avoided crossing takes place with the highest energy Stark state of a manifold associated with a different rotational state, and from this point on the ionisation path is determined by the slew rate and the strength of the coupling between the two states (equation 5.1).

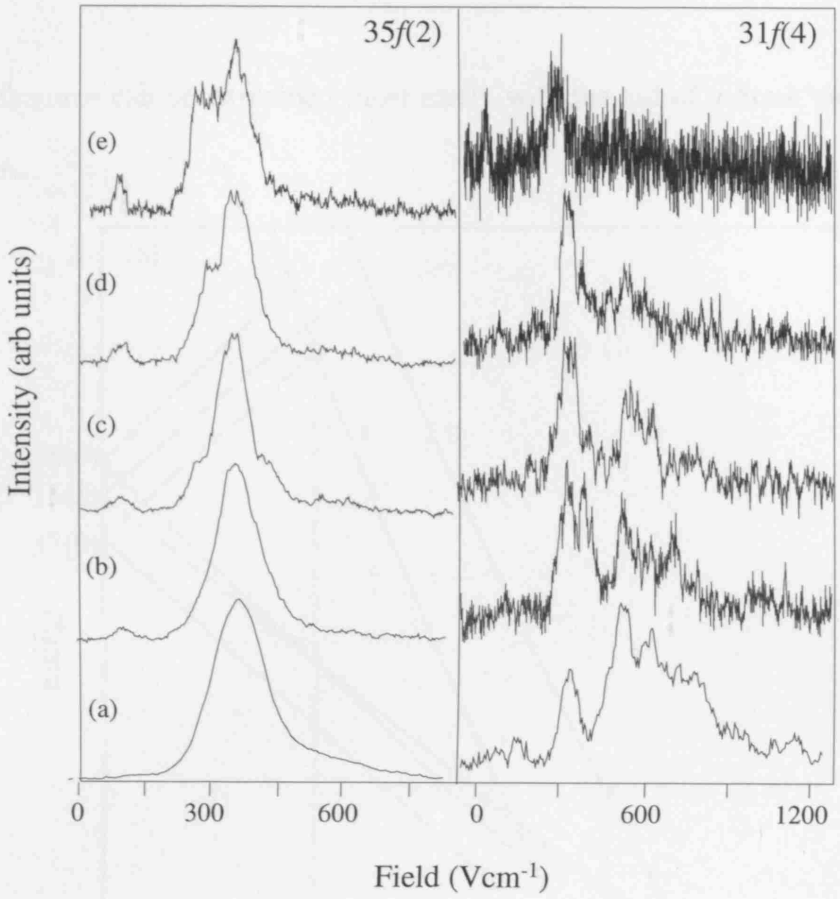

Figure 5.4 Measured SFI signals of the 35*f*(2) and 31*f*(4) Rydberg states of NO at slew rates of (a) 6.9, (b) 3.7, (c) 2.8, (d) 2.3 and (e) 1.3 V cm^{-1} ns^{-1}.

5.3.1 SELECTIVE FIELD IONISATION OF THE 35*f*(2) RYDBERG STATE

Consider the SFI profile of the $35f(2)$ state with a slew rate of 6.9 V cm^{-1} ns^{-1} (figure. 5.4(a)). Most of the molecules ionise when the field is ~370 V cm^{-1}, which corresponds to diabatic ionisation into the $N^+ = 2$ continuum. When the slew rate is decreased to 3.7 V cm^{-1} ns^{-1} (figure. 5.3(b)), an additional peak appears in the SFI profile at ~120 V cm^{-1} and this peak grows as the slew rate is decreased further (figure. 5.4(c)-(e)). At 2.8 V cm^{-1} ns^{-1} (figure. 5.4(c)) a shoulder begins to appear on the low field side of the diabatic peak at ~370 V cm^{-1} and becomes more pronounced as the slew rate is further decreased (figure.5.4(d)-(e)).

These features can be explained most easily with the aid of a Stark energy level diagram.

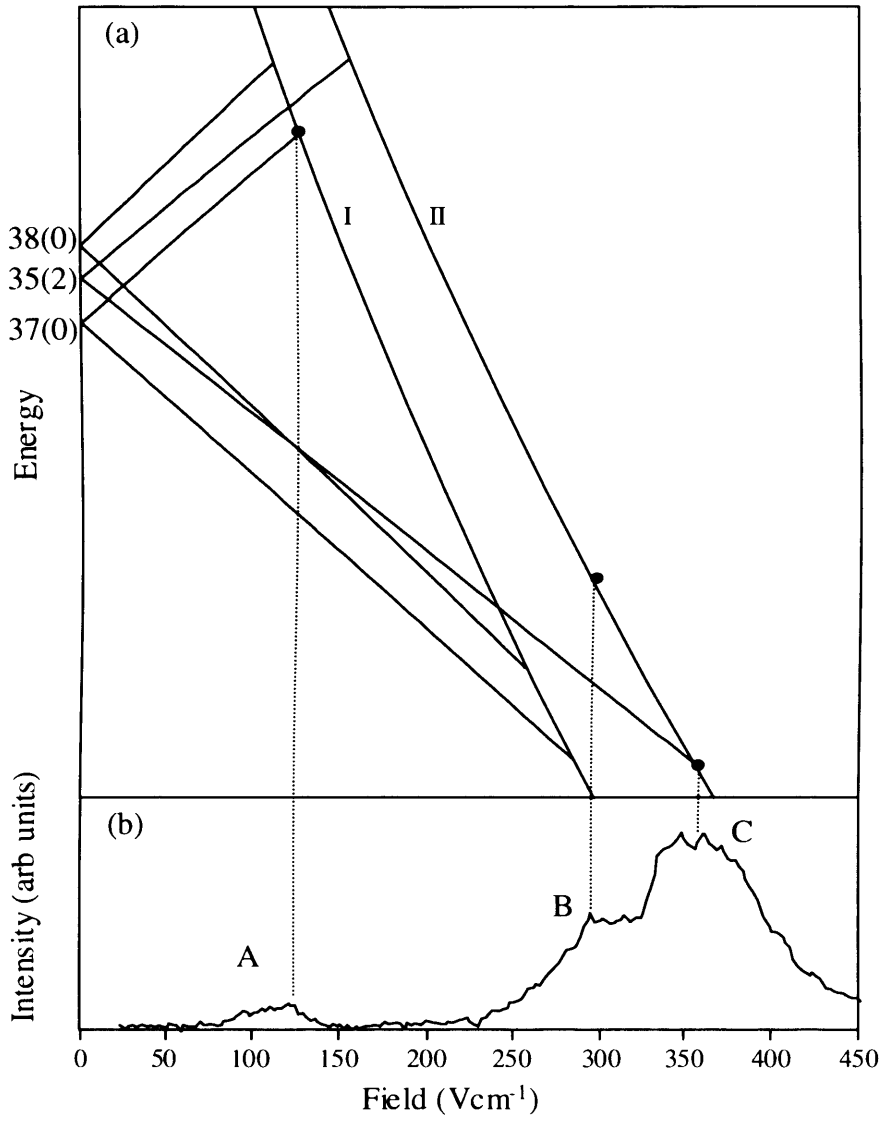

Figure 5.5 (a) Extreme members of the m = 0 hydrogenic Stark manifolds for 37(0), 35(2) and 38(0) high-l Rydberg states, calculated to the first order using equation 1.10. Curves I and II represent the classical field-ionisation limits ($F = 1/16n^4$) of the $N^+ = 0$ and $N^+ = 2$ Rydberg series, respectively. (b) SFI profile of the 35f(2) Rydberg state with a slew rate of 2.3 V cm^{-1} ns^{-1}.

In figure 5.5 the extreme members of the m = 0 hydrogenic Stark manifolds, calculated by first-order perturbation theory, are plotted for the 37(0), 35(2) and

38(0) states. The classical field-ionisation limits, $E = B_0 N^+(N^+ + 1) - 6.12\sqrt{F}$ cm^{-1}, are plotted for adiabatic ionisation into $N^+ = 0$ and $N^+ = 2$ continua. B_0 = 1.988 cm^{-1} is the rotational constant, and F is in units of V cm^{-1}. A detailed Stark map for NO is calculated for states in the vicinity of the first avoided crossing, using a matrix-diagonalisation method [35] (figure. 5.6). As the field is ramped up, the 35*f*(2) state mixes into the 35(2) manifold almost immediately and the population follows the lowest energy state of the 35(2) Stark manifold until it reaches an avoided crossing with the 37(0) manifold at ~16 V cm^{-1} (figure 5.5), which arises due to a zero-field coupling between rotational states with $\Delta N^+ = \pm 2$. For the fastest slew rate, the population continues on the diabatic path to the $N^+ = 2$ classical field-ionisation limit at ~370 V cm^{-1} (figure 5.5 peak C). This is in perfect agreement with the probability, $P_{diabatic} = 1.00$, calculated using equation 5.1 and parameters listed in table 5.1 with respect to figure 5.7. At 3.7 V cm^{-1} ns^{-1} (figure. 5.4(b)) most of the population still makes this crossing diabatically, although a measurable fraction crosses adiabatically onto the highest energy Stark state of the 37(0) manifold, where it is then transferred diabatically to the $N^+ = 0$ continuum (peak A in figure. 5.5). As the slew rate decreases further, the probability of adiabatic transfer is enhanced and this feature gains intensity. At 1.3 V cm^{-1} ns^{-1} (figure. 5.4(e)), the experimentally measured fraction of electrons making this crossing adiabatically is 0.03, which is in good agreement with the probability calculated using equation 5.1, $P_{diabatic} = 0.98$.

At 2.8 V cm^{-1} ns^{-1} (figure. 5.4(c)), a broad shoulder emerges at fields 250–340 V cm^{-1} and becomes more pronounced as the field is increased. This is

interpreted in terms of the increasing number of adiabatic crossings on the route to the $N^+ = 2$ classical field-ionisation limit (figure. 5.5 B-C).

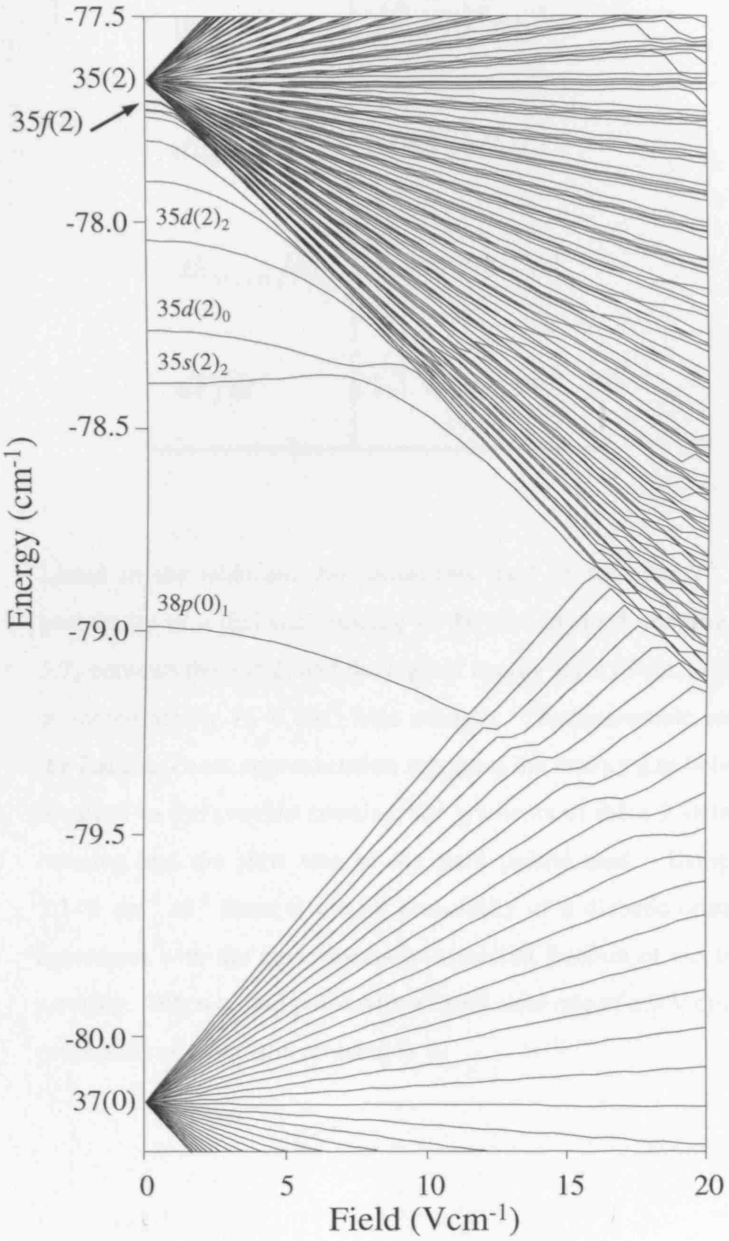

Figure 5.6 Stark map for states in the vicinity of the first avoided crossing between 35*f*(2) and a Stark state from the 37(0) manifold in the field strength region of 0 – 20 V cm^{-1}, calculated using a hybrid MQDT and matrix-diagonalisation method [40]. The zero-field non degenerate states are labelled using the $nl(N^+)_N$ notation where n is the principal quantum number, l is the electron orbital angular momentum, N^+ is the ion core rotational quantum number and N is the total angular momentum excluding spin, $\mathbf{N} = \mathbf{N}^+ + \mathbf{l}$.

Parameters	*Values*
$W_{37(0),35f(2)}$	3.8×10^{-3} cm^{-1}
$dE_{37(0)}/dF$	0.084 cm^{-1} V^{-1}
$dE_{35f(2)}/dF$	-0.071 cm^{-1} V^{-1}
dF/dt	1.3 V cm^{-1} ns^{-1}

Table 5.1 Listed in the table are the parameters used in equation 5.1 to calculate the probability of a diabatic crossing at the first avoided crossing (figure. 5.6 and 5.7) between the 35*f*(2) and the highest energy level of the 37(0) Stark manifold at approximately 16 V cm^{-1} field strength. The measurable parameters used in the Landau-Zener approximation represent the energy gap between the 2 states involved in the avoided crossing, the gradients of these 2 states at the avoided crossing and the slew rate of the field pulsed used. Using a slew rate of 1.3 V cm^{-1} ns^{-1} there is a 0.98 probability of a diabatic crossing which is in agreement with the experimentally measured fraction of electrons making this crossing. When a field pulse with a faster slew rate of 6.9 V cm^{-1} ns^{-1} is used the probability of a diabatic crossing is 1.

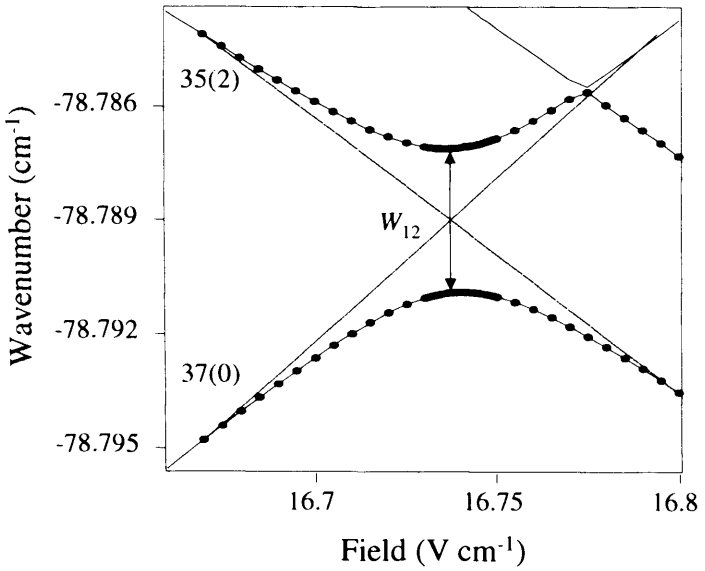

Figure 5.7 The first avoided crossing between the 35*f*(2) Stark state with the highest energy Stark state of the 37(0) manifold. The probability of crossing an isolated avoided crossing diabatically is determined using the Landau-Zener approximation, which takes into consideration the energy gap between the states labelled 1 and 2 at the avoided crossing, W_{12} and the difference in the gradient of the two states. The energy levels are calculated using a matrix diagonalisation method [35].

5.3.2 SELECTIVE FIELD IONISATION OF THE 31*f*(4) RYDBERG STATE

Now consider the SFI profile of the $31f(4)$ state with the fastest slew rate of 6.9 V cm^{-1} ns^{-1} (figure. 5.4(a)). The molecules ionise over a range of fields from 180 – 1100 V cm^{-1}. The SFI profile is highly structured and the peaks can be assigned to a number of ionisation pathways. The 31*f*(4) state mixes into the 31(4) manifold almost immediately and as the field is ramped the population follows the lowest energy Stark state of this manifold until it meets the first avoided crossing with the highest energy Stark state of the 38(0) manifold. $\Delta N^+ = \pm 4$ coupling is weak, so the avoided crossing between these two states will be very small and at this slew rate, and in fact for all slew rates employed in this work, there is no evidence for any adiabatic population transfer to $N^+ = 0$.

The next avoided crossing takes place with the highest energy Stark state of the 35(2) manifold at ~24 V cm^{-1} (figure 5.8(a) and figure 5.9(A)). Zero-field core coupling between rotational states with $\Delta N^+ = \pm 2$ is stronger and a fraction of the population is transferred adiabatically to the 35(2) manifold where it continues diabatically to the $N^+ = 2$ continuum at ~160 V cm^{-1} (figure 5.8(b) peak A). Alternatively, the Rydberg population may cross the interleaved manifolds adiabatically until it crosses onto the lower energy Stark states of the 36(2) manifold (figure 5.8(a) and figure. 5.9(B)) where it would then continue diabatically to the $N^+ = 2$ continuum at ~330 V cm^{-1} (figure 5.8(b) peak B). The population that remained on the lowest energy Stark state of the 31(4) manifold meets the next avoided crossing, with the 26(6) manifold, at ~77 V cm^{-1} (figure 5.8(a) and figure 5.9(C)). The zero-field coupling between the 31(4) and 26(6) states clearly results in a significant fraction of the population being transferred adiabatically to the highest energy Stark state of the 26(6) manifold, which is then transferred diabatically to the $N^+ = 6$ ionisation continuum at ~525 V cm^{-1} (figure 5.8(b) peak C). This is the most intense peak at the slowest slew rate (figure 5.4(e)). Peak D is attributed to purely diabatic ionisation of 31*f*(4) into the $N^+ = 4$ ionisation continuum at 600 V cm^{-1} (figure 5.8(a) and figure. 5.9(D)). Peak E in figure 5.8(b) must arise from population travelling diabatically along the lowest energy Stark state of the 26(6) manifold to the classical field-ionisation threshold at 1100 V cm^{-1}. Adiabatic population transfer from the 31*f*(4) to a range of Stark states belonging to the 26(6) manifold gives rise to the SFI signal in the range 600 - 1100 V cm^{-1}. As the slew rate is decreased (figure. 5.4(b)-(e)), the probability of adiabatic transfer at each of the crossings increases. At the slowest

slew rates the purely adiabatic ionisation to the $N^+ = 4$ continuum (figure 5.8(b) peak B) is the most intense although there are still some molecules ionising into $N^+ = 6$ at ~525 V cm^{-1} (figure 5.8(b) peak C).

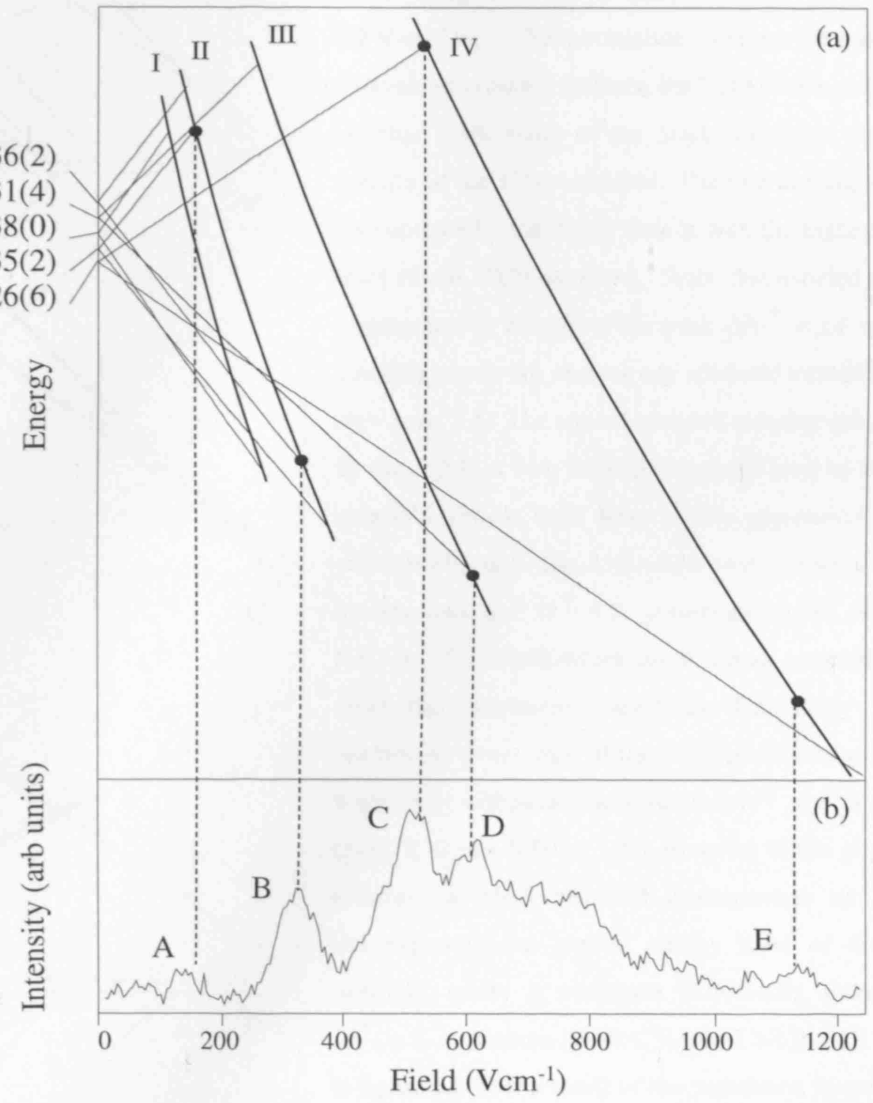

Figure 5.8 (a) Extreme members of the m = 0 hydrogenic Stark manifolds for 26(6), 35(2), 38(0), 31(4) and 36(2) high-l Rydberg states, calculated using first order perturbation theory. Curves I, II, III and IV represent the classical field-ionisation limits ($F = 1/16n^4$) of the $N^+ = 0$, $N^+ = 2$, $N^+ = 4$ and $N^+ = 6$ Rydberg series, respectively. (b) SFI profile of the 31*f*(4) Rydberg state with a slew rate of 6.9 V cm^{-1} ns^{-1}. Figure 5.9 shows the mechanism of how these peaks appear.

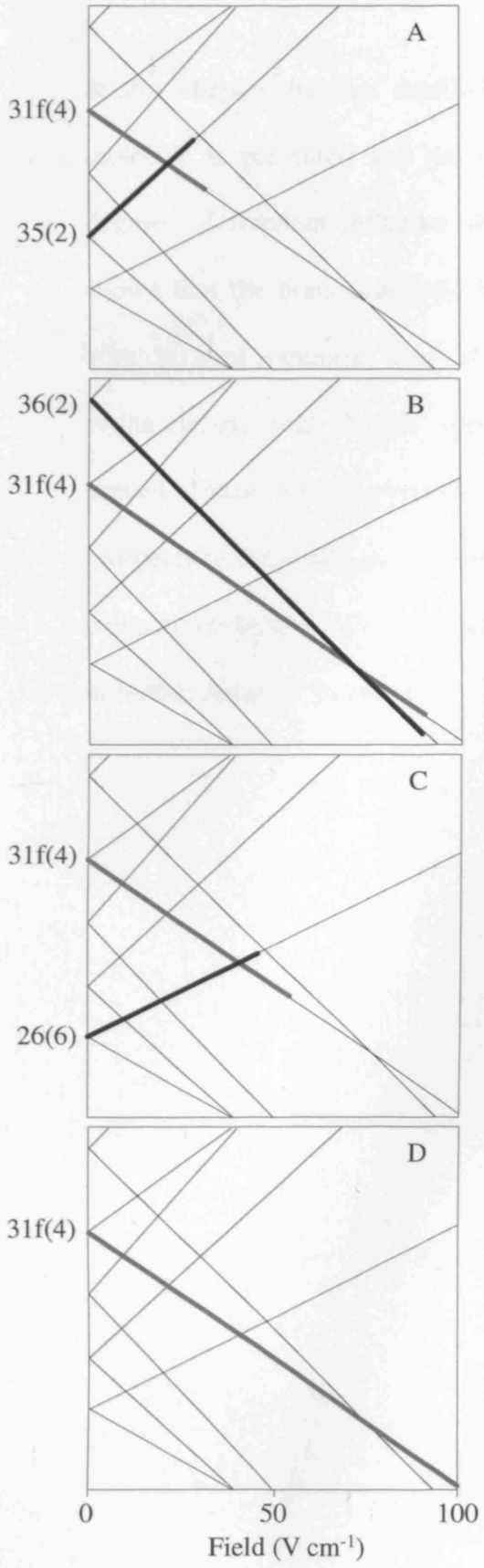

Figure 5.9

Schematic diagrams illustrating the mechanism by which the peak structure of the field ionisation profile of the 31*f*(4) state (grey bold line) in figure 5.8(b) is obtained when using a field ionisation with a slew rate of 6.9 V cm^{-1} ns^{-1}. The mechanism considers the traversal of an avoided crossing between the 31*f*(4) state and various extreme Stark states of the Stark manifolds within the vicinity of the 31(4) manifold. The first avoided crossing encountered by the 31*f*(4) state is with the highest energy level of the 37(0) manifold. Since this avoided crossing is generated as a result of the weak $\Delta N^+ = \pm 4$ zero field coupling we do not observe any adiabatic transition at this slew rate. (A) The second avoided crossing encountered by the 31*f*(4) is with the highest energy level of the 35(2) manifold (black bold line). The population crosses adiabatically onto the 35(2) state and continues until it ionises into the $N^+ = 2$ continuum (peak A figure. 5.8(b)). (B) Alternatively the Rydberg population may cross the interleaved manifolds diabatically until it reaches the lower state of the 36(2) manifold from where it proceeds diabatically towards the $N^+ = 2$ continuum (peak B figure 5.8(b)). (C) However if the population remains on 31(4) manifold it encounters an avoided crossing with the highest energy level of the 26(6) manifold where it continues diabatically towards the $N^+ = 6$ continuum (peak C figure 5.8(b)). (D) Peak D in figure 5.8(b) is a result of the population remaining on the 31(4) manifold and ionising in the $N^+ = 6$ continuum.

5.4 SUMMARY

In this chapter the first detailed investigations of SFI of Rydberg states in a molecule is presented and the mechanisms behind how the various rotational degrees of freedom influence the field-ionisation process are explored. It is shown that the branching ratio between the field-ionisation continua associated with different rotational states of the molecular ion is controlled by the slew rate of the electric field. Future work will aim to investigate the possibility of using shaped electric fields to improve the rotational selectivity and to investigate the prospects of using SFI as a tool to control more molecular phenomena such as the competition between field-ionisation and predissociation. This will be discussed in further detail in chapter 6.

5.5 REFERENCES

1. J. L. Vialle and H. T. Duong, *Journal Of Physics B-Atomic Molecular And Optical Physics* **12** (8), 1407 (1979).
2. J. H. M. Neijzen and A. Donszelmann, *Journal Of Physics B-Atomic Molecular And Optical Physics* **15** (13), 1981 (1982).
3. K. B. Macadam, D. B. Smith, and R. G. Rolfes, *Journal Of Physics B-Atomic Molecular And Optical Physics* **18** (3), 441 (1985).
4. F. G. Kellert, T. H. Jeys, G. B. McMillian, K. A. Smith, F. B. Dunning, and R. F. Stebbings, *Physical Review A* **23** (3), 1127 (1981).
5. T. H. Jeys, G. W. Foltz, K. A. Smith, E. J. Beiting, F. G. Kellert, F. B. Dunning, and R. F. Stebbings, *Physical Review Letters* **44** (6), 390 (1980).
6. T. F. Gallagher, L. M. Humphrey, R. M. Hill, and S. A. Edelstein, *Physical Review Letters* **37** (22), 1465 (1976).
7. T. F. Gallagher, L. M. Humphrey, W. E. Cooke, R. M. Hill, and S. A. Edelstein, *Physical Review A* **16** (3), 1098 (1977).
8. R. E. Carley, E. D. Boleat, R. S. Minns, R. Patel, and H. H. Fielding, *Journal Of Physics B-Atomic Molecular And Optical Physics* **38** (12), 1907 (2005).
9. M. Tada, Y. Kishimoto, M. Shibata, K. Kominato, S. Yamada, T. Haseyama, I. Ogawa, H. Funahashi, K. Yamamoto, and S. Matsuki, *Physics Letters A* **303** (4), 285 (2002).
10. F. Robicheaux, C. Wesdorp, and L. D. Noordam, *Physical Review A* **62** (4), 043404 (2000).
11. A. Gurtler and W. J. van der Zande, *Physics Letters A* **324** (4), 315 (2004).

12. T. F. Gallagher, B. E. Perry, K. A. Safinya, and W. Sandner, *Physical Review A* **24** (6), 3249 (1981).

13. M. Gatzke, J. R. Veale, W. R. Swindell, and T. F. Gallagher, *Physical Review A* **54** (3), 2492 (1996).

14. T. C. Weinacht, J. Ahn, and P. H. Bucksbaum, *Physical Review Letters* **80** (25), 5508 (1998).

15. S. N. Pisharody and R. R. Jones, *Physical Review A* **65** (3), 033418 (2002).

16. J. H. Hoogenraad and L. D. Noordam, *Physical Review A* **57** (6), 4533 (1998).

17. G. Reiser, W. Habenicht, and K. Mullerdethlefs, *Chemical Physics Letters* **152** (2-3), 119 (1988).

18. U. Hollenstein, R. Seiler, H. Schmutz, M. Andrist, and F. Merkt, *Journal Of Chemical Physics* **115** (12), 5461 (2001).

19. H. J. Dietrich, K. Muller-Dethlefs, and L. Y. Baranov, *Physical Review Letters* **76** (19), 3530 (1996).

20. M. Bixon and J. Jortner, *Journal Of Chemical Physics* **105** (4), 1363 (1996).

21. C. Bordas, P. F. Brevet, M. Broyer, J. Chevaleyre, P. Labastie, and J. P. Perrot, *Physical Review Letters* **60** (10), 917 (1988).

22. W. A. Chupka, *Journal Of Chemical Physics* **99** (8), 5800 (1993).

23. W. A. Chupka, *Journal Of Chemical Physics* **98** (6), 4520 (1993).

24. S. T. Pratt, *Journal Of Chemical Physics* **98** (12), 9241 (1993).

25. W. G. Scherzer, H. L. Selzle, E. W. Schlag, and R. D. Levine, *Physical Review Letters* **72** (10), 1435 (1994).

26. M. J. J. Vrakking and Y. T. Lee, *Physical Review A* **51** (2), R894 (1995).

27. R. C. Shiell, E. Reinhold, F. Magnus, and W. Ubachs, *Physical Review Letters* **95** (21), 213002 (2005).

28. D. A. Harmin and P. N. Price, *Physical Review A* **49** (3), 1933 (1994).

29. D. A. Harmin, *Physical Review A* **56** (1), 232 (1997).

30. D. A. Harmin, *Physical Review Letters* **49** (2), 128 (1982).

31. D. A. Harmin, *Physical Review A* **26** (5), 2656 (1982).

32. S. N. Dixit, D. L. Lynch, V. McKoy, and W. M. Huo, *Physical Review A* **32** (2), 1267 (1985).

33. K. Kaufmann, C. Nager, and M. Jungen, *Chemical Physics* **95** (3), 385 (1985).

34. M. Raoult, *J. Chem. Phys.* **87** (8), 4736 (1987).

35. R. Patel, N. J. A. Jones, and H. H. Fielding, *Journal Of Physics B-Atomic Molecular And Optical Physics* **40**, 1369 (2007).

36. M. Forre and J. P. Hansen, *Physical Review A* **67** (5), 053402 (2003).

37. E. F. McCormack, F. Di Teodoro, J. M. Grochocinski, and S. T. Pratt, *Journal Of Chemical Physics* **109** (1), 63 (1998).

38. C. Jungen and E. Miescher, *Canadian Journal Of Physics* **47** (17), 1769 (1969).

39. D. T. Biernacki, S. D. Colson, and E. E. Eyler, *Journal Of Chemical Physics* **88** (4), 2099 (1988).

40. M. J. J. Vrakking, *Journal Of Chemical Physics* **105** (17), 7336 (1996).

CHAPTER 6

SUMMARY AND OUTLOOK

ABSTRACT

This thesis presents work investigating the application of static and ramped electric fields to molecular Rydberg states. The Rydberg states of NO were chosen for investigation due to the experimental ease they offer. The region of Rydberg states with principal quantum number in the range n = 25 – 32 was considered. In chapter 4, a static electric field was applied resulting in the appearance of new spectroscopic features. In chapter 5, the application of electrical pulses with varying slew rates drove the Rydberg electrons through various pathways along the Stark manifold towards field ionisation. Future investigations will use shaped electrical fields to give greater control over this process.

6.1 SUMMARY

6.1.1 INTRODUCTION

The motivation for the experimental work presented in this thesis stemmed from an initially planned Rydberg wave packet coherent control experiment in NO. A recent application of molecular Rydberg wave packets is their use in understanding the mechanisms of chemical reactivity [1], and in particular to behave as optical reagents to control chemical reactions. This "coherent control" approach takes advantage of the dual quantum and classical property that wave packets possess: After initial formation, the wave packet behaves classically as it oscillates between the inner and outer turning point at the classical (Kepler) orbit period. At longer times, the wave packet disperses and the purely classical picture is no longer applicable (and quantum wave-like behaviour becomes dominant).

Over the past decade, the topic of coherent control has been one of the leading areas of research in chemical physics. To obtain insight and understanding into the electronic and nuclear dynamics of individual atoms in a molecular system could potentially enable one to influence all fundamental processes of chemistry, biology and materials science. Coherent control experiments have been approached from many different aspects [1] ranging from the control of angular momentum in atoms [2] to quantum computing techniques [3-7]. Experiments have taken place in a vast number of systems from simple atoms such as Na [8,9], to large complicated biological molecules [9]. The currently most popular method to selectively control processes in large molecules is through the use of tailored waveforms generated by feedback-controlled learning loops. The understanding

behind the fundamental physics of these processes, especially within larger molecules, is not fully developed due to the complexity of the spectroscopy. For this reason, one of the growing research areas within coherent control is to develop a technique which can accurately describe the dynamical processes that occur when the molecular energy levels interact with pulses of laser radiation, with the aim of developing shaped laser pulses to achieve a desired outcome. This can be achieved by using an intuitive control scheme in which a sequence of light pulses is designed such that each step in the sequence is understood when the light pulse interacts with the molecule.

One experiment which demonstrates control over electron wave packet composition through the use of a sequence of laser pulses, was carried out in the Xenon atom [2]. Our group showed that is was possible to control the orbital angular momentum character of an electron wave packet, which was initially created from a superposition of *s* and *d* Rydberg series. The different quantum defects of the *s* and *d* series ensured that at a given time and for a specific excitation energy, the two angular momentum components of the wave packet would be out of phase with one another. At this point it was possible to selectively pump down (depopulate) either all, or a fraction of one or other angular momentum component.

A similar method was applied to an experiment in the sodium atom [8]. The control scheme for this experiment required a 2 pulse sequence, one to excite the wave packet and the second to excite another interfering wave packet after a specific time delay. The Rydberg wave packets were created centred on $n = 35$

so that the relative phase position of the 35*s* and 34*d* states were accessible. Using state-selective field ionisation (SSFI) coupled with the optical Ramsey method they were able to monitor the phase evolution of the resultant wave packet, and the modulating population of the Rydberg states involved as a function of time.

Our proposed experiment takes this idea a step further by applying it to a more complex molecular system, NO. We propose to apply a coherent control scheme, using a sequence of laser pulses, to the bound Rydberg states of NO and to detect the direct resultant population using SFI. The idea for this work is similar to earlier work in our group which employed a sequence of laser pulses to selectively remove Rydberg states of a specific rotational character from Rydberg wave packets, consisting predominately of two Rydberg series, excited in the autoionising region of NO [10]. The detection technique used in this work was the optical Ramsey method, in which the final Rydberg population is not directly measured. With the use of SFI, the population of the final Rydberg states in our work would be measured directly.

A two pulse sequence will create a bound Rydberg wave packet and, after a time delay, a second identical wave packet would interfere with the first. The resultant tailored wave packet would be detected using SFI and the final Rydberg state populations would be measured directly. This would be achieved through understanding and manipulation of the relative phases between the various Rydberg series and the phase of the laser pulses. In planning these experiments, the first step taken was to gain a thorough understanding of the phase information

within the molecule by recording the relevant Rydberg frequency spectra. These spectra were taken to confirm exactly the composition of the wave packets excited and corresponding SFI traces were recorded as 'fingerprints' to allow easy interpretation of any wave packet SFI. However, we found that the SFI profiles were almost indistinguishable and so to gain better insight into the observed SFI profiles, we investigated the effect of applying a static electric field to the frequency spectra of the bound Rydberg states. This lead us to the work presented here: Stark Rydberg frequency spectra in NO excited *via* the ($v' = 0, N' = 0$) and ($v' = 0, N' = 2$) states of the intermediate $A^2\Sigma^+$ state. The spectra were recorded in the principal quantum number range $n = 24 - 32$. To interpret the experimental spectra, calculated spectra using the matrix diagonalisation method are also presented.

The selective field ionisation profiles (chapter 5) were recorded with an improved experimental set-up in which the electron MCP was bought closer to the interaction region. This set-up resulted in the ionised electrons being detected almost immediately which lead to distinguishable ionisation profiles for different Rydberg states. The results presented in this thesis are summarised in the following sections.

6.1.2 CHAPTER 4: OBSERVATION OF THE STARK EFFECT IN $\nu^+ = 0$ RYDBERG STATES OF NO WITH A MATRIX DIAGONALISATION ANALYSIS

In chapter 4 the Stark spectra of NO recorded by double resonance *via* the $v' = 0, N' = 0$, and $v' = 0, N' = 2$ rovibrational states of the intermediate $A^2\Sigma^+$ state were presented. From these results many interesting spectroscopic features were observed, for example the Stark spectra recorded *via* the $v' = 0, N' = 0$ rotational state of the intermediate revealed the emergence of the *ns*(2) Rydberg series as a result of electric field induced coupling with allowed Rydberg states. Similarly, the Stark spectra recorded *via* the $v' = 0, N' = 2$ rovibrational state of the intermediate state showed the appearance of an unexpected Stark manifold, which was accurately reproduced using a matrix diagonalisation calculation. In these calculations the experimental spectra for both intermediates states were well simulated by matrix diagonalisation using just one set of dipole transition moment parameters of the *A*-state. There were a few anomalies in the intensities of a portion of the spectra that were not reproduced using the matrix diagonalisation method. An example of such an anomaly is reproduced in figure 6.1. In the zero field Rydberg spectrum recorded *via* the $A(v' = 0, N' = 0)$ intermediate state it is evident that the *nf*(2) Rydberg series dominates and this is well reproduced in the calculated spectrum. Also observed in the experimental spectrum is the 28*p*(0) state which is not seen in the calculated spectrum. By giving the *np*(0) Rydberg series more intensity at zero field, poorer agreement between experiment and theory in the presence of an electric field was observed. MQDT calculations

currently being undertaken in our group could explain the intensity anomalies found in the matrix diagonalisation calculations in this thesis.

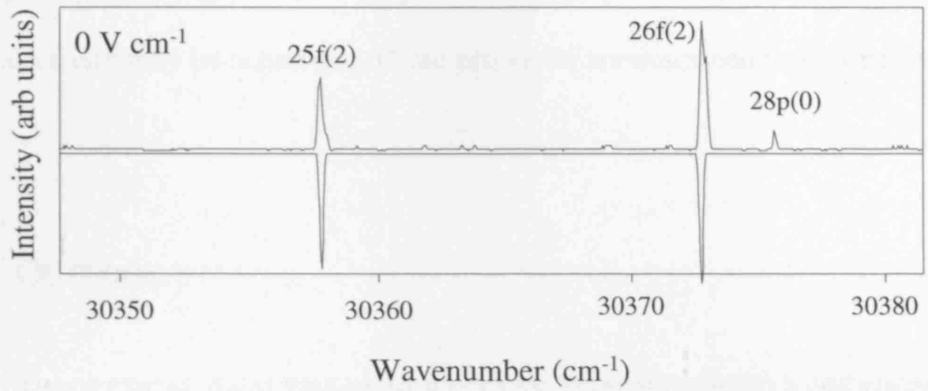

Figure 6.1 The zero field spectrum of the Rydberg states of NO converging to the $v^+ = 0$ ionisation limit with principal quantum number n = 25 - 26 excited *via* the $A^2\Sigma^+(v' = 0, N' = 0)$ state. The upper trace is the experimental spectrum and the lower inverted spectrum is the corresponding calculated simulation.

6.1.3 CHAPTER 5: ROTATION-STATE SELECTIVE FIELD IONISATION OF MOLECULAR RYDBERG STATES

In chapter 5 the first investigations of rotational selective field ionisation of molecular Rydberg states were presented. By varying the slew rate of the electric field pulse the final route to ionisation was manipulated. The final composition of the field ionised molecules was changed from one rotational quantum state into another. In the case of the 31*f*(4) Rydberg state, when applying a electric field pulse with a slew rate of 6.9 V cm^{-1} ns^{-1} the final ionisation profile was found to contain $N^+ = 2$, 4 and 6 rotational character. The change in rotational quantum number and therefore the adiabatic traversal of avoided crossings was dependent on the $\Delta N^+ = \pm$ 2 or 4 zero field core coupling. The strength of this coupling is

directly related to the size of the avoided crossing and therefore determines the probability of an adiabatic transition. Using the basic ideas obtained from this investigation, new experimental proposals are being developed where a greater state selectivity may be achieved. These proposals are described further below.

6.2 OUTLOOK

6.2.1 THEORETICAL ANALYSIS OF MOLECULAR SELECTIVE FIELD IONISATION

The main theoretical approach used to simulate the data obtained from selective field ionisation (SFI) investigations is the application of the Landau-Zener approximation.

$$P_{dia} = \exp\left[-\frac{2\pi|V_{12}|^2}{\hbar \cdot (dW_{12}/dt)}\right] \tag{6.1}$$

This equation calculates the probability of diabatically traversing an avoided crossing, where an avoided crossing is created between two Stark states as a result of a zero core field coupling. This theory of SFI was first established by Harmin *et al.* [11,12]. A modified version of this model, developed by Noordam *et al.* [13] was used to model the effects of several n Stark manifolds mixing to the point of ionisation in Li and Rb. They achieved this *via* repeated application of the Landau–Zener approximation. This is the basis of current activity in this group to develop a model which will give a more detailed account of what happens to a molecular Rydberg system as a rising electric field pulse is applied.

The literature regarding the simulation of the passage to ionisation upon applying a rising field pulse is limited to atomic systems. This is mainly due to the complicated nature of a molecular system in an electric field. The larger number of Rydberg series associated with the presence of a molecular core, results in a highly congested Stark map in the high n region when placed in an electric field. This in turn means that there are a larger number of avoided crossings between the Stark states resulting in a greater number of possible routes to ionisation. In order to simulate these different routes to ionisation, one would need to determine the outcome of every possible traversal of avoided crossings encountered in the region of interest. This is the basis of our theoretical calculations, combined with the matrix diagonalisation method. The positions of the avoided crossings will be determined using the matrix diagonalisation method and the traversal of them will be determined by applying the Landau-Zener approximation. This approach will give all possible routes to ionisation with the relative probability of it occurring.

6.2.2 CONTROLLING FIELD IONISATION USING SHAPED ELECTRIC FIELD PULSES

The technique of state selective field ionisation has been used in various investigations to manipulate the ionisation process using shaped electric field pulses in atomic systems [14,15]. As presented, the results in chapter 5 show that it is also possible to control the outcome of field ionisation in a molecule simply by varying the slew rate of the applied electric field pulse. The proposal of a new experiment extends this work further by introducing more selectivity using a shaped electric field pulse. Initial investigations will use two electric field pulses

to control the traversal of the first avoided crossing created by two states. The first pulse will be a slow rising pulse over the field region at which the avoided crossing is created. The slew rate of this field pulse will be varied such that the avoided crossing is traversed either adiabatically (slow slew rate) or diabatically (fast slew rate). The second electric field pulse will have a fast slew rate such that after the first avoided crossing the electron is ionised entirely diabatically. Varying the slew rate of the first electric field pulse will produce field ionisation traces that vary in time and field. This will be an indication of how the avoided crossing between the two states was traversed and therefore the extent to how much the final ionisation profile is due to each of these states. The idea behind this experiment is similar to the investigation by Tada *et al.* [16] where they control the first avoided crossing between the low l states and manifold states of high n (> 90) Rydberg states in Rb. They do this by applying an electric field pulse with a slow slew rate such that the first avoided crossing is traversed adiabatically. After this avoided crossing a field pulse with a fast slew rate is applied, resulting in ionisation of the atoms. Another example of an experiment which employs a shaped pulse was by Gutler *et al.* [14] who applied a shaped pulse to control the state selectivity of the Rydberg states of Rb. They applied a field pulse with fast step followed by a slow ramp and this allowed for better separation of the s, p and d states of Rb.

Further investigations, will require the use of a high voltage electric pulse shaper. This experiment will employ just one shaped electric field pulse to manipulate the route to ionisation and therefore force the electron onto various states otherwise not accessible.

6.3 REFERENCES

1. M. Dantus and V. V. Lozovoy, *Chemical Reviews* **104** (4), 1813 (2004).
2. J. R. R. Verlet, V. G. Stavros, R. S. Minns, and H. H. Fielding, *Physical Review Letters* **89** (26), 263004 (2002).
3. J. Ahn, D. N. Hutchinson, C. Rangan, and P. H. Bucksbaum, *Physical Review Letters* **86** (7), 1179 (2001).
4. J. Ahn, C. Rangan, D. N. Hutchinson, and P. H. Bucksbaum, *Physical Review A* **66** (2), 022312 (2002).
5. J. Ahn, T. C. Weinacht, and P. H. Bucksbaum, *Science* **287** (5452), 463 (2000).
6. C. Rangan, J. Ahn, D. N. Hutchinson, and P. H. Bucksbaum, *J. Mod. Opt.* **49** (14-15), 2339 (2002).
7. C. Rangan and P. H. Bucksbaum, *Physical Review A* **6403** (3), 033417 (2001).
8. R. E. Carley, E. D. Boleat, R. S. Minns, R. Patel, and H. H. Fielding, *Journal of Physics B-Atomic Molecular and Optical Physics* **38** (12), 1907 (2005).
9. T. Brixner and G. Gerber, *Chemphyschem* **4** (5), 418 (2003).
10. R. S. Minns, R. Patel, J. R. R. Verlet, and H. H. Fielding, *Physical Review Letters* **91** (24) (2003).
11. D. A. Harmin, *Physical Review A* **56** (1), 232 (1997).
12. D. A. Harmin and P. N. Price, *Physical Review A* **49** (3), 1933 (1994).
13. F. Robicheaux, C. Wesdorp, and L. D. Noordam, *Physical Review A* **62** (4), 043404 (2000).

16. Y. Kishimoto, M. Tada, K. Kominato, M. Shibata, S. Yan
Haseyama, I. Ogawa, H. Funahashi, K. Yamamoto, and S.
Physics Letters A **303** (4), 279 (2002).